Mechanics of functionnal thin films : instabilities and adhesion

Jean-Yvon Faou

To cite this version:

Jean-Yvon Faou. Mechanics of functionnal thin films : instabilities and adhesion. Mechanics of materials [physics.class-ph]. Université Pierre et Marie Curie - Paris VI, 2013. English. NNT : . tel-00868409

HAL Id: tel-00868409

https://theses.hal.science/tel-00868409

Submitted on 1 Oct 2013

HAL is a multi-disciplinary open access archive for the deposit and dissemination of scientific research documents, whether they are published or not. The documents may come from teaching and research institutions in France or abroad, or from public or private research centers.

L'archive ouverte pluridisciplinaire **HAL**, est destinée au dépôt et à la diffusion de documents scientifiques de niveau recherche, publiés ou non, émanant des établissements d'enseignement et de recherche français ou étrangers, des laboratoires publics ou privés.

THÈSE DE DOCTORAT DE
l'UNIVERSITÉ PIERRE ET MARIE CURIE

En Physique et Chimie des matériaux (Paris)

Présentée par

Jean-Yvon FAOU

Pour obtenir le grade de

DOCTEUR de l'UNIVERSITÉ PIERRE ET MARIE CURIE

Sujet de la thèse :

Mécanique des couches minces fonctionnelles : instabilité et adhésion

Soutenue le 20 septembre 2013

devant le jury composé de :

M. Christophe COUPEAU	Président
M. Christian GAUTHIER	Rapporteur
M. Loïc VANEL	Rapporteur
M. Basile AUDOLY	Examinateur
M. John HUTCHINSON	Examinateur
M. René GY	Invité
M. Guillaume PARRY	Invité
M. Étienne BARTHEL	Directeur de thèse

A ma femme,

Acknowledgments

Je remercie Loic Vanel et Christian Gauthier d'avoir accepté d'être rapporteurs de mon manuscrit et Christophe Coupeau de présider mon jury. Merci également à Basile Audoly et John Hutchinson pour votre participation au jury. Vos relectures attentives et votre jugement indépendant permettent de valider les modèles proposés dans ce manuscrit et les résultats qui en découlent.

Le cadre de travail et les moyens apportés sont les bases nécessaires à un travail de qualité. Je remercie pour cela Saint-Gobain Recherche ainsi que l'ANRT pour avoir financé ce sujet de recherche et avoir eu confiance dans le candidat que j'étais pour le mener à bien. Je remercie la directrice de laboratoire Surface du Verre et Interface d'alors Elin Sondergard et la directrice actuelle Emanuelle Gouillard de m'avoir accueilli.

Le travail de recherche que constitue une thèse est la continuation d'un long processus, pas nécessairement douloureux, commencé il y a bien longtemps au siècle dernier. J'aimerais remercier FR3 pour la diffusion des "‘Il était une fois"’, qui a su susciter en moi dès le plus jeune le goût de la découverte. Puis plus tard, lors de mon stage de master I entre le LPN et l'ENS C. Gosse, T. Barilero et T. Le Saux de m'avoir réellement fait découvrir le travail de recherche dans un environnement des plus stimulants. Je garde un excellent souvenir de mon passage à l'HKUST, merci au professeur H. S. Kwok m'avoir accueilli pour mon stage de master II. Merci à Jacob, Yuet Wing et He de m'avoir tant appris sur le sujet des OLED et mes neufs compères de bureau pour leur sympathie et au souvenir des dix mille dim sum que nous avons mangés ensemble, *yat man do dze*.

La thèse est loin d'être un parcours initiatique où l'élève est jeté au désert et doit survivre pour rejoindre l'oasis muni d'une gourde, *le sujet*, et pour seules indications de vieilles inscriptions, *la bibliographie*. Quoique... Non une thèse est avant tout un travail d'équipe, car sans échanges point d'avancement. Je dois bien dire qu'au cours de ces trois ans, jamais je n'ai senti la soif, les discussions furent nombreuses et riches. Aux maîtres de toutes sources d'inspiration je remercie sincèrement Etienne Barthel mon directeur de thèse, voir Fig. 1 et mes encadrants, Guillaume Parry et Sergey Grachev pour avoir toujours été présents, près à m'écouter et à me supporter. A Saint-Gobain Recherche je remercie particulièrement Alessandro Benedetto et Xavier Caillet pour leur suivi et leurs éclairages particuliers. Au SiMAP, je remercie chaleureusement Muriel Braccini et Raphael Estevez pour leur accueil à un thésard lointain et peu présent. Ces rares moments auront été mis efficacement à contribution.

J'en arrive à SVI ou plutôt au labo mixte, abréviation locale d'une association loin d'être unique. Pour un breton, monter à la capitale n'est pas toujours chose aisée. Il faut apprendre la langue (on n'envoie plus personne, on ne va plus au centre ville ni à la perception) et s'adapter au climat sec et froid, décidément il ne pleut plus et les températures négatives ne sont pas un conte pour enfant. Tout cela requiert une bonne préparation du terrain. Alors merci à François pour avoir été un pionnier au sein du laboratoire. C'est à SVI que j'ai passé le plus de temps et où, par voie de conséquence, mes remerciements seront les plus nombreux. Merci à Pierre, pour être toujours présent au café (quand il en reste) et pour avoir accepté d'être mon tuteur, j'en profite au passage pour remercier Milita, qui fait qu'un paquet de filtre se fini toujours moins vite qu'un paquet de café. Le café c'est autant la boisson qui réveille les esprits que le moment qui permet de les aiguiser. Merci Davy pour ton esprit critique, merci Jérémie pour tes nombreux conseils toujours à propos sur des sujets variés et des idées de manip farfelues, nous avons voyagé dans le futur avec ces nombreuses manip du siècle, vive la surfusion. Merci à l'équipe MISSTIC. Par chronologie, Anne tout d'abord, pour ta bonne humeur autant que pour ton bon sens et tes conseils, ainsi que pour l'installation de ce merveilleux AFM. Ensuite Raphael, pour venir du bon côté de l'Odet, avoir toujours été disponible pour réaliser de magnifiques images MEB qui illustrent ce manuscrit et enfin pour ces réparations héroïques de notre vaisseau spatial. Merci aux compagnons du bureau 536 pour l'ambiance à l'intérieur comme à l'extérieur, aux anciens, Lina pour m'avoir appris l'espagnol, gracias, Charles qui m'a légué bien plus que des cales, Arthur avec qui on peut rire de tout et aux survivants, Barbara et William. Merci aux doctorantes, Helena, Ning, Marine et surtout Corinne, pour cette organisation impeccable et ta bonne humeur permanente. Ces messieurs, Joël, Yann à la pédagogie exagérative et pantomimique souvent juste et Gauthier sans qui mes années de latin et de grec seraient restées endormies et qui a su stimuler à maintes reprises ma rhétorique. A vous tous je vous dis un grand merci. Je ne saurai oublier les anciens, Dawn, Rémy toujours prêts a transmettre leur expérience. Enfin Isabelle, qui à ce niveau fait partie de la famille, tu m'as vendu du poisson comme personne et il était toujours délicieux, merci. Ces nombreuses soirées passées ensembles ont formé un groupe qui reste soudé et contribue fortement à la bonne entente qui règne au laboratoire.

Un labo ne serait pas ce qu'il est sans ses petites mains oeuvrant dans l'ombre, je tiens à particulièrement remercier Ekaterina pour ta rigueur à toujours contraindre de couches sans en ressortir stressée et Théo, gars de l'ouest au grand coeur et aux expériences impeccables et sachant oscillé aussi bien dans un canal qu'à l'Auberzinc.

Enfin, merci aux amis, Jérémy, Tommy, loin des yeux mais toujours proches du coeur. Merci à tout le clan, pour ces longues soirées pleines de rigolade. Merci à mes parents et à mes soeurs pour tout et cela va bien au-delà de ces trois ans de thèse. Mon plus grand merci va à celle qui a le plus grand mérite et qui paradoxalement est en bien des points la plus éloignée du sujet. Elle tient la plus grande place dans mon coeur depuis des années, Si Nga, ma femme, sans qui je n'aurai sans doute pas démarré ni fini une thèse, cette thèse, *m goy sai ngo lo po, ngo ngoi lei.*

Man soi, man soi, man man soi...

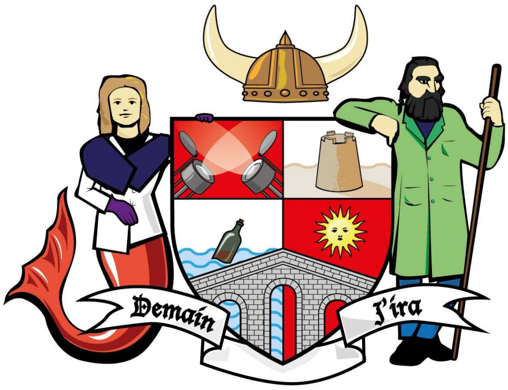

Figure 1: Armoiries du laboratoire Surface du Verre et Interfaces.

Contents

Introduction **1**

1 Mechanical instabilities of multilayer stacks **5**
- 1.1 Low-emissivity multilayer . . . 5
  - 1.1.1 Low-emissivity glazing . . . 5
  - 1.1.2 Multilayer structure . . . 6
- 1.2 Mechanics of rupture . . . 7
  - 1.2.1 Cracks in bulk . . . 7
  - 1.2.2 Interface crack . . . 10
  - 1.2.3 Thin film delamination . . . 10
- 1.3 Adhesion . . . 13
  - 1.3.1 True work of adhesion . . . 13
  - 1.3.2 Adhesion in fracture mechanics . . . 14
  - 1.3.3 Measurement of K_c and G_c . . . 15
- 1.4 Strategy to study adhesion through buckling driven delamination . . . 19
- Bibliography . . . 20

2 Residual stresses in molybdenum thin films **23**
- 2.1 Thin films deposited by magnetron sputtering . . . 23
  - 2.1.1 Process . . . 23
  - 2.1.2 Growth of a thin film . . . 25
  - 2.1.3 Mechanics of thin film . . . 26
- 2.2 Measurement of stress . . . 30
  - 2.2.1 Curvature and stress measurement . . . 30
  - 2.2.2 Strategy adopted for stress measurement . . . 31
- 2.3 Highly compressively stressed molybdenum layer . . . 33
  - 2.3.1 Influence of the partial pressure of Ar . . . 34
  - 2.3.2 Film relaxation . . . 36
  - 2.3.3 Influence of a bias potential at the substrate . . . 38
  - 2.3.4 Influence of oxygen . . . 39
  - 2.3.5 Discussion . . . 43

2.4 Conclusion 45
Bibliography 45

3 Cohesive zone model for buckling driven delamination 47
3.1 Buckling driven delamination of thin films 47
3.1.1 The straight sided blister : a post-buckling solution 48
3.1.2 Equilibrium of the crack front 49
3.1.3 Mode mixity dependence of the interfacial toughness 52
3.1.4 Limitations and strategy adopted to study buckling driven delamination 54
3.2 Analytical resolution for a straight sided blister 56
3.2.1 Free-buckled area 56
3.2.2 Dugdale distribution for mode I and mode II 57
3.3 Numerical resolution 59
3.3.1 Non-linear plate implementation 59
3.3.2 Cohesive zone implementation 60
3.3.3 Unilateral contact 62
3.3.4 Resolution method 62
3.4 Numerical results for a straight sided blister 63
3.4.1 Geometry 64
3.4.2 Effect of the loading 64
3.4.3 Effect of process zone 68
3.5 Conclusion 71
Bibliography 71

4 Buckles morphology: experiments meet simulations 75
4.1 Experiments and propagation mechanism 75
4.1.1 Design of the experimental system 76
4.1.2 Experimental investigation of the morphology of the blister . . 77
4.1.3 Comparison with simulations 78
4.1.4 Branching blisters 80
4.1.5 Pinning of the crack front : sagging and mode mixity 81
4.2 Simulations: Phase diagram of buckling driven delamination patterns 82
4.2.1 Phase diagram 82
4.2.2 Condition for propagation of the buckling driven delamination. 84
4.2.3 Range of stability of the TC morphology 86
4.2.4 Stress released in the blister during buckling 87
4.3 Large cohesive zone sizes: The role of Ag 88
4.3.1 Periodic branching: evidence for hexagonal pattern 89
4.3.2 Telephone cords : large aspect ratio 90
4.3.3 Role of the process zone size in the delamination morphology . 92

4.3.4 Material origin of a large process zone at the interface SiO_x/Ag 93
4.3.5 Discussion 95
4.4 Conclusion 96
Bibliography 96

Conclusion 99

A List of samples 101

B Effect of mode mixity definition 103

C Stress tuning in in sputter-deposited MoO_x films 107

D How Does Adhesion Induce the Formation of Telephone Cord Buckles? 113

Introduction

Glass is a very specific technological material. Dating back to Antiquity it is still nowadays subject to a lot of research. Its broad use as flat glass in construction and automotive applications has required constant innovation from engineers and researchers. In particular, the development of thin film deposition on large surfaces has provided a cheap way to add new properties (optical, electrical, wetting) to flat glass. Anti-reflective coatings, double glazing windows or self-cleaning glass are now widely available on the market.

New properties are achieved by depositing films few nanometers thick. At the nanometer scale for example, it is possible to deposit a transparent material even though its bulk is opaque in the visible spectrum. A good example is the use of a thin silver layer to create a functionnalized glass reflecting the infra-red. Such a glass will possess insulating properties. By depositing several layers, properties can be combined and industrial stacks often possess tens of layers.

Glass products having a lifetime of several decades, use of thin films has brought new challenges to bring the mechanical stability of the stacks to the same level as glass. One major mechanical instability known is delamination of the stack from its substrate. One source of delamination resides in residual stresses present in the stack coming from the deposition process or by external stresses due to the post-treatment of glass (annealing, forming). Another source for delamination is the weak adhesion of the film to the substrate. Combination of weak adhesion and compressive stresses results in buckling driven delamination of the film, leaving blisters on the glass surface (Fig. 2). Such defects are highly undesirable.

As residual stresses coming from the process itself are often unavoidable, a lot of efforts have been dedicated to improving adhesion of thin films. However this effort is limited as few quantitative tests, especially tests representative of real fracture conditions, are available for adhesion measurements of thin films. This is partly due to the nanometric scale of the layers but also to the sensitivity of the interfacial toughness to the mode mixity.

Due to the non-linearity of buckling, blisters possess a width of about thirty times the film thickness and are thus easy to measure. It was shown on simple cases, such as a straight sided blister, that width of the buckles is limited by adhesion. There is therefore interest in using blisters to measure interfacial toughness in thin film systems.

The simple straight sided pattern is not however often encountered when large in-plane compression is present in the film and the common morphology is the telephone cord like blister 2. Unlike the straight sided blister, the relation between the size of the telephone cord like blister and interfacial toughness is unknown. Previous academic work have proposed to use models based on the straight sided delamination to characterize more complex patterns, but this practice has limited theoretical ground. Experimental studies of the relation between buckle size and interfacial toughness has however been limited by control of adhesion of the system.

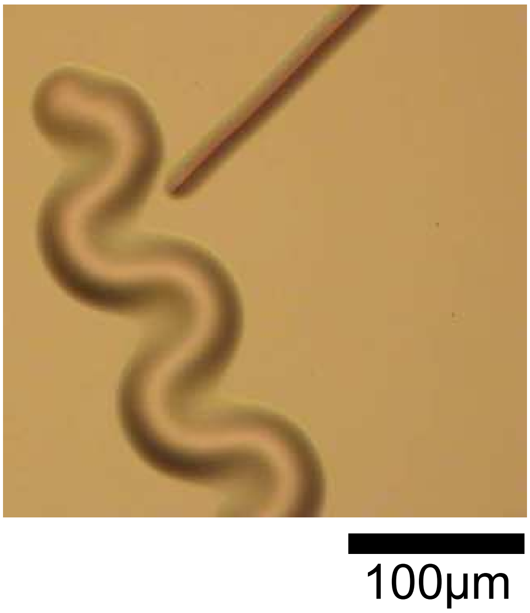

Figure 2: Optical micrograph : delamination of a molybdenum thin film on silicon. Broken straight sided blister and telephone cord like blister are visible.

The purpose of this thesis is : 1) to generate well controlled buckles and study their morphology ; 2) to develop a model for buckling driven delamination of thin films deposited on rigid substrate under equi-biaxial loading, in order to identify the relation between interfacial toughness and the morphology of delamination.

This research project has required expertise in the experimental field as well as in the numerical field and is reflected by the implication of the following research units:

- the group "‘Couches Minces et Nanostructures"’ of the laboratory *Surface du Verre et Interfaces* of the joint unit CNRS/Saint-Gobain in Aubervilliers
- the group "‘Physique du Métal"’ of the laboratory *Science et Ingénierie des Matériaux et Procédés* in Grenoble

The first chapter presents the context of the work. Starting from the example of low emissive stacks and their industrial application, the adhesion problem in silver based multilayers is introduced. We then introduce basic ideas of fracture mechanics behind delamination as well as interfacial toughness and present available measurement techniques. Understanding of technological limits of such measurements leads us to propose a way to study delamination of thin films through buckles.

In the chapter 2, we present an experimental study of residual stresses in molybdenum thin films. This study is driven towards understanding how stress develop in molybdenum and how compressive residual stress can be increased for delamination of thin films.

In chapter 3, we present an analytical model of the straight sided delamination problem as a reference. We then present our simulation of the buckling driven delamination in the general case. Our model couples thin plate buckling and cohesive zone at the interface. It is first applied to the straight blister case and solved numerically using finite elements method. Results of the analytical resolution and our model are compared and discussed.

In chapter 4 we present an experimental study of buckling driven delamination. Results obtained on propagation of the delamination crack front are discussed with the help of the simulation. From the numerical resolution of the problem, I propose a phase diagram of the delamination morphology. Experimental cases not falling within the phase diagram are discussed and reveal an interesting behavior of silver at the interface.

In the conclusion of this thesis we present some of the perspectives of this work in order to further improve the buckling driven delamination model and control the delamination of thin films by introduction of low yield stress layer at the interface.

Chapter 1

Mechanical instabilities of multilayer stacks

The art of rupture dates back to the stone age, when humans started knapping flint stones to produce tools, such as knife and arrow heads [1, 2]. Even though fracture of brittle materials could be mastered in an empirical way, systematic study of crack formation and propagation only came much later [3, 4, 5]. Understanding propagation of cracks is still nowadays of great concern, in particular to improve mechanical stability and durability of heterogeneous materials, such as multilayer stacks.

1.1 Low-emissivity multilayer

In Saint-Gobain, float glass is functionnalized by means of low emissivity layers. These layers are deposited on the inner side of windows in order to enhance thermal insulation of buildings. Such windows play an important role in the effort to reduce energy consumption for buildings heating.

1.1.1 Low-emissivity glazing

Insulating two environments, say indoor and outdoor, consists in limiting heat transfers between them. In order to do so, several heat mechanisms need to be dealt with and we will take the example of a double glazing window, see Fig 1.1. They are all due to the difference of temperature between the two environments. The first transfer is the conductive heat transfer. It is expressed locally by the differential form of the Fourier law of thermal conduction :

$$\vec{q} = -\lambda \vec{\bigtriangledown} (T) \tag{1.1}$$

where $\vec{q}$ is the heat flux density between indoor and outdoor, $\vec{\bigtriangledown} (T)$ is the gradient of temperature between indoor and outdoor and λ the thermal conductivity at the interface. As there is little control over the temperature gradient, limiting the heat flux means reducing λ. This can be achieved by introducing some distance between the two glass sheets of a double glazing. The spacing is then filled by a gas having a lower thermal conductivity than air, such as argon.

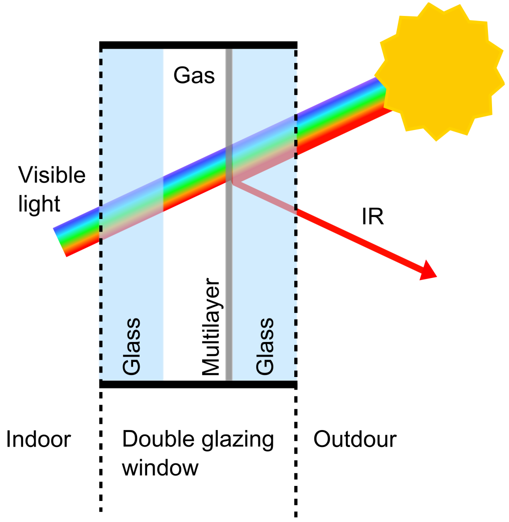

Figure 1.1: Schematic of a double glazing window with a low emissive multilayer.

The second heat transfer is the convective heat transfer and corresponds to the heat flux transfered through movement of a fluid. In a double glazing the fluid is simply the gas filling the spacing between the two glasses.

The third heat transfer is the radiative heat transfer. It corresponds to heat flux by means of electromagnetic field in the infrareds (wavelength above 5 μm). Glass almost completely absorbs those wavelengths and can reemit the incident flux by radiation. More quantitavely, a black body will absorb 100% of the incident flux and reemit it entirely. Under a given flux (at a given wavelength), the emissivity, ϵ of a material is defined as the energy radiated by the material, E_R, and normalized by the energy a black body would radiate, E_{RBB}.

$$\epsilon = \frac{E_R}{E_{RBB}} \tag{1.2}$$

In order to prevent glass to reemit the incident flux and thus decrease its emissivity, a high reflection in the infrared needs to be achieve at the first glass/air interface. At the same time, keeping high transmission within the visible spectrum (wavelength between 390 nm to 700 nm) is essential.

1.1.2 Multilayer structure

We present on Fig. 1.2 a schematic cross-section of a low emissivity stack. The key

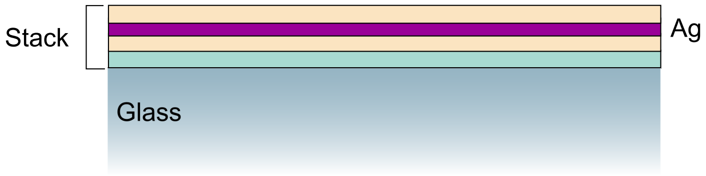

Figure 1.2: Schematic of a low emissivity stack. The silver layer is encapsulated within dielectric layers.

material to achieve both reflectivity in infrared and high transmission in the visible spectrum is silver. Silver is deposited by magnetron sputtering as a thin layer of 10 to 20 nm. It is encapsulated within several dielectric layers. The dielectric layers beneath and above silver serve both optical and mechanical properties. The main effect is the influence on growth of the silver layer and grain size. The dielectric materials used by Saint-Gobain are generally oxides such as ZnO, SnO_2 and nitrides such as Si_3N_4.

There are two main mechanical limits to such multilayers. The first is the poor adhesion of silver to oxides and nitrides [6]. The second is the residual stresses that arise either from the deposition process or annealing of such layers. Both mechanical limits are sources for interface cracks. In the next section we introduce the mechanics of rupture and how adhesion and residual stresses influence the delamination of a film.

1.2 Mechanics of rupture

By mechanics of rupture we consider the study of the propagation of a crack in a medium resulting in separation of two interfaces. In this section we recall the main ideas governing the study of cracks and especially interface cracks. These ideas will support the development of a model to study the delamination process of thin films in chapter 3.

1.2.1 Cracks in bulk

Empirically the fracture of most of a test piece occurs when the stress exceeds some critical level. For brittle materials, it was early observed that this level of external load fluctuated significantly. The reason for fluctuation lies in the initial defect. Cracks will in general nucleate at defects in the materials, that by geometrical consideration are stress concentrator. Therefore locally, the stress can exceed the external load by several orders of magnitude. Even though this cohesive stress exists for the material at a microscopic or nanoscopic scale, observation at this scale is very limited by present technical standards.

Energy criterion for crack propagation A more practical approach was proposed by A.A. Griffith in 1920 [3]. The model considers the energy balance of a system with a crack of initial surface S lying within an elastic body. The loading applied to the elastic body results in an elastic energy U_E. We also note W_L the work done by the external load and U_S the energy needed to create new crack surface during propagation. At equilibrium, and when the work done by the external load is zero, the energy balance of the system is :

$$U = U_E + U_S \tag{1.3}$$

We assume that the crack length increases by an amount δ_c. It is obvious that while the crack extends the mechanical energy of the system will decrease, $dU_E/dc < 0$. At the same time the free surface energy increases as molecular bonds needs to be broken over the length δ_c to create new crack surface, $dU_S/dc > 0$. Balance of those two terms of mechanical and surface energy provide the concept of equilibrium of a crack which is defined by :

$$\frac{dU}{dc} = 0 \tag{1.4}$$

In this case formation of crack is neither favored by the strain energy of the system nor limited by surface energy.

In a more complex system, the variation of elastic energy spent during the formation of a crack of surface A is called the energy release rate[1] and is noted $G = dU_E/dA$. Using Eq. 1.4 we therefore have at equilibrium :

$$G = \Gamma_c \tag{1.5}$$

with Γ_c the toughness of the material considered. We have here a criterion for crack propagation. If the energy release rate is larger than the material toughness, the crack will propagate and if the energy release rate at the crack tip is smaller than the material toughness, the crack will stop.

Crack propagation: rupture modes In order to proceed to a stress analysis of the plane-crack problem, it is useful to define the three *modes* of crack opening. In our case only the first two will be necessary. Mode I, or opening mode, corresponds to the normal separation of crack walls under tensile stress. Mode II, sliding or shear mode, corresponds to mutual shearing of the crack walls along a direction normal to the crack front. There is also a third mode, mode III, or tearing mode, that corresponds to mutual shearing of the crack walls but along a direction parallel to the crack front. All three modes are presented in Fig 1.3.

---

[1] Note that the energy release rate may exceed locally the elastic energy per unit area available in the system due to the particular geometry of a crack.

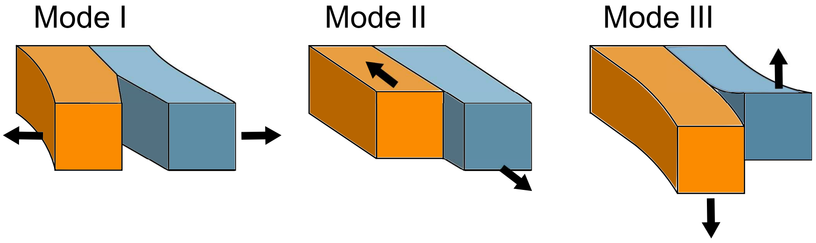

Figure 1.3: Schematic of the three modes of rupture. Mode I : opening mode ; Mode II : shear mode ; Mode III transverse mode.

There are many experimental evidences that the direction of propagation of a crack is highly related to crack-tip field. In particular it has been observed in [7] that the crack propagates so that the plane of rupture undergoes maximum tensile component at the crack tip. Therefore cracks in bulk brittle materials are often considered pure mode I cracks. Other modes can however be present when the initial geometry forces the crack to deviate from mode I, for example when there is an interface.

Crack propagation: non-linear crack-tip field The work balance principle explained above was applied to the case of metals by Orowan and Irwin in the early 1950s. Due to ductile behavior of metals, such as silver, the high level of local stress around the crack tip was enough to cause plastic deformation around the crack tip. This plastic zone around the crack tip may dissipate large amount of mechanical energy and therefore needs to be taken into account in the energy balance.

Irwin and Orowan, working independently, proposed to include a zone around the crack tip in which the material stress-strain relation possess a nonlinear behavior. Outside, the stress-strain relation remains linear, see Fig 1.4. In this fashion, the ductile behavior of the material may be taken into account. Several models for the

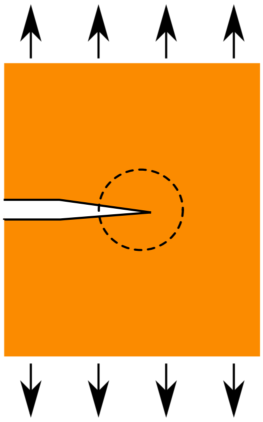

Figure 1.4: Schematic of a crack in a bulk. The loading is applied far from the crack tip. The domain influenced by non-linear effects is presented in dashed lines.

crack tip have been proposed to match experimental observations. Cohesive zone models are often used, such as Dugdale [8] for plastic materials. These cohesive zone models also apply to brittle materials, see Barenblatt [9] for perfectly brittle materials. Choice of the existence and extension of the process zone around the crack tip and choice of the shape of the non-linear stress-strain relation will be discussed in detail in chapter 3 for the delamination of a thin film on a rigid substrate.

1.2.2 Interface crack

Rupture of heterogeneous materials has been studied for a long time. Propagation of cracks in these systems differs from the bulk case in several aspects, in particular because of the presence of interfaces. We consider the simple case of a heterogeneous system made of two isotropic elastic solids A and B both of infinite thickness and sticked together, see Fig 1.5.

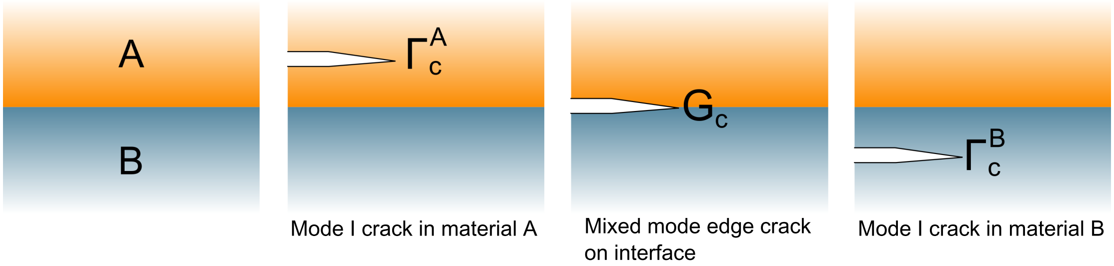
A
B
Γ_c^A
Mode I crack in material A
G_c
Mixed mode edge crack on interface
Γ_c^B
Mode I crack in material B

Figure 1.5: Schematic of a crack propagating at an interface.

Starting from the edge of the sample, the crack can either propagate in material A, B or at the interface between material A and B. We note Γ_c^A and Γ_c^B the toughness of material A and B respectively, as already defined above. Similarly for an interface, the energy per unit area needed to separate material A from material B is called the interfacial toughness and noted G_c.

While in a bulk propagation the crack path maximizes tensile stresses, in the case of interfacial rupture the crack path is pre-defined by junction of material A and B. It is therefore possible to keep the crack tip under a mixed mode, i.e having non-zero component for the mode II (and mode III). This possibility of mixed mode is a key point to understand crack propagation in many interfacial crack problems discussed in chapter 3.

1.2.3 Thin film delamination

Thin films are typically systems in which an interfacial rupture is likely to occur. This phenomenon is known as *delamination*. In this case, the interface crack problem consists of an elastic film, or stack, of thickness h lying on an elastic substrate which can be considered semi-infinite as its thickness is large compared to h.

Residual stress as driving force. Thin films of metals, ceramics and polymers can be subject to residual stresses, sometimes up to several GPa. The various origins of residual stresses will be discussed in the next chapter. Let us here assume the simplest mechanism : a thermal mismatch origin. The film and the substrate are two isotropic linear elastic solids with elastic moduli, Poisson ratios and thermal expansion coefficients (E_f, ν_f, α_f) and $(E_f s, \nu_s, \alpha_s)$ respectively. At high temperature T_0 the film and substrate are stress-free. Upon cooling to room temperature T_t, a biaxial misfit stress, σ, between the film and the substrate develops.

$$\sigma = \frac{E_f}{1-\nu_f} \left(\alpha_f - \alpha_s\right) \left(T_0 - T_t\right) \tag{1.6}$$

Crack morphologies that develop after cooling depend on the sign of σ.

Film delamination under tension. The value of the residual stress σ is positive when $\alpha_f > \alpha_s$. At room temperature the film is therefore under a tensile stress. The residual tensile stress provides a driving force for cracking of the film, see Fig. 1.6. A surface crack can nucleate from a flaw in the thin film. The crack will grow in mode I with $G = \Gamma_c^A$ until it reaches the interface. At this point it can either stop if the toughness of substrate and interface are large enough. The crack can also kink and go on as an interface crack. Interface cracks will be favored in a edge crack problem due to stress concentration or if the toughness of the substrate is large compared with G_c.

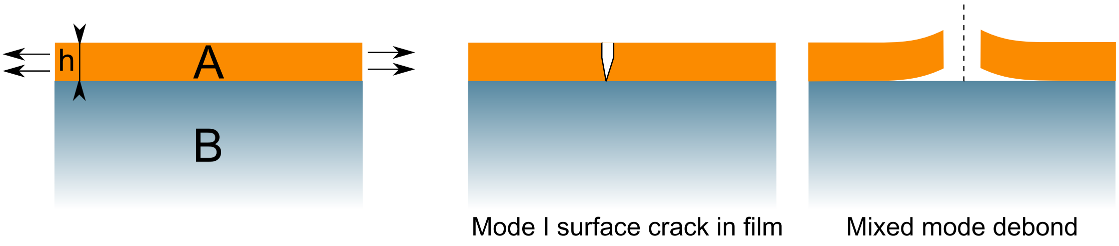

Figure 1.6: Possible crack paths under tension.

Film cracks and interface cracks have been and are still intensively studied. Many examples of such film delaminations can be found in the literature. A good example is the work of Zhuk *et al.* [10] for delamination of a stack of tensile stressed Ni films and epoxy on a silicon wafer, see illustration in Fig. 1.7. The combination of film cracking and film delamination under in-plane biaxial loading often leads to complex but interesting patterns [11], see also Fig. 1.7 and study of those morphologies are themselves a complex topic.

Film delamination under compression The opposite case corresponds to a com-

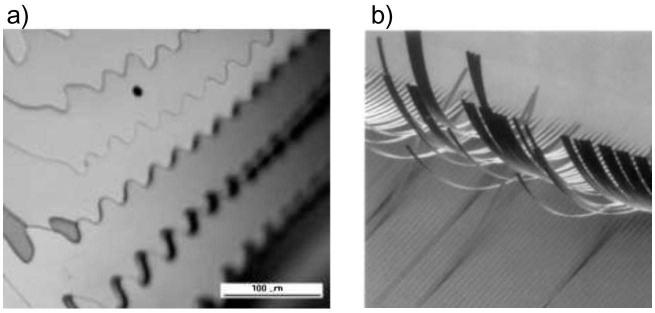

Figure 1.7: a) Delamination of tensile stressed Ni films on epoxy from Zhuk *et al.* [10]. b) Delamination and crack pattern of tensile stressed Mo films on Si substrate.

pressive residual stress in the film after cooling, i.e. $\sigma < 0$. In this configuration, once the crack has nucleated from an initial defect, its growth will be driven by buckling of the film. Buckling is essentially a mechanical instability which causes the film to develop large out-of-plane displacement above a critical load, see Fig. 1.8. The morphology adopted by the film after buckling is called a *buckle* or *blister*. The crack driving force is the residual stress stored in the film. The extent of the decohesion is limited by the rupture of the in-plane interface, and thus called *buckling driven delamination*. Buckling driven delamination of thin films can result in very simple shapes, such as the straight and circular blisters [12]. Under larger in-plane equi-biaxial loading, the buckled films often display a tendency to form periodic patterns such as the telephone cord (TC) like blister, see Fig. 1.9. Though the TC blister has been widely observed in various systems at the nanoscale [13] or meter scale (see Fig. 1.9), other morphologies exist and differ from the TC. Among them, herringbone blisters and branching blisters are the most remarkable [14]. Even though it is possible to model properly the behavior of a straight blister and couple the non-linear response of a plate with the interface rupture, a general approach is still lacking for understanding the more complex shapes of buckles. Chapter 3 is dedicated to the study of a model coupling the non-linear response of the film and interfacial toughness.

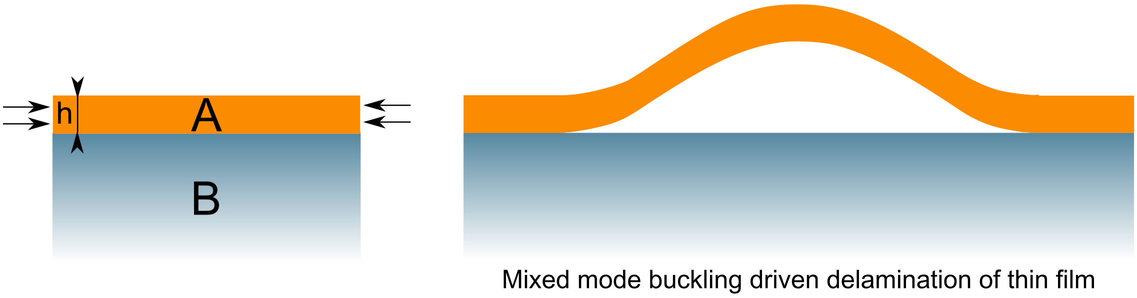

Figure 1.8: Schematic of buckling driven delamination of a thin film under a compressive residual stress.

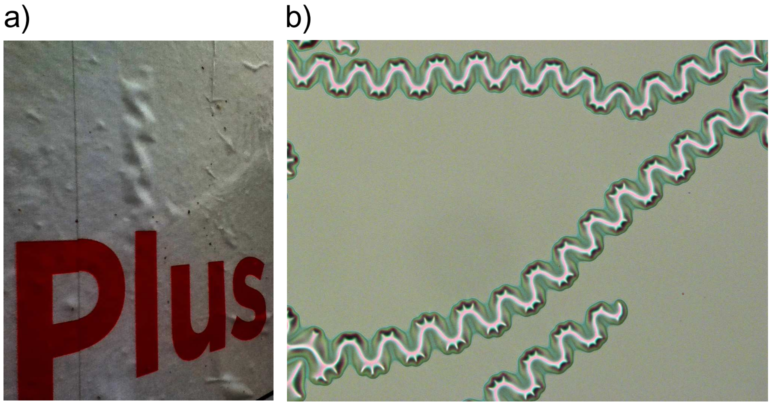

Figure 1.9: a) 5 cm large TC blister on an advertisement in Aubervilliers. b) 50 μm large TC blisters of Mo thin film on silicon.

1.3 Adhesion

1.3.1 True work of adhesion

From a thermodynamic point of view, the *true work of adhesion*, W_A, of a given interface is the amount of energy required to create free surfaces from the bonded elastic solids, say a film and a substrate. The Young-Dupre equation gives :

$$W_A = \gamma_f + \gamma_s - \gamma_{fs} \tag{1.7}$$

where γ_f and γ_s are the specific surface energies of the film and the substrate respectively and γ_{fs} is the energy of the interface. The true work of adhesion is an intrinsic property of the couple formed by the film and the substrate. It depends on the physical and chemical interactions between them.

The true work of adhesion can be measured by contact angle measurement [15, 16]. In practice a droplet of the film material is deposited on the substrate, often at elevated temperature for metals. At thermodynamic equilibrium the Young equation gives :

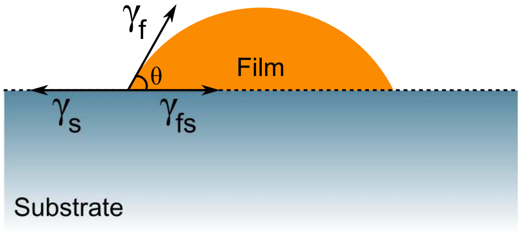

Figure 1.10: Partial wetting of a film material onto a substrate.

$$\gamma_{fs} = \gamma_s - \gamma_f \cos\theta \tag{1.8}$$

Substrate	Temperature	Contact Angle	Work of adhesion
Al_2O_3 [17]	300 K	130°	0.35 $J.m^{-2}$
SiO_2 [18]	300 K	123.8°	0.43 $J.m^{-2}$
Ti [6]	300 K	110°	0.64 $J.m^{-2}$
Mo [19]	1273 K	107°	0.69 $J.m^{-2}$
Mo [20]	1273 K	35°	1.76 $J.m^{-2}$

Table 1.1: Contact angle and true work of adhesion of silver with different substrates from the literature. Temperature measurement is indicated.

where θ is the contact angle between the droplet and the substrate, see Fig. 1.10. The true work of adhesion can therefore be re-expressed to obtain the Young Dupre equation

$$W_A = \gamma_f \left(1 + \cos\theta\right) \tag{1.9}$$

For metals on ceramics, the literature reports values of W_A in the range of 0.5 to 2 $J.m^{-2}$. For instance, the thermodynamic work of adhesion of gold on sapphire is around 0.5 to 0.9 $J.m^{-2}$ [15]. As silver is the critical layer in low emissivity multilayers, we report values of contact angles and W_A for Ag films from the literature in Tab. 1.1. From this list we can observe a wide range of values for adhesion of silver with oxides and metals.

1.3.2 Adhesion in fracture mechanics

In a mechanical test, it is impossible to measure W_A as other sources of dissipation such as plasticity around the crack tip and friction are involved. The value of adhesion obtained in a mechanical test is the interfacial toughness G_c, always larger than W_A. Only within reasonable limits, G_c can approach W_A. Two main definitions are commonly used to provide an adhesion value from fracture mechanics.

The first approach focuses on the stress field around the crack tip. Consider the simple cases of a crack in an isotropic elastic solid, see Fig 1.4. A general solution shows that the local stress around the crack tip at coordinates (r, θ) for each of the three modes can be expressed as :

$$\sigma_{ij} = \frac{K_n}{\sqrt{2\pi r}} f_{if,n}\left(\theta\right) \tag{1.10}$$

with $i = r, \theta$, $j = r, \theta$ and $n = I, II, III$. The K terms are the stress intensity factors. The stress intensity factors depend only on the applied loading and crack geometry and therefore determine the *intensity* of the local field. The other terms depend only on the spacial coordinates around the tip and correspond to the field *distribution*, subdivided in a *radial* component r and *angular* component θ. K needs to be linked to the energy release rate so that it can serve as a criterion for crack extension.

Under plane strain conditions, it can be shown that the energy release rate G reduces to :

$$G = K_I^2/\bar{E} + K_{II}^2/\bar{E} \tag{1.11}$$

where $\bar{E} = E/\left(1-\nu^2\right)$ [21].

The contribution of each mode is additive and enhances crack propagation. The relative proportion of mode II with respect to mode I is characterized by an angle of mode mixity ψ defined as :

$$\tan\psi = \frac{K_{II}}{K_I} \tag{1.12}$$

ψ varies from $-\pi/2$ to $\pi/2$, both pure shear loading with opposite signs, and $\psi = 0$ for pure mode I loading.

The second approach corresponds simply to the energy balance of the system by writing that under equilibrium we have equivalence in a crack interface problem between the strain energy release rate and the interfacial toughness G_c which is an intrinsic material component.

$$G = G_c \tag{1.13}$$

The parameters K_c and G_c are therefore equivalent to predict the resistance of a material or interface to crack propagation. They are both intrinsic material data. Equivalence is obtained through the energy release rate and will therefore depend on specific crack problem. Existence of crack propagation under mixed mode and thus non-zero contribution for mode II or mode III implies that the value of G_c might not be unique. In the literature a single value for K_c or G_c is however often provided and correspond in general to the mode I contribution. In this case $K_c = K_Ic$ and $G_c = G_{Ic}$. Both values are assumed to correspond to the true work of adhesion. The possibility of non-unique value for K_c and G_c and their dependences with ψ will be discussed in chapter 3.

1.3.3 Measurement of K_c and G_c

A proper determination of K_c or G_c in many crack configurations should reduce to determination of the energy release rate G for the crack equilibrium condition. It is only at equilibrium that G can be used to determine the intrinsic critical energy release rate. In many empirical tests, this is not the case : some tests infer an adhesive strength by subjecting the specimen to some external load and measuring the critical value at which it fails. Such tests are still useful for routine quality control, as they are fast and easy to implement. However they do not measure the interfacial toughness, since the strain energy release rate usually cannot be calculated.

Many efforts have been devoted to developing quantitative tests for interfacial toughness in thin films, and a universal test is not yet available. This is due to the variety of thin film systems. The film thickness can vary from few nanometers to the millimeter range and the plane strain assumption is only limited by the in-plane dimension of the film. The other limitation is the wide range of interfacial toughness a test would have to deal with, from $G_c \approx 0.1\,\mathrm{J.m^{-2}}$ to $G_c \approx 100\,\mathrm{J.m^{-2}}$ [22, 7], partly due to the mode mixity dependence of the interfacial toughness.

Interfacial toughness tests are based on the same general scheme. A specimen will be initially loaded until a crack propagates dynamically. A first challenge is therefore to have sufficient energy to cause propagation of a crack at the interface. Note that if the system possesses several interfaces, it will only be possible to probe the weakest interface. Equilibrium will be attained when the crack halts. One of the challenges is to find a configuration leading to crack arrest. Small values of interfacial toughness require a good command of loading. Finally, the strain energy release rate is evaluated and G_c can be estimated.

An overview of adhesion measurements techniques has been provided by Volinsky et al. in [23]. We will comment several tests commonly used which will serve for comparison.

Cleavage test The cleavage test uses the early work of Kanninen [24] that proposed an analytical solution for crack propagation in an *augmented* double cantilever beam (DCB) configuration. This configuration differs from the classical DCB by the existence of an elastic foundation. In case where the crack length is large in comparison with the thickness of the specimen it is not necessary to take into account this elastic foundation and simple beam theory can be used [4].

In both configurations it is possible to calculate the stress intensity factor from the thickness h of the cantilever, the opening at the edge of the specimen δ and the crack length L once the crack is stable. The energy release rate, at fixed opening, for the augmented DCB system is equal to :

$$G = \frac{3Eh^3\delta^2}{16\left(L + 0.64h\right)^4} \tag{1.14}$$

From Eq. 1.14, we see that when the crack length increases, the energy release rate decreases. As a result the cleavage test is mechanically stable. As this test is almost a pure mode I crack growth, the value of the stress intensity factor calculated is K_I. The test was adapted, see Fig 1.11, by Barthel and co-author [22] to study interfacial toughness in multilayer stacks deposited by magnetron sputtering. Thin films were deposited on glass. A counter glass plate was then glued with an epoxy on the stack. The glue is polymerized at 80°. A blade is then carefully inserted between the two glass plates at the multilayer location and imposes a given opening, δ. The crack propagates at the weakest interface of the stack and using Eq. 1.10 it is possible to estimate G_{Ic} of the weakest interface.

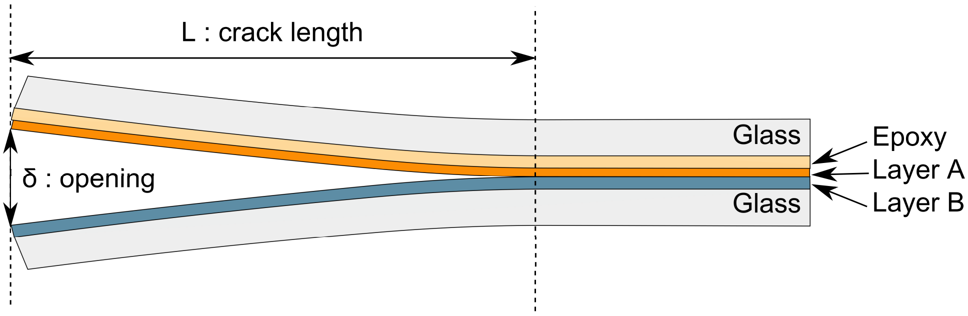

Figure 1.11: Cleavage test.

The range of interfacial toughness the cleavage test using glass as cantilevers can measure is limited by the toughness of glass which is close to $G_c \approx 5\text{J.m}^{-2}$, it is thus difficult to estimate larger interfacial toughness as the crack is prompt to kink into the glass itself. The system was later improved to study heterogeneous planar interfaces [25]. By patterning a zone of strong interfacial toughness within a weaker one, it is still possible to force the crack to remain at the interface and measure stronger interfacial toughness.

Four-point bend test Another test is the four-point bend test. Two elastic solids are bonded together with another material such as an epoxy. A notch is created in the upper substrate so that a crack can develop and eventually kink at the interface upon loading. The weak interface can lie within one interface of a multilayer stack if previously deposited on one of the substrates. This test covers a wide range of applications from interfaces in thermal barrier coatings [26, 27] to a macroscopic scale for pavements [28]. General schematic is presented in Fig. 1.12.

Once the crack develops at the interface, the energy release rate reaches a steady state value. The energy release rate during stable fracture can be calculated using :

$$G = \frac{P^2 L^2}{8b}\left(\frac{1}{\Sigma_1} - \frac{1}{\Sigma_2}\right) \tag{1.15}$$

where P is the load upon which the crack propagate, L the spacing spacing between the inner and outer loading lines, b the sample width, Σ_1 is the beam stiffness of the upper substrate and Σ_2 is the lower substrate.

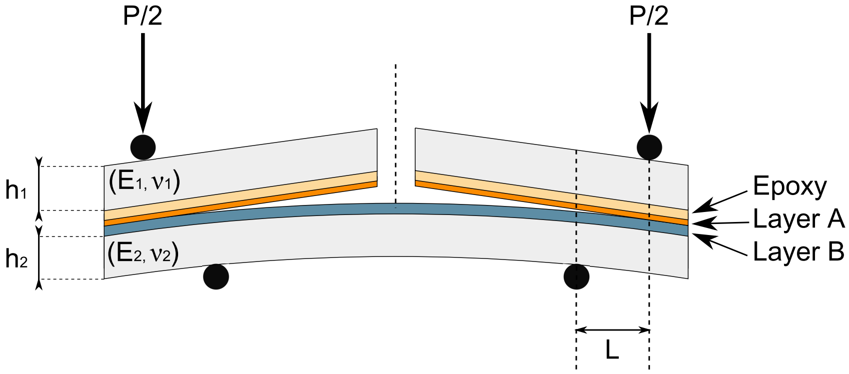

Figure 1.12: Four-point bend test.

In a four-point bend test the crack propagates in a mixed mode. This is due to asymmetry of the test and thus existence of a non-zero mode II component. The relative proportion of mode II and mode I strongly depends on the thicknesses and material properties of the elastic solids used for the test, see Fig. 1.13. The lowest mode II contribution is obtained for soft solid standing on a rigid solid of equal thicknesses ($h_1/h_2 = 1$) and corresponds to $\psi = 36°$. The highest mode II contribution is obtained for a purely rigid thin film on a soft and deep substrate. Such broad range of mode mixity imposes good control over elastic properties of the test. In case of no elastic mismatch between solids of equal thicknesses, the energy release rate is equal to

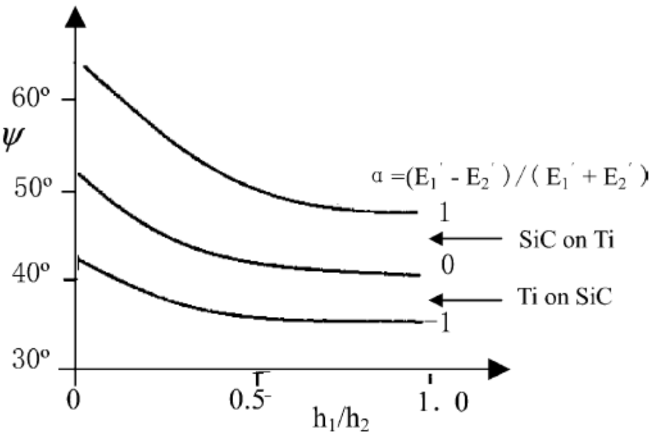

Figure 1.13: The dependence of phase angle on specimen size and elastic mismatch in four-point bending test, from Zou et al. [29]

$$G = \frac{21\left(1-\nu^2\right)P^2L^2}{16Eb^2h^3} \tag{1.16}$$

with $\psi = 43°$. Note that the fracture becomes unstable once the crack passes the lower support line. In such circumstances, numerical analysis should be used to compute G [30]. Note that none of the two tests described previously take into account the residual stress in thin films that can influence the mode mixity of the test.

Bulge test The bulge test uses the pressure from a fluid, such as air or water, as the driving force for delamination. It is commonly used to estimate the Young modulus of thin films [31] and more recently to estimate interfacial toughness [32, 33]. A hole is drilled through the substrate down to the chosen interface. A fluid is then pressed under the film until the interface crack initiates, see Fig. 1.14. Response of the film as a function of pressure for a given delamination radius provides information on the Young modulus. At the same time, by varying the pressure one can probe fracture propagation with different combinations of opening and sliding at the crack tip. Therefore the mode mixity may be varied from −45° to almost pure mode II. Calculation of the energy release rate is, for this test, rather complex in particular when elasticity of the substrate and residual stresses in the film are taken into account.

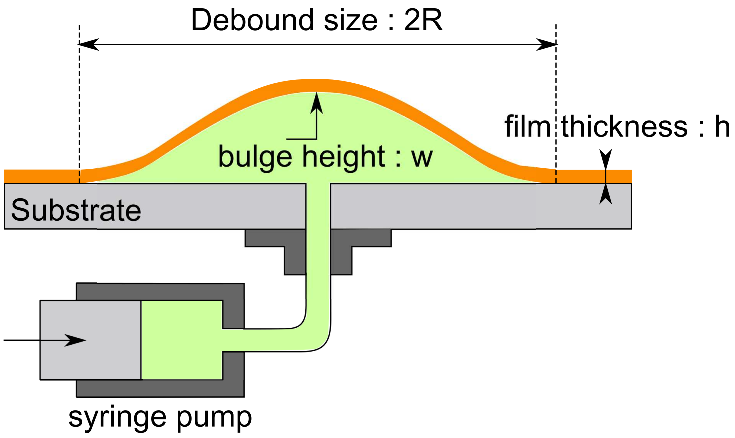

Figure 1.14: Bulge test

This non-exhaustive list of tests shows that in most of the tests mechanical properties of the film and the substrate are required. In addition most of them neglect the residual stresses in the film that can add sliding at the crack tip.

1.4 Strategy to study adhesion through buckling driven delamination

In general, the best test for thin film adhesion reproduces the actual conditions under which a multilayer fails. For multilayers based on silver, oxides and nitrides, buckles are a common defect when strong compressive residual stress and weak adhesion are combined. Buckles are an interesting way to measure adhesion as propagation of the interface crack and therefore the size of the blister is limited by the value of interfacial toughness.

However except in simple cases, the precise relation between buckle size and adhesion is not fully understood. This is the case especially for films with large residual stresses and leading to a common morphology of delamination : the TC blister. One way to identify such relation is to keep a constant interfacial toughness, say silver with the substrate, and load the interface crack at several values with a stressed overlayer, also named superlayer. The superlayer can store a certain amount of elastic energy by means of its thickness and in-plane stress and transmit the energy to the interface crack. Residual stresses allow to tune the elastic energy stored in a thin film at room temperature and for a constant film thickness. Molybdenum thin films exhibit large residual stresses and are perfect candidates for a superlayer.

The next chapter presents in detailed study of residual stresses in molybdenum thin film deposited by magnetron sputtering. Origin of the residual stress is discussed.

Bibliography

[1] P. Villa, A. Delagnes, and L. Wadley. *J. of Arch. Sci.*, 32:399–422, 2005.

[2] J.-M. Petillon and S. Ducasse. *J. of Human. Evol.*, 62:435–465, 2012.

[3] A. A. Griffith. The phenomena of rupture and flow in solids. *Phil. Trans. Roy. Soc. Long.*, A221:163, 1920.

[4] J. W. Obreimov. The splitting strength of mica. *Proc. Roy. Soc. Lond.*, A127:290, 1930.

[5] G. C. Sih, P. C. Paris, and G. R. Irwin. On cracks in rectilinearly anisotropic bodies. *Int. J. of Frac. Mech.*, 1:189–203, 1965.

[6] E. Lazzari and J. Jupille. Wetting and interfacial chemistry of metallic films on the hydroxylated $\alpha{-}\mathrm{al}_2\mathrm{o}_3$ (0001) surface. *Phys. Rev. B*, 71:045409, 2005.

[7] J.-S. Wang and Z. Suo. Experimental determination of interfacial toughness curves using brazil nut sandwiches. *Acta metall. mater.*, 38(7):1479–1290, 1990.

[8] D.S. Dugdale. Yielding of steel sheets containing slits. *J. Mech. Phys. Solids*, 8:100–104, 1960.

[9] G. I. Barenblatt. The mathematical theory of equilibrium cracks in brittle fracture. *Adv. Appl. Mech.*, 7:55, 1962.

[10] A. V. Zhuk, A. G. Evans, J. W. Hutchinson, and G. M. Whitesides. The adhesion energy between polymer thin films and self-assembled monolayers. *J. Mater. Res.*, 13:3555–3564, 1998.

[11] D. C. Meyer, T. Leisegang, A. A. Levin, P. Paufler, and A. A. Volinsky. Tensile crack patterns in mo/si multilayers on si substrates under high-temperature bending. *Appl. Phys. A*, 78:303–305, 2004.

[12] J. W. Hutchinson. *Acta metall. mater.*, 40(2):295–308, 1992.

[13] M.-W. Moon, H. M. Jensen, J. W. Hutchinson, K. H. Oh, and A. G. Evans. *J. Mech. Phys. Sol.*, 50:2355, 2002.

[14] C. Coupeau. Atomic force microscopy study of the morphological shape of thin film buckling. *Thin Solid Films.*, 406:190–194, 2002.

[15] I. Reimanis, B. J. Dalgleish, M. Ruhle, and A. G. Evans. *Acta. Metall.*, 38:2645, 1990.

[16] A. Furaya, N. Hosoi, and Y. Ohshita. *J. Appl. Phys.*, 78:598, 1995.

[17] D. Chatain, L. Coudurier, and N. Eustathopoulos. Wettability and adhesion of metallic liquids on ceramics in non-reactive and reactive systems. *J. Chem. Phys.*, 83:561, 1986.

[18] K. S. Gadrea nd T. L. Alford. Contact angle measurements for adhesion energy evaluation of silver and copper films on parylene-n and sio2 substrates. *J. Appl. Phys.*, 93:919–923, 2003.

[19] R. C. Hula, C. Edtmaier, and M. Holzweber. The wetting behaviour of silver on carbon, pure and carburized nickel, cobalt and molybdenum substrates. *App. Surf. S.*, 256:4697–4701, 2010.

[20] N. Rauch, E. Saiz, and A. P. Tornsia. Spreading of liquid ag and ag-mo alloys on molybdenum substrates. *Zeit. Metall.*, 94:233–237, 2003.

[21] J. W. Hutchinson and Z. Suo. *Adv. Appl. Mech.*, 29:63, 1992.

[22] E. Barthel, O. Kerjan, P. Nael, and N. Nadaud. Asymmetric silver to oxide adhesion in multilayers deposited on glass by sputtering. *Thin Solid Films*, 473:272–277, 2005.

[23] A. A. Volinsky, N. R. Moody, and W. W. Gerberich. *Acta Mat.*, 50:441–466, 2002.

[24] M. F. Kanninen. *Int. J. of Fracture*, 9:83, 1973.

[25] S. Patinet, L. Alzate, E. Barthel, D. Dalmas, D. Vandembroucq, and V. Lazarus. *J. Mech. Phys. Solids*, 61:311–324, 2013.

[26] P.-Y. Thery, M. Poulain, MI Dupeux, and M. Braccini. *Surf. Coat. Tech.*, 202:648–652, 2007.

[27] R. G. Hutchinson and J. W. Hutchinson. Lifetime assessment for thermal barrier coatings: Tests for measuring mixed mode delamination toughness. *J. Am. Ceram. Soc.*, 94:S85–S95, 2011.

[28] A. Chabot, M. Hun, and F. Hammoum. *Cons. Build. Mat.*, 40:1076–1087, 2013.

[29] L. Zou, Y. Huang, and C. Wang. *J. Eur. Ceramic. Soc.*, 24:2861–2868, 2004.

[30] I. Hofinger, M. Oechsner, H. Bahr, and M. Swain. *Int. J. Fract.*, 92:213, 1998.

[31] A. Karimi, O. R. Shojaei, T. Kruml, and J. L. Martin. *Thin Solid Films*, 308-309:334–339, 1997.

[32] A. Sofla, E. Seker, J. Landers, and M. R. Begley. *J. App. Mech.*, 77:031007, 2010.

[33] W. Zhou, J. Yang, Y. Lin, A. Ji, F. Yang, and Y. Yu. *Thin Solid Films*, 517:1989–1994, 2009.

Chapter 2

Residual stresses in molybdenum thin films

Molybdenum thin films have been used previously at the SVI laboratory to provide elastic energy to fracture a weak interface [1]. However no systematic study of the residual stress obtained was undertaken. Study of thin film delamination was limited by the unknown stress evolution as a function of thickness. In addition the range of elastic energy stored, and thus interfaces possible to break was limited by low residual compression obtained : $\sigma \approx 1.7\,\mathrm{GPa}$.

This chapter is dedicated to the study of residual stresses in molybdenum thin films deposited by sputtering. In particular it presents the impact of deposition parameters on the residual stress. The stress distribution through thickness has also been studied.

2.1 Thin films deposited by magnetron sputtering

2.1.1 Process

Magnetron sputtering has been used as an extremely flexible coating technique for decades. A wide variety of materials can be deposited from metals to ceramics. This technique, performed in vacuum, can create thin films with high purity and full-dense microstructure on a wide range of substrates. It also provides high deposition rates and good adhesion, reproducible topography, structure and other properties.

The principle in case of direct current (DC) magnetron sputtering is illustrated in Fig. 2.1. The sputtering system consists of two electrodes: a target made from the material to be deposited (cathode) and the substrate (anode). The deposition chamber is first pumped to a high vacuum, typically 1×10^{-5} Pa. An inert gas, typically argon, is then introduced at a given flux. The pumping rate and flux of argon control the deposition pressure. A negative voltage is supplied to the target (typically around 300 V in case of metallic target of 2 inches diameter), in order to

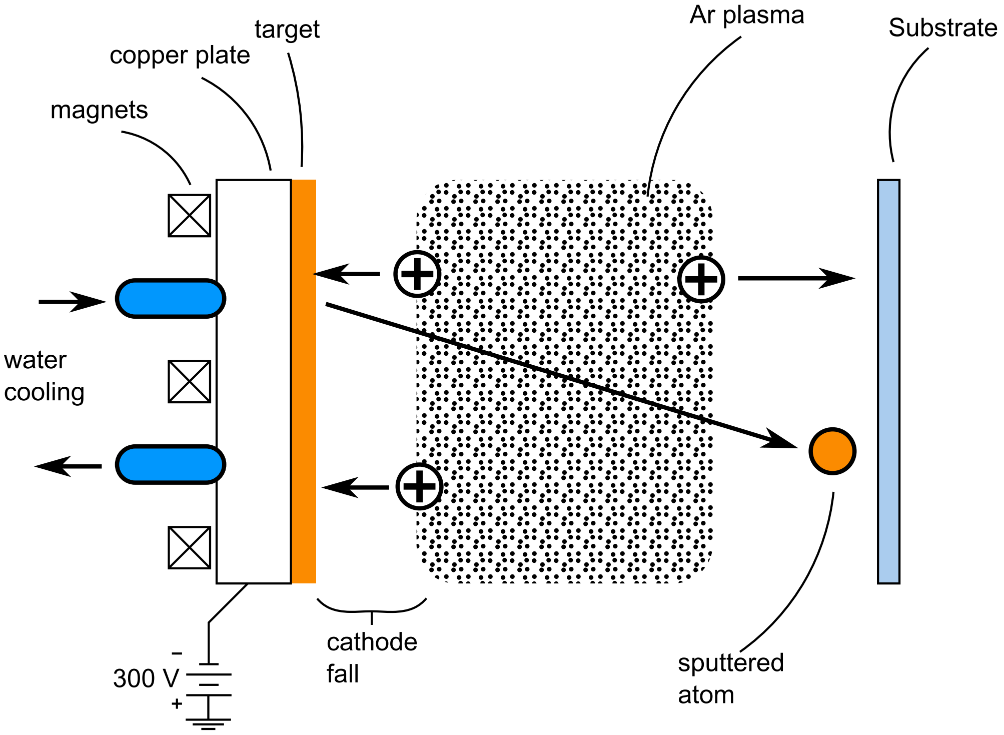

Figure 2.1: Schematic of magnetron sputtering system.

create a glow discharge. The working gas is ionized and positive ions are accelerated towards the cathode by the electric field. The incoming ions bombard the target and knock the target atoms out. A surface atom can be sputtered if the energy transferred normal to the surface is about three times its binding energy. In case of magnetron sputtering, the sputtering phenomenon is enhanced by a magnetic field generated by magnets underneath the target. The magnetic field traps free electrons near the target, colliding with neutrals to produce new argon ions.

Sputtered atoms travel through the chamber and condense onto a substrate, thus providing film growth. In case of reactive magnetron sputtering, another gas can be added to argon during deposition, such as nitrogen for Si_3N_4 or oxygen for ZnO. The deposition rate, or growth rate of the film can be controlled either by the applied power density to the target, or by the argon pressure and the target-substrate distance.

Depending on the deposition conditions and the state of the substrate, the material may grow monocrystalline, polycrystalline or amorphous, with or without preferred texture and orientation.

2.1.2 Growth of a thin film

We now consider the conditions under which a film may condense on the substrate and cause growth. The film growth process begins with a clean substrate surface at temperature T_s, exposed to a vapor of a chemically compatible film material, which is at temperature T_v. Let us consider a monocrystalline film, then to form such a film, atoms of the vapor must arrive at the substrate, adhere to it and settle at possible equilibrium positions before the structural defects are left behind the growth front. While forming an amorphous film they must be prevented from seeking stable equilibrium positions.

Through contact with the substrate surface, atoms in the vapor form chemical bonds with the substrate atoms reducing their energy. Hence, for film growth it is necessary that the vapor is supersaturated with respect to the substrate. Some of the adatoms may return to the vapor by evaporating. The adatoms distributed on the substrate have the character of a two-dimensional vapor. The deposited material thermalizes quickly and takes on the temperature T_s.

Most of the time each adatom on the surface resides within an equilibrium energy well, which is separated from the neighboring wells by a diffusion barrier. The atoms oscillate in their wells due to thermal activation and occasionally they can hop between the wells; the result of such jumps is the surface diffusion. In case of a spatially uniform surface, diffusion occurs randomly and the hopping rate increases with the substrate temperature. If temperature is very low, adatoms stick on the growth surface where they landed, and the film tends to grow with an amorphous or very fine grained polycrystalline structure.

The growth surface always has a distribution of surface defects, which provide sites of relatively easy attachment for adatoms. If the diffusion distance is large compared to the defect spacing, then adatoms encounter defects and become attached to them. This is the case of heterogeneous nucleation of the film growth. If the spacing of defects is larger than the diffusion length, migrating atoms can lower the energy of the system by binding together and forming clusters. The case of such stable clusters formation is called homogeneous nucleation of the film growth. For a film to form on a substrate, it is necessary that either nuclei formed by homogeneous processes are able to grow or that a sufficient number of surface defects are available to serve at sites of heterogeneous nucleation.

Film growth modes. The mode of film formation largely determines the eventual structure of the film, and is itself determined by the relative values of energies involved in the adatoms-surface interaction. With respect to energy aspects two types of growth can be distinguished. The Volmer-Weber (VW) growth, where adatom-adatom interactions are stronger than between adatoms and the surface, leads to the formation of three-dimensional clusters or islands. Growth of these clusters, along

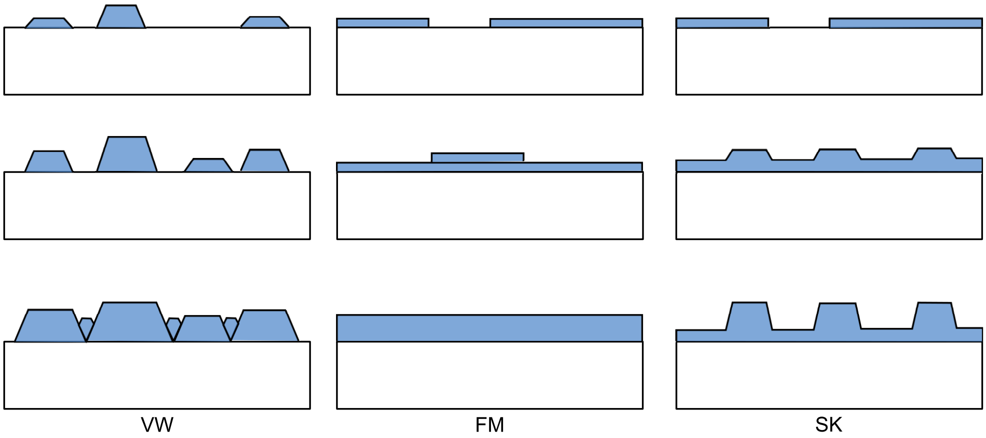

Figure 2.2: Schematic of growth mode for thin film. Left Volmer-Weber growth mode. Middle : Frank-Van de Merwe growth mode. Right : Stranski-Krastanov growth mode.

with coarsening, causes rough multi-layer films to grow on the substrate surface. This is the growth mode of silver and molybdenum thin films on alumina [2].

Opposite, during Frank-Van der Merwe (FM) growth, adatoms preferably attach to surface sites resulting in atomically smooth, fully formed layers. This layer-by-layer growth is two dimensional, indicating that complete films form prior to growth of subsequent layers.

Those two modes can combine for features of both 2D layer and 3D island growth, called Stranski-Krastanov (SK) growth. Transition from the layer-by-layer to island-based growth occurs at a critical layer thickness (highly dependent on the chemical and physical properties of the substrate and film), once the planar growth surface becomes established.

2.1.3 Mechanics of thin film

The growth mode of the thin film has several consequences on the mechanics of the film grown. Next, we will introduce defect formation and other phenomena which may lead to stresses in thin films. Two categories of film stresses are generally distinguished.

The first are stresses related to the growth process and are commonly called intrinsic stresses. These stresses strongly depend on the involved materials, substrate temperature during deposition, growth flux and chamber conditions. A progress in nondestructive methods for in-situ stress measurements (see part 2.1) made it possible to trace the evolution of the film properties and the corresponding average stresses during the film formation. This allowed subdividing the growth stresses in different categories: those which are associated with different growth stages and those which are present at the end of the process.

The second category represents stresses arising from changes in the physical environment of the film material during its growth. These externally induced stresses are commonly called extrinsic stresses. In many cases they arise when the film is bonded to the substrate, hence the distinction of growth and induced stresses is sometimes unclear.

The intrinsic stresses for certain growth conditions depend on many factors. Except for an ideal epitaxial case, the final structure is inevitably far from the equilibrium state, and there are a huge number of degrees of freedom involved in this metastable structure formation. Stresses occurring in films due to external influences also can arise from a multitude of effects such as annealing. For a review of common stress generation mechanisms see for instance Doerner and Nix [3].

For most film-substrate material combinations films grow in the VW mode, which leads to a polycrystalline microstructure. The connection between the stress and VW mode growth stages is not yet fully understood. However, the real-time stress measurement techniques have provided insights into the nature of the dynamic interplay between different physical mechanisms of structural evolution that induce or relax the internal stress. A general behavior for the stress is shown in Fig. 2.3. The mechanisms that can take place for the observed behavior are described in the following discussion.

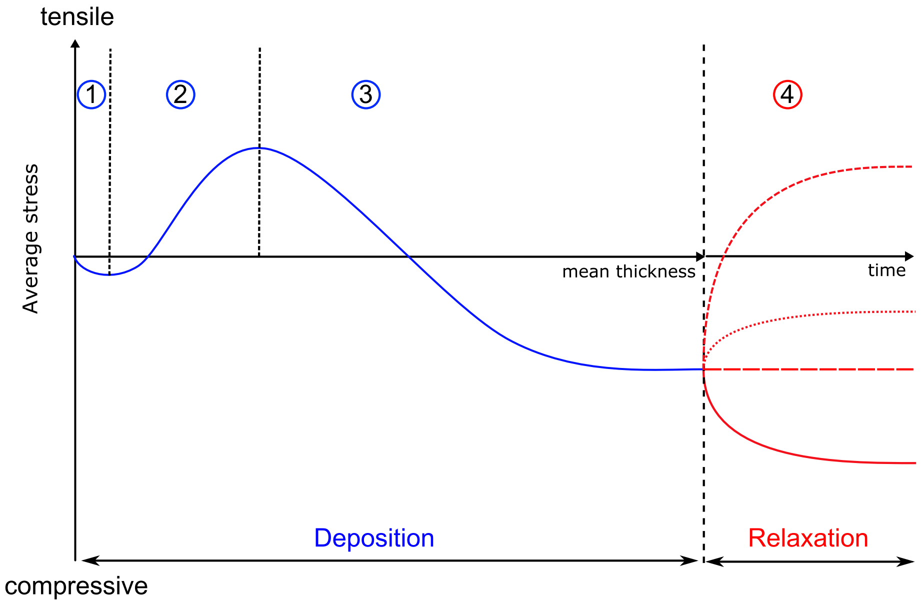

Figure 2.3: General behavior of the average stress in a thin film as a function of mean thickness (during deposition) and of time (after deposition). The first stage corresponds to early surface tension. The second stage corresponds to grain zipping. The third stage corresponds to the growth of a continuous thin film. The fourth stage corresponds to evolution of the stress after deposition.

Early surface tension. This stage corresponds to the first stage in Fig. 2.3. The compressive stress that arises early in the deposition process is usually attributed to the action of surface and/or interface stress and is explained by the fact that the lattice spacing in a very small isolated crystallite is smaller than the spacing in a bulk crystal of the same material at the same temperature, see Fig. 2.4. The magnitude of this effect can be estimated as a surface tension for the case of a homogeneous and isotropic spherical crystallite of radius R. If f is the isotropic surface stress acting on the spherical crystallite surface, then equilibrium requires the presence of internal stress acting throughout the crystal interior with a magnitude of

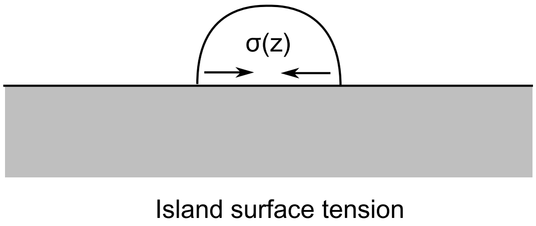

Figure 2.4: Early surface tension in thin films.

$$\sigma = -\frac{2f}{R} \tag{2.1}$$

At the early stage of film growth crystallites forming on the surface become firmly 'attached' to the substrate. Upon further growth in volumes of clusters, the internal elastic stress in the crystallites tends to relax because the cluster radius becomes larger. However, the internal strain is preserved due to the constraint of the substrate causing compression, see Fig 2.3 region 1. This mechanism was first proposed by Laugier [4].

Grain zipping. The most widely adopted model for the tensile stress origin is based on the works of Hoffman [5] and Doljack and Hoffman [6]. They suggested that small gaps between neighboring grains can close ('zip up') by forming grain boundaries (Fig. 2.5), and the energy released due to surface area reduction is converted to the elastic deformation of the participating grains required to the gap closure. It is therefore possible to identify very precisely the thickness at which a film starts percolating and at which thickness the percolation is finished. Percolation is figured by a dashed line between region 2 and 3 in Fig 2.3.

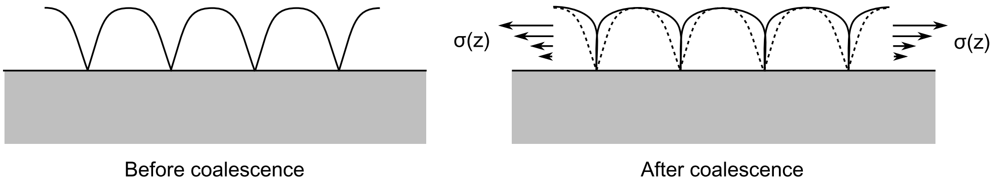

Figure 2.5: Grain zipping schematic.

Later stage. Shortly after arising, the tensile stress decreases in magnitude, yielding a growing compressive stress. For the high mobility materials the average stress in the film decreases until it takes on negative values. This indicates that the decrease involves not only a mechanism of tensile stress relaxation. Ultimately, the compressive stress approaches a steady value for the fixed growth flux and temperature.

Two additional observations may provide clues to the origin of the compressive stress. First, for the materials considered, if the growth is interrupted while the stress magnitude is at its plateau value, it falls off rapidly. Then, upon resumption of the deposition flux, the falloff in stress magnitude is fully reversed and the same compressive stress is re-established [7]. Second, it was demonstrated for the stress in Pd films deposited on polycrystalline Pt becomes compressive, while for the single crystal Pt wafers it remains tensile [8].

Apparently, the compressive stress arises in the film due to the excess number of atoms forming it. The available observations suggest that it probably depends on the deposition flux and the existence of grain boundaries in the film microstructure. Thornton and coworkers proposed the primary cause of compressive intrinsic stress during sputter deposition was *atomic peening*. Atomic peening is the process that induces damage at the surface due to bombardment of high energy atoms, named ion peening when charged particles are involved.

From the thermodynamic point of view, there is always a driving force, tending to expel excess atoms from the crystal under equilibrium conditions; however this may not be the case during the deposition. As was already mentioned, the growth flux provides adatoms which are supersaturated. Chason [9] proposed a model of compressive stress formation by the migration of adatoms into grain boundaries (that requires less energy, than to get into interstitial sites in the crystal). This is the mechanism playing a role after deposition is stopped.

Stress relaxation. The state of the stress in the film evolves for some time after deposition is stopped. Several scenarii are possible : relaxation towards tension, no relaxation and relaxation towards higher compression. We here use the term 'relaxation' because the general behavior of the film would be to minimize its stress amplitude, by different mechanisms such as the one previously described.

However, in some cases a large relaxation of a compressive film towards tension can cause the average film stress to be tensile [9]. As mentioned previously, one of the possible cause of such phenomenon is the film cooling after deposition. If the difference between the thermal expansion coefficients of the film, α_f, and the substrate, α_s is positive, then during a film cool down a average tensile stress $\langle\sigma_{th}\rangle$

will be generated for the film.

$$\langle \sigma_{th} \rangle = \frac{E_f}{1 - \nu_f} \left(\alpha_s - \alpha_f \right) \Delta T \tag{2.2}$$

The different mechanisms involved are highly dependent on the material chosen and a general approach is still lacking. However the evolution of stress during deposition can be monitored using the proper measurement technique to gain knowledge of film formation.

2.2 Measurement of stress

Several techniques can be used to measure the stress in thin film : XRD [10], raman spectroscopy [11] and curvature measurement. The last one takes advantage of the fact that strain in the film can cause uniform deformation of the substrate.

2.2.1 Curvature and stress measurement

The existence of residual stress in films deposited on substrates and its effects on delamination and cracking were recognized even in the nineteenth century. Later, in 1909, Stoney observed that a metal film deposited on a thick wafer was in a state of tension or compression with no external loads applied, which could lead to substrate bending. He suggested relating the stress in the film to the extent of this bending [12].

Suppose that a film is bonded to the surface of a substrate of uniform thickness t_s. It will be assumed that the substrate shape is a circular disk of radius R, but results can be extended to any shape. A cylindrical coordinate system (r, θ, z) is introduced with its origin at the center of the substrate with z-axis oriented perpendicular to the substrate faces, so the film is bonded to the face at $z = t_s/2$. It is assumed that the substrate thickness is thin compared to the in-plane dimension ($t_s << R$) and large compared to the film thickness ($t_s >> h$). Let be E_s, ν_s be the elastic modulus and Poisson ratio of the film respectively.

An isotropic membrane force f expressed in N.m^{-1} acts on the free standing film and its magnitude is either positive or negative, giving rise to a strain in the film. The strained film is then brought in contact with the substrate surface and bonded onto it, causing strain on the substrate that bends.

It is assumed that the substrate deforms in plane strain, axisymmetrically, $\sigma_{zz} = 0$, that linear elasticity can be applied and that the change in the membrane force f is small due to the bending of the substrate.

On the deformation itself, axial symmetry is assumed and edge effects are neglected. In such conditions, the curvature κ of the substrate midplane surfaces can be considered spatially uniform and the deformed shape of the midplane spherical. This is a good approximation provided that the material is nearly isotropic and the deformation is small.

Resolution can be found in [12], and leads to the Stoney formula that links the in-plane curvature to the membrane force applied to the film :

$$\kappa = \frac{6f}{\mu_s t_s^2} \tag{2.3}$$

If we convert the membrane force to the stress in the film $\sigma = f/h$ then

$$\sigma = \kappa \frac{E_s}{6\left(1-\nu_s\right)} \frac{t_s^2}{h} \tag{2.4}$$

The Stoney formula is of critical importance as it gives experimental access to measurement of the residual stress in thin films by measuring substrate curvature, provided that the limits stated above are not exceeded.

2.2.2 Strategy adopted for stress measurement

In general the measurement of the curvature is done on sample prior and after the deposition. Therefore a change in the substrate curvature can be estimated and the average residual stress σ^{avg} in the thin film calculated.

$$\sigma^{avg} = \left(\kappa_2 - \kappa_1\right) \frac{E_s}{6\left(1-\nu_s\right)} \frac{t_s^2}{h} \tag{2.5}$$

However this method cannot render the evolution of stress we mentioned above and a study of stress through thickness requires a large number of samples. One way found in the literature to overcome this problem is to etch away the material [13]. The stress dependence with thickness can then be monitored. Another way is to directly monitor the stress in-situ during growth. We propose to use the multi-beam optical sensor set-up used by Chason *et al.* in [9].

The change in curvature of the sample is monitored in-situ using a multibeam optical stress sensor built-in-house [14, 15] (MOSS), presented in Fig.2.6. A laser beam is split by a semi-reflective mirror. The mirror is a 2 mm thick glass with on one side a semi-reflective coating and on the other side a 100 % reflective coating. As the beam arrives at the surface of the mirror with an incoming angle $\theta \neq 0$, the miror generates multiple reflections with decreasing intensity spaced by a distance $l = 2h \tan\theta$. Spacing of the set of parallel beams can be tuned by controlling θ. The set of parallel beams reflect on the substrate surface with an incoming angle α. The curvature of the sample causes the beams to diverge. As long as the curvature κ of the sample remains small enough, $\kappa \leq 0.5$, α can be considered constant. The spot positions observed on a screen are linked to the curvature at a time t, as

$$\kappa\left(t\right) = \frac{\cos\left(\alpha\right)}{2L}\left(1 - \frac{D\left(t\right)}{D_{ref}}\right) \tag{2.6}$$

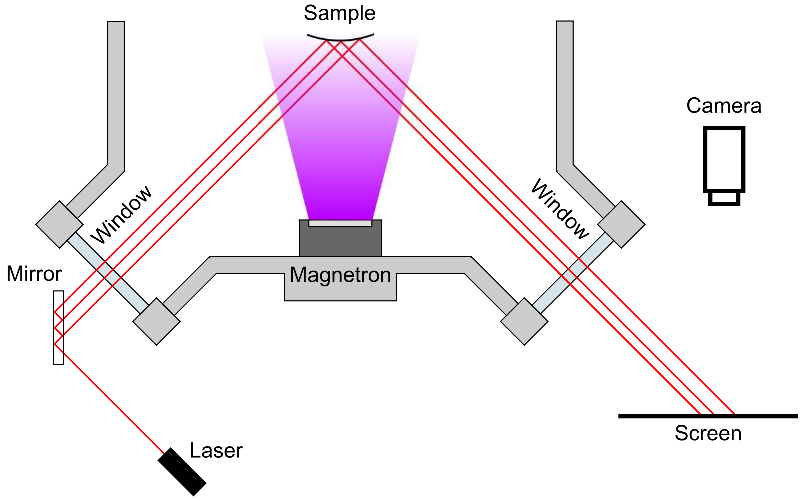

Figure 2.6: Schematic of deposition chamber and MOSS set-up.

where L is the distance between the sample and the screen, D_{ref} is the distance between spots for a flat substrate, and $D\left(t\right)$ is the distance between spots at instant t. D_{ref} was measured using a thick glass of 5 mm covered with a reflective layer of 100 nm of silver. If we combine (2.6) with the Stoney formula, the change in stress in the film can be expressed.

Digital image correlation is used to find the displacement of the spot on the screen. The maximum of correlation is found by fitting the correlation matrix locally by a second order polynomial surface and finding its maximum [16]. The new position (x, y) of the six spots are compared to the previous position to find the value of $D\left(t\right)$. All the treatment has been programmed with the software Igor Pro. In practice, the spot line is aligned with the CCD detector so that the number of pixel is maximized between two spots. The precision of the set-up can be expressed in term of minimum change of curvature detected.

$$\kappa_{min} = \frac{\Delta L_{min}}{\Delta y_{max}} \frac{1}{2L} \tag{2.7}$$

where Δy_{max} is the largest displacement for a laser spot, ΔL_{min} is the smallest laser motion detected. In our set-up, the maximum displacement for the laser spot is 5 cm. The smallest laser motion detected by image correlation is 1/10 pixel. Each pixel has a size of 0.05 mm×0.05 mm, which gives $\Delta L_{min} = 5\ \mu\text{m}$. The distance between the screen and the sample is $L = 0.957$ m. The precision is therefore $\kappa_{min} = 5.22 \times 10^{-5}\,\text{m}^{-1}$. Note that the precision over what stress can be detected is strongly dependent on the substrate chosen and especially its thickness. The samples presented in this work were sputtered on 2 inch Si wafers with a biaxial modulus $E_s/\left(1 - \nu_s\right) = 179.4$GPa at room temperature. Their thickness is determined with a precision of 5μm. Regarding the thin film deposited, their final thickness is measured by atomic force microscopy (AFM) using a step through the layer. Deposition rate

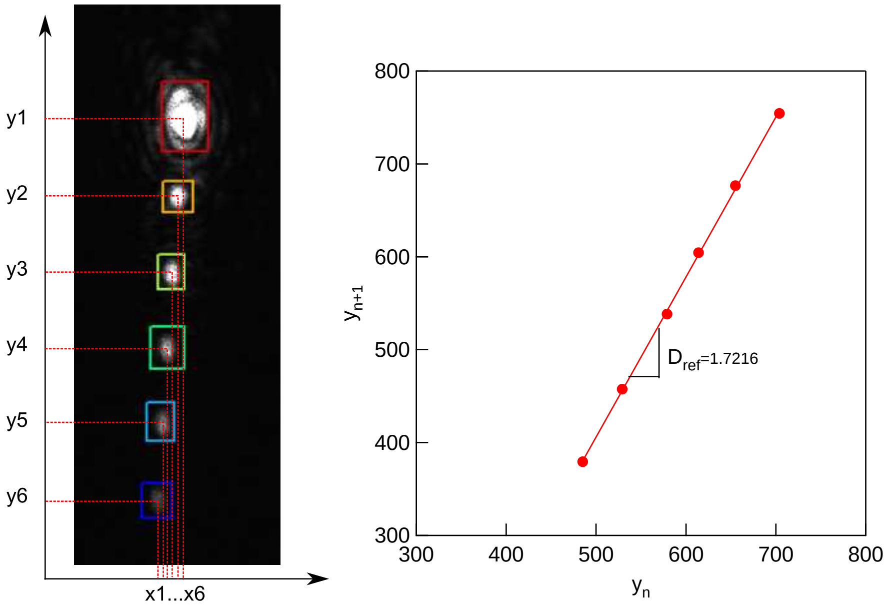

Figure 2.7: Spot position and calculation of elongation.

is assumed to be constant during deposition after the first seconds of deposition.

We obtain $\sigma^{avg} \times h$ curves. Each point on the curve corresponds to the average stress state times thickness of the stack at a given thickness. A positive value for $\sigma^{avg} \times h$ corresponds to a film in tension and a negative value corresponds to a film in compression.

If we neglect time evolution of stress during deposition, the derivative of the σ^{avg} curve at a given thickness corresponds to the stress, σ^{local}, of the material being added to the stack. Therefore if for a given thickness, $\sigma^{avg} \times h > 0$ and $\sigma^{local} < 0$ it means that the stack is in tension but that the new material being added is in compression.

Let z be the axis along the thickness of the film, and let's consider a thin layer of thickness dz, then the measured average stress is related to the local stress by

$$\sigma^{avg} = \frac{1}{h} \int_0^h \sigma^{local}(z)\, dz \tag{2.8}$$

By successively measuring the average stress, via (2.6), it is possible to evaluate the local stress. We discretize (2.8) and obtain an iterative formula for the local stress :

$$\sigma^{local}_{i+1} = \frac{1}{h_{i+1}} \left(\sum_1^{i+1} h_k \right) \sigma^{avg}_{i+1} - \frac{1}{h_{i+1}} \sum_1^{i} h_k \sigma^{local}_k \tag{2.9}$$

2.3 Highly compressively stressed molybdenum layer

The general study was driven towards understanding the stress development in molybdenum and how the compressive stress could be increased in order to provide enough elastic energy to break stronger interfaces.

Films were deposited by magnetron sputtering in a high vacuum chamber with a base pressure of 4×10^{-5} Pa. During deposition, the evolution of the curvature was recorded with the MOSS set-up described previously. For all molybdenum samples, $280 \pm 20\ \mu$m thick wafers were used.

2.3.1 Influence of the partial pressure of Ar

The first parameter we studied was the pressure. Deposition conditions can be found in Tab. A.1 in Appendix A. All deposition times are equal to 10min. The stress state of molybdenum thin film shows a clear evolution from compression to tension when the argon pressure is increased in the chamber. Note that the deposition rate is little impacted by the pressure. In order to understand how the shift in tension occurs, it is important to consider the microstructure of the films. In Fig. 2.9 we present the cross-section of the films obtained by SEM and the top surface of the films obtained by AFM. The amplitude of the AFM scans is the same (see the scale on the right), so that they can be compared. We first note that all films are polycrystalline and grow columnar, with a preferential orientation perpendicular to the substrate. No significant change in the grain size is noticeable by SEM or AFM imaging through the thickness of each sample and between the samples themselves. However the roughness of the film increases as the deposition pressure is increased.

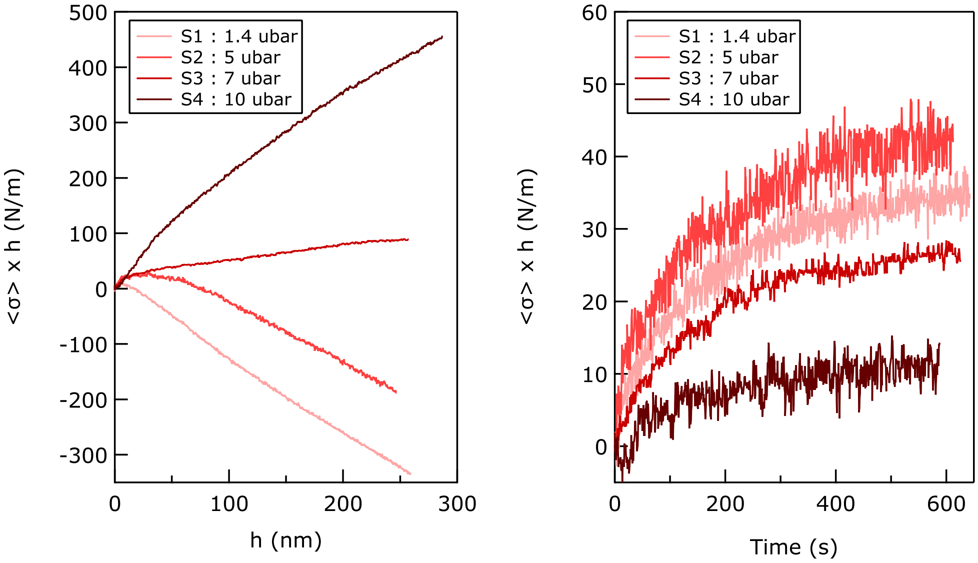

Figure 2.8: Evolution of $\sigma^{avg} \times h$ as a function of thickness during deposition (left) and as a function of time after deposition (right) for four different sputtering pressures.

On Fig. 2.8, the evolution of $\sigma^{avg} \times h$ after deposition is plotted. This is equivalent to the evolution of stress as the thickness stops evolving. Note that the stress values

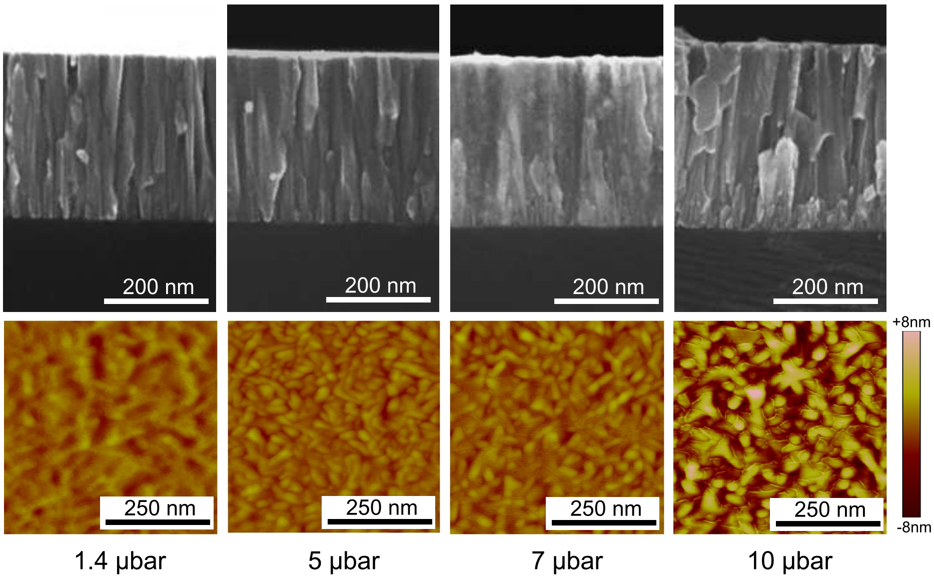

Figure 2.9: Scanning electron microscopy cross-section of samples sputtered at different pressures (top). Atomic force microscopy of the samples surface (bottom).

have the same origin for comparison purposes, and the scale is adjusted. We observe that stress in all films evolves towards more tension. For films in compression before deposition is stopped, it means the stress relaxes and for films in tension it means the stress amplitude increases. As a first approximation, we can fit the profile of relaxation with an exponential decay. The inverse of the characteristic time τ is representative of the speed at which the relaxation in the film occurs.

$$f(t) = A + B\exp(-t/\tau) \tag{2.10}$$

Study of τ shows that the relaxation occurs faster when the deposition pressure is increased. A similar evolution is found for roughness, as it increases with increasing pressure of argon. Regarding the amplitude of the relaxation, no trend can be drawn as the sample thicknesses are different and residual stress amplitudes before relaxation are different.

Evolution of stress and roughness can be explained considering the mean free path of the sputtered species.

$$\lambda = \frac{k_B T}{\sqrt{2}\pi d^2 P} \tag{2.11}$$

where k_B is the Boltzmann constant, T the temperature, d the atom diameter and P the pressure. For a typical molybdenum atom $d = 278$ pm. This gives a range of mean free paths at room temperature for the pressures tested from 8.6 cm for 1.4 μbar to 1.2 cm for 10 μbar. Similar values are obtained for argon atom. Those lengths should compare to the distance between the target and the sample which is, in our deposition chamber, 11 cm. For the lowest pressure we are therefore in a ballistic regime where very few collisions occur. Atoms and positive ions reach the sample surface with a wide range of energies up to 10 eV. This bombardment causes atomic and ion peening and thus compression [17].

As the pressure is increased, the mean free path of the atoms diminishes, introducing more collisions and more energy losses. The ion peening diminishes and so does the compressive component. Another result of the reduced mean free path is the wider angular distribution of molybdenum atoms arriving at the substrate [18] leading to enhanced roughness. This causes the shadowing effect.

Further experiments were conducted at the lowest argon pressure, 1.4 μbar, at which a plasma could be held and higher compressive intrinsic stress achieved.

2.3.2 Film relaxation

As we have seen previously in Fig.2.8, films tend to relax toward tension. The extent of relaxation and its rate are however critical in order to use residual stress (large and compressive) as a loading source for an interfacial crack. In this section we study the amount of relaxation as a function of thickness.

Five samples were deposited at the pressure 1.4 μbar, for which as the residual stress is large and compressive. Deposition lasted 1 to 5 min, leading to five different thicknesses. Evolution of $\sigma^{avg} \times h$ as a function of thickness during deposition is plotted in Fig. 2.10, left part. Above the percolation threshold we described previously, located around 10 nm for those films, whatever the thickness we here consider, the residual stress is compressive. The deposition rate is similar for the five samples and around $3.7 \pm 0.2\,\text{Å.s}^{-1}$. The amplitude of the residual stress above 20 nm is constant for the five samples and is equal to $\sigma^{avg} = -1.6 \pm 0.1$ GPa.nm.

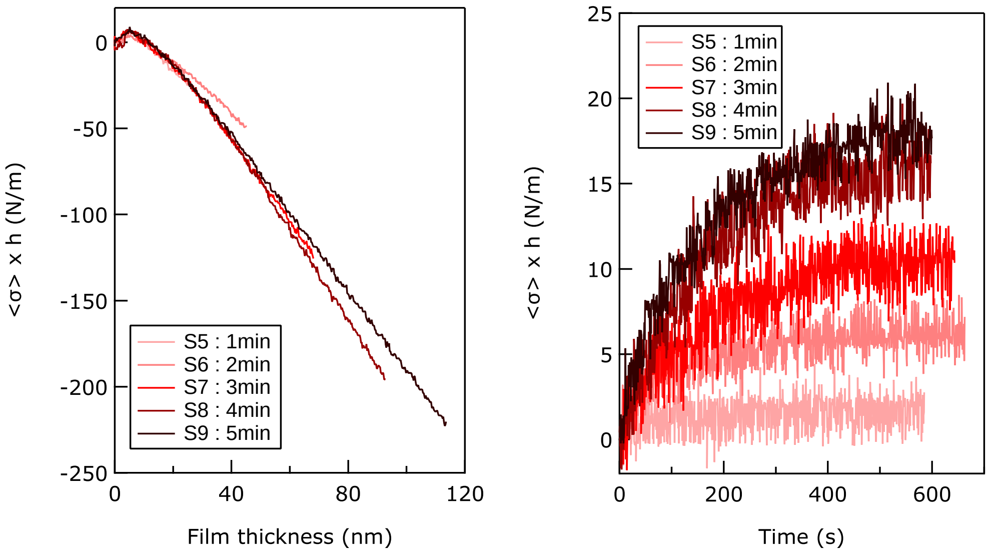

Figure 2.10: Evolution of $\sigma^{avg} \times h$ as a function of thickness during deposition (left) and as a function of time after deposition (right) for four different sputtering times.

The residual stress is therefore reproducible from sample to sample for the same conditions of deposition within this limit.

In Fig. 2.10, right part, the evolution of $\sigma^{avg} \times h$ is plotted after deposition. Curves are offset to zero when deposition is stopped. We observe that all films relax towards tension. The amplitude of relaxation increases as the thickness deposited is increased. We use the same exponential fit than Eq. 2.10. Fitting shows that the amplitude of relaxation tends to be 10% of residual stress whatever the thickness for the recipe considered. Evolution of τ is plotted as a function of deposition time in Fig. 2.11 We observe that when the thickness of the films are increased, the relaxation occurs more slowly with a characteristic time of around 3 min. It is here important to distinguish the effect of the surface and the bulk on relaxation of residual stresses. The surface aspect measured by AFM of the molybdenum films for different thicknesses is presented on Fig. 2.12. We observe that after two minutes of deposition, grains are visible and few differences in size are visible at those thicknesses. Roughness is calculated from AFM scans and presented in Fig. 2.10

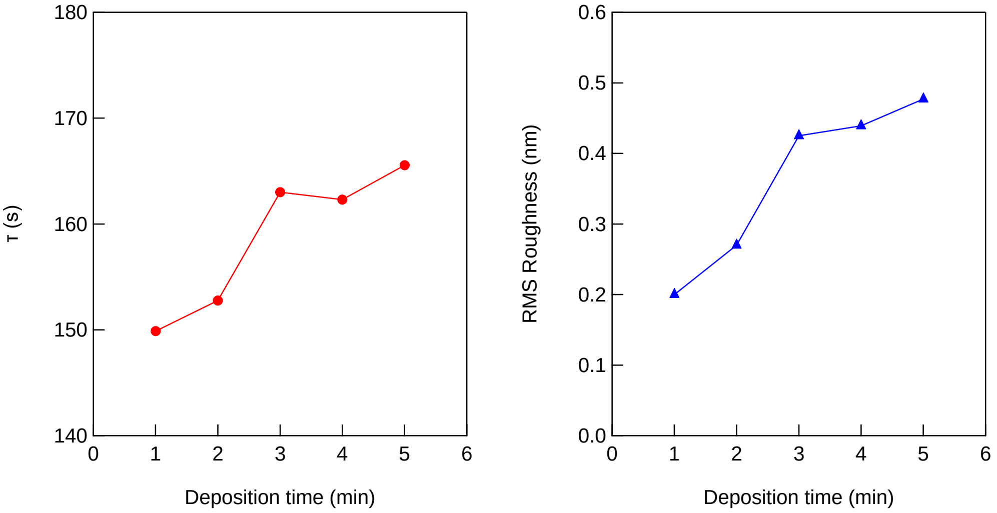

Figure 2.11: Characteristic relaxation time τ as a function of deposition time (left). RMS roughness as a function of deposition time (right).

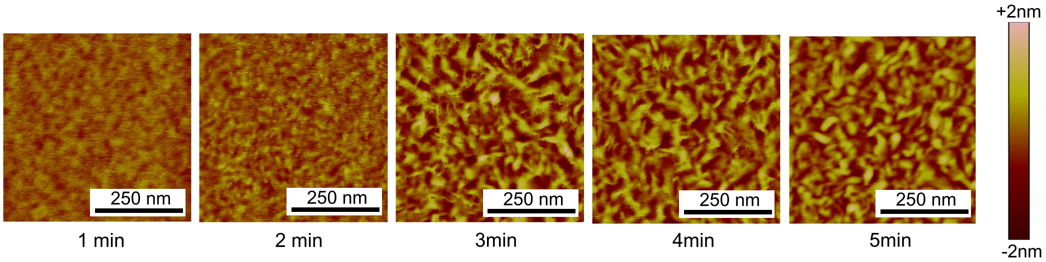

Figure 2.12: Atomic force microscopy image showing the evolution of the surface when sputtering time is increased.

(right). The roughness increases with deposition time. There is a good correlation between the relaxation time and the roughness. This could indicate that surface relaxation plays an important role for those films. However as both are linked to the thickness, it is difficult to identify any surface effect. The role of temperature should not be neglected either. Longer deposition time lead to higher temperature and therefore longer cooling time.

2.3.3 Influence of a bias potential at the substrate

In order to increase the ion peening mechanism, one way is to accelerate ions towards the sample by applying a bias potential, so that the general bombardment is increased. We studied the influence of bias potential in the range of 0 V to −75 V. Such value should compare to the floating potential measured at −22.5 V. Detailed conditions of the samples sputtered can be found in Tab. A.2 in Appendix A. We show in Fig. 2.13 the $\sigma^{avg} \times h$ curves for four different bias potentials as a function of deposition time. The deposition rate was measured for the four samples and is constant at $4.0 \pm 0.2\,\text{Å.s}^{-1}$. All the sputtered samples exhibit large compressive residual stress at the end of deposition. The lowest compressive residual stress is achieved for 0 V, and the largest is achieved for −75 V. At low thickness, the films are more compressive than at higher, whatever the potential. As the deposition conditions are kept constant besides the bias potential, we attribute the change in stress to the influence of bias on the charged, positive species in the plasma, namely Ar^+ and Mo^+. Applying a negative bias to the substrate, we create an electrical field which accelerates the positive species, see Fig. 2.1 towards the sample increasing the ion peening effect and thus compression.

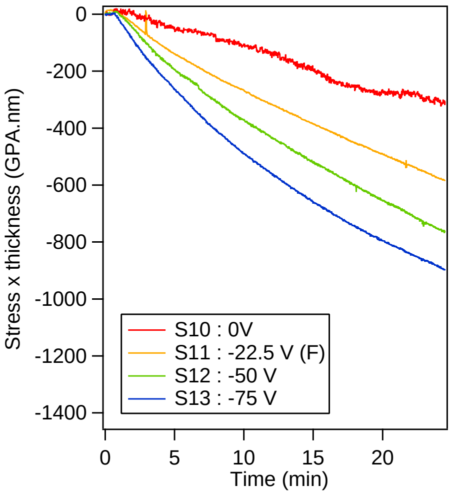

Figure 2.13

2.3.4 Influence of oxygen

Reactive sputtering of molybdenum thin films with oxygen gas was studied at low flux of oxygen ranging from 0 sccm to 6 sccm. The general idea is here to dope the film of molybdenum with oxygen so that the residual compression in the film can be enhanced.

Oxygen doping. We first studied the influence of oxygen doping on the mechanical properties of molybdenum films. The first graph presents the final value of the average stress state of the film for different oxygen flux and two different potentials, see Tab. A.4 in Appendix A for detailed conditions.

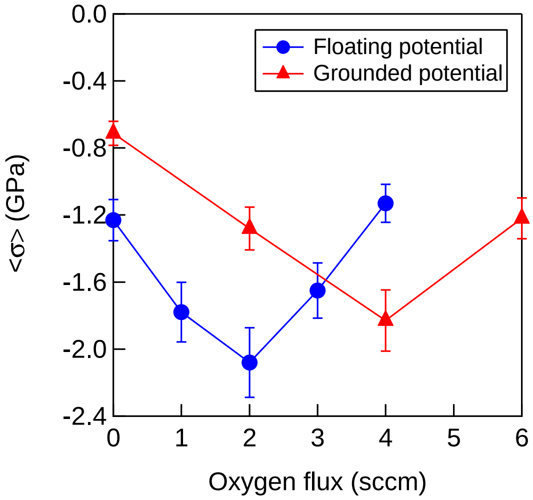

Figure 2.14

We note that all films deposited at floating potential are under compression and that a maximum of residual compressive stress can be found at around 2 sccm of O_2. When the substrate is grounded, all films remain in compression but the maximum in compression occurs at higher level of O_2 doping. Those results are obtained for films sputtered for 15 min whose thicknesses can be found in Tab. A.4 in Appendix A. As the stress evolves through the thickness, it is important to look at the distribution of stress to know if the oxygen doped films are always more compressive than the pure molybdenum films. We will do this comparison at two different potentials : -22.5 V (floating) and -75 V.

In Fig.2.15a, we plot results obtained in the previous section for pure molybdenum but as a function of thickness. We observe that the stress is always compressive. As the film thickness increases, the value of compressive stress decreases. When a potential of -75 V is applied to the substrate, the stress becomes more compressive with larger compression at small thickness.

In Fig.2.15b, oxygen is added during the deposition. At floating potential, the stress is also compressive but lower at small film thickness than in the oxygen-free film. When we apply a potential of −75 V to the sample during growth, we observe the same trend with an overall average compressive stress higher than in the floating potential case.

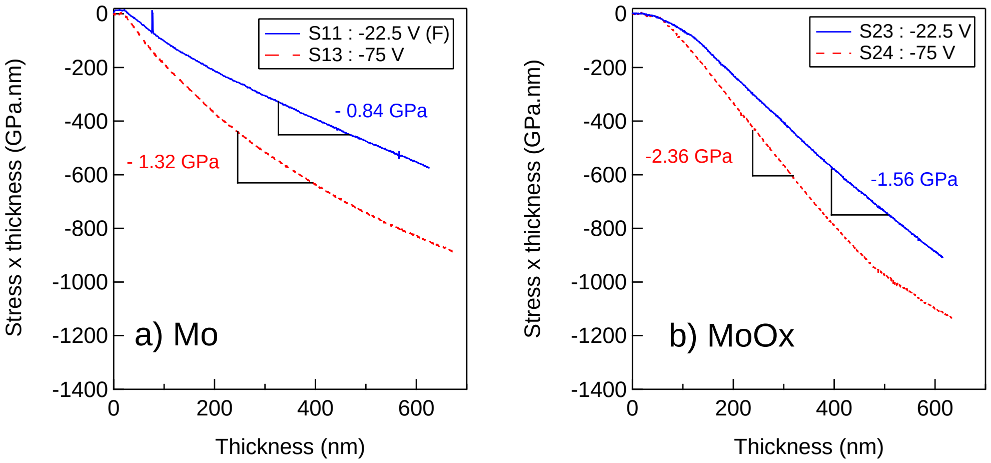

Figure 2.15: Influence of the substrate potential on stress in molybdenum thin film for (a) no oxygen and (b) 2 sccm of oxygen.

Film microstructure. We studied the films microstructure in cross section using SEM which are displayed in Fig. 2.14. We can see that all the samples exhibit columnar grain structure. The structure remains columnar when a potential of −75 V is applied. However, the addition of oxygen in the MoO_x leads to a reduction of the grain size and at the interface with the substrate, the columnar structure of the film has not developed. This layer close to the interface appears amorphous or nanocrystalline. Root mean square roughness and film thickness, measured by AFM, of four characteristic films are presented in Table. 2.1. We observe that the deposition rate varies by about 10% depending on the deposition conditions. The roughness of the pure molybdenum samples increases when the substrate potential is decreased. For MoO_x films, the roughness is higher when the potential is left floating (−22.5 V). In MoO_x films, grains are small at the interface and the stress observed is less compressive than for Mo films.

X-ray diffraction. XRD was performed on the four samples to study their crystallographic orientation. Resulting XRD patterns are shown in Fig. 2.17. All samples exhibit the (110) peak showing that all films are grown as a molybdenum bcc crystalline solid. The presence of stoichiometric oxides, such as MoO_3 phase, are not detected, indicating that the oxygen in the molybdenum films is in interstitial position and confirms that we have doped our Mo films with oxygen.

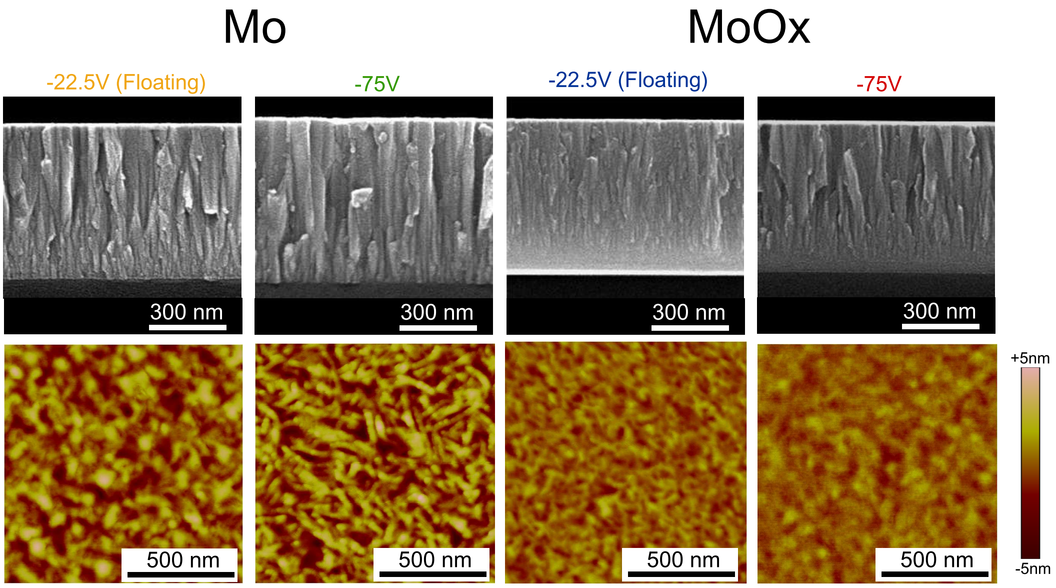

Figure 2.16: FEG-SEM images showing the influence of substrate potential and oxygen doping on the microstructure of molybdenum thin films. Local stress versus thickness is plotted for each sample. Top left Mo at floating potential, top right Mo at −75 V, bottom left Mo with 2 sccm of O_2 at floating potential and bottom right Mo with 2 sccm of O_2 at −75 V.

Sample	S11	S13	S23	S24
Material	Mo	Mo	MoO_x	MoO_x
Potential (V)	-22.5 (F)	-75.0	-22.5 (F)	-75.0
Thickness (nm)	626.1	671.0	633.0	615.6
Roughness (nm)	6.3	10.8	9.9	4.3

Table 2.1: Thickness and roughness of five characteristic samples. Deposition times are equal.

Significant differences are observed for films grown with and without oxygen. The full width at half maximum (FWHM) can be calculated from the spectra presented in Fig.2.17. The smallest FWHM is obtained for pure Mo at −75 V with 0.28° whereas the value for pure Mo at floating potential is slightly higher 0.32°. The peaks are broader for MoO_x films with a FWHM of 0.66° and 0.63° for Mo with 2 sccm of O_2 at floating potential and Mo with 2 sccm of O_2 at −75 V respectively. The broadening of x-ray diffraction peaks can usually be attributed to the small grain size or the defects in the thin film [19]. When a negative potential is applied during growth of pure Mo, grain size is larger which results in a narrowing of the diffraction peak. This effect is also observed when films are grown with oxygen. From the grain structure of the Mo grown with oxygen presented in Fig. 2.16, we know that the columnar grain size does not differ much between pure and oxidized

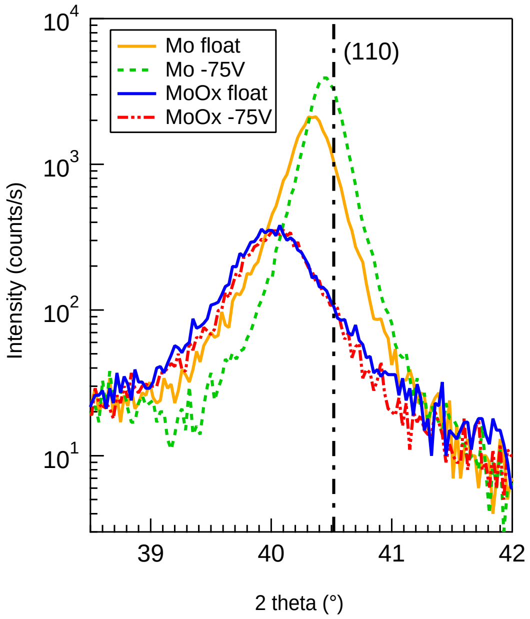

Figure 2.17: XRD spectra. Dashed line represents the location of the (110)peak of molybdenum.

film. However the large broadening of the peaks is likely to indicate a greater concentration of defects in the films, such as oxygen interstitials.

Film composition. In order to further understand the influence of oxygen on the micro structure of our films, we performed Time of Flight Secondary Ion Mass Spectroscopy, ToF-SIMS, on our samples. This technique uses pulsed ion beam to sputter the sample. The ionized sputtered species are then accelerated in a tube. Due to the difference in masses and by measuring their time of flight from the sample, it is possible to identify the sputtered species. As matter is sputtered in a cone shape, it is less precise when the cone deepens as both surface and deep species are sputtered. This technique is efficient for surface based application. Measurements presented were performed on a TOF-SIMS IV from Ion-Tof and Cs^+ ions are the sputtering species.

Concentrations of oxygen through the thickness of the films are presented in Fig. 2.16. We observe that all four samples have a peak of oxygen concentration due to the native oxide of the silicon substrates. Results are normalized to the position of this peak, as the interface reference. Inside the molybdenum film, to the left of the peak of SiO_2, we can distinguish the samples deposited with oxygen as they have between 3 and 10 times higher oxygen concentration through the film than the films deposited without oxygen. The concentration in oxygen is also higher for the films sputtered with floating potential than with the fixed potential of $-75\,V$. This can be explained by the fact that negative oxygen ions are repelled by the applied

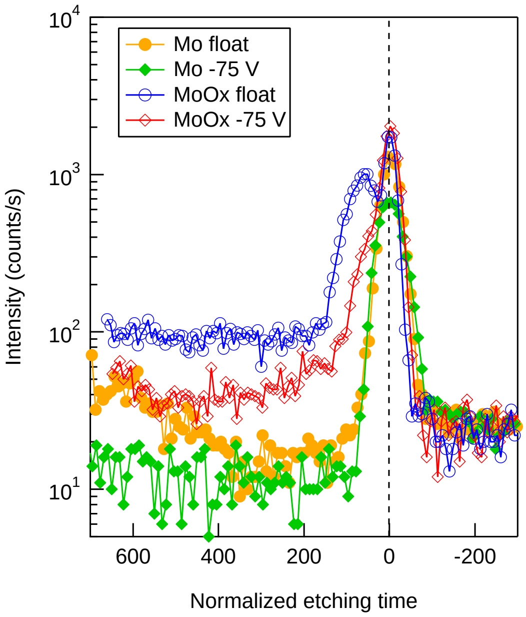

Figure 2.18: ToF-SIMS measurement of oxygen concentration of the same four samples as Fig.2.16. Dashed line represents the SiO_2 peak of the substrate interface. MoO_x films have high oxygen concentration at the interface.

potential during deposition.

We can also observe a high concentration of oxygen, ten times higher than in the rest of the sample, next to the interface with the substrate in both MoO_x films. The oxygen concentration in the film remains high up to a certain thickness. When we compare the concentration profile of oxygen with the cross-section of the MoO_x films in Fig.2.16, the oxygen-rich layer corresponds to the nanocrystalline layer and the lower concentration corresponds to the columnar structure.

2.3.5 Discussion

Our results on the influence of oxygen doping on molybdenum thin film suggest that the oxygen content and the microstructure drive the local stress generation. These phenomena can be discussed in relation to the deposition conditions.

The mean free path of atoms with the deposition pressure used (~ 0.22 Pa) is of the order of 10 centimeters or more while the distance between the target and the sample is set to ~ 11 cm. In such conditions the atoms and positive ions [20, 21] reach the sample surface with a wide range of energies reaching up to 10 eV. The oxygen negative ions are accelerated in the electric field and this acceleration leads to a distribution in energy up to 300 eV [22]. Such energies are characteristic of the so-called "ballistic" regime at low processing pressures. The high energy species normally cause the formation of dense films which are often under compression (atomic or ion peening effect [23]).

All these effects seem to play a role in the formation of our Mo and MoO_x films. The increase of the average compressive stress in the film with the increase of the negative potential is attributed to the more energetic positive ions bombardment (Ar^+, Mo^+). When the potential is switched to the ground, the bombardment from positive species is reduced and less compression is developed. Such behavior has been reported previously for chromium thin films [24].

In the case where a columnar microstructure is observed, the presence of oxygen in the plasma also adds to the compression in the film. This is due to incorporation of O atoms in interstitial sites of Mo lattice. Such mechanism by O contamination of pure Mo films has been reported [25]. Remarkably, increase of the negative potential results in higher compression, but lower oxygen content in the film. This can be due to the fact that O^- ions with energies below 75 eV are being repelled by the negative potential on the sample and do not reach the surface. The bombardment by the positive ions, however, is increased like in the case of oxygen-free deposition, which results in still higher compression in the film.

The formation of an amorphous or nanocrystalline interface layer with relatively small stress when oxygen is added to the plasma is not easily explained. One of the plausible explanations is that oxygen directly inhibits the Mo adatoms mobility. This results in the formation of smaller grains with higher density of grain-boundaries. Since the grain-boundaries often cause the tensile stretching of the grains, this effect might have negated the compressive stress due to ion-peening. The high grain boundary density in the nanocrystalline layer and the order of magnitude difference in oxygen concentration between this layer and the columnar structure indicates different sticking coefficient of oxygen during deposition and that most of the oxygen is likely to lie within the grain boundaries.

Stress behavior under increasing oxygen flux can be interpreted considering the change in microstructure from columnar to amorphous. For small amount of oxygen, the film structure remains columnar and O^- bombardment results in the increase of compression observed for both potentials. For a higher flux of oxygen, a less compressive nanocrystalline layer close to the interface is formed. The average compression in the film is therefore reduced.

As the films get thicker, the average stress generally decreases. Partly, this could be due to the heating of the sample by ion bombardment and subsequent relaxation of defects. Large grains with increasing thickness may also play a role. One of the consequences of the grain growth is the appearance of voids at the grain boundaries, which could cause relaxation of the compressive stress.

2.4 Conclusion

In this chapter we presented the influence of pressure, potential and oxygen doping on residual stress in molybdenum thin films. The microstructural state of the films was linked to oxygen doping and residual stress level. These results provide recipes to tune residual stress in molydenum. In particular, bombardment of argon should be increased to provide more compression. Control of the residual stress through oxygen doping is more difficult to achieve as the microstructure is greatly impacted at low film thicknesses. However compression achieved in those conditions are very high.

The maximum compression achieved is around 2.5 GPa for a thickness of 400 nm. Such film can be used to provide elastic energy $\approx 5\,\mathrm{J.m^{-2}}$ to an interface and cause delamination.

Bibliography

[1] S.Yu Grachev, A. Mehlich, J.-D. Kamminga, E. Barthel, and E. Sondergard. High-throughput optimization of adhesion in multilayers by superlayer gradients. *Thin Solid Films*, 518:6052–6054, 2010.

[2] E. Lazzari and J. Jupille. Wetting and interfacial chemistry of metallic films on the hydroxylated $\alpha-\mathrm{al_2o_3}\,(0001)$ surface. *Phys. Rev. B*, 71:045409, 2005.

[3] D. F. Doerner and W. Nix. *CRC Critical Review in Solid State and Materials Sciences*, 14:225–268, 1988.

[4] M. Laugier. *Vacuum*, 31:155–157, 1981.

[5] R. W. Hoffman. *Thin Solid films*, 34:185–190, 1976.

[6] F. A. Doljack and R. W. Hoffman. *Thin Solid films*, 12:71–74, 1972.

[7] A. L. Shull and F. Spaepen. *J. App. Phys.*, 80:6243–6256, 1996.

[8] V. Ramaswamy, M. A. Phillips, W. D. Nix, and B. M. Clemens. *Mat. Sci. and Eng.: A*, 319-321:887–892, 2001.

[9] E. Chason, B. W. Sheldon, and L. B. Freund. Origin of compressive residual stress in polycrystalline thin films. *Phys. Rev. Letters*, 88:156103, 2002.

[10] B. Panicaud and J. L. Grosseau-Poussard. *App. Surf. Sci.*, 257:1282–1288, 2010.

[11] M. Kemdehoundja, J. L. Grosseau-Poussard, and J. F. Dinhut. *App. Surf. Sci.*, 255:2719–2725, 2010.

[12] G. G. Stoney. *Proc. of the Royal Soc. of London*, A82:172–175, 1909.

[13] G. C. A. M. Janssen, A. J. Dammers, V. G. M. Sivel, and W. R. Wang. Tensile stress in hard metal films. *Appl. Phys. Lett.*, 83:3287, 2003.

[14] J.A. Floro, S.J. Hearne, J.A. Hunter, P. Kotula, E. Chason, S.C. Seeel, and C.V. Thompson. *J. of App. Phys.*, 89:4886, 2001.

[15] A. Fillon, G. Abadias, A. Michel, and C. Jaouen. *Thin Solid Films*, 519:1655, 2010.

[16] P.-C. Hung and A. S. Voloshin. In-plane strain measurement by digital image correlation. *J. of the Braz. Soc. of Mech. Sci. and Eng.*, XXV:215, 2003.

[17] D. W. Hoffman and J. A. Thornton. The compressive stress transition in al, v, zr, nb and w metal films sputtered at low working pressures. *Thin Solid Films*, 45:387–396, 1977.

[18] T. Hino, Y. Makabe, Y. Hirohata, and T. Yamashina. Surface roughness of mo films prepared by magnetron sputtering. *Thin Solid Films*, 229:201–206, 1993.

[19] B.E. Warren. *X-Ray Diffraction.* Addison-Wesley Publishing Co., 1969.

[20] D. Herrmann, M. Oertel, R. Menner, and M. Powalla. *Surf. Coat. Technol.*, 174-175:229, 2003.

[21] N. Martin, A.M.E. Santo, R. Sanjines, and F. Levy. *Surf. Coat. Technol.*, 138:77, 2001.

[22] Petr Pokorny, Jiri Bulir, Jan Lancok, Jindrich Musil, and Michal Novotny. *Plasma Process. Polym.*, 7:910, 2010.

[23] F.M. d Heurle. *Metallurgical Transactions*, 1:725, 1970.

[24] G.C.A.M. Janssen and J-D. Kamminga. *Appl. Phys. Lett.*, 85, 2004.

[25] L.P. Kendig, Z.U. Rek, S.M. Yalisove, and J.C. Bilello. *Surf. Coat. Technol.*, 132:124, 2000.

Chapter 3

Cohesive zone model for buckling driven delamination

Residual stresses in thin films can be a driving force for delamination. Under compression, buckling of the film occurs concomitantly to the propagation of a fracture at the interface and results in the so called buckling-driven delamination. This problem can be approached considering equilibrium of the crack front in the final pattern.

Study of the equilibrium of the post-buckling regime is however not sufficient to explain complex patterns such as the telephone cord like blisters, where the final pattern results from successive equilibria of the crack front. For these reasons, a model for buckling driven delamination needs to couple non-linear elastic response of the film and propagation of the crack front.

This chapter presents several models to describe the delamination of a thin film, and the simple case of a straight sided delamination post-buckling regime is taken as a first example. In the first part we describe available models for the film buckling and how they are coupled to the interface. In the second part we couple the film buckling with a cohesive zone, cf chapter 1, at the crack front. In the last part we present numerical results for the cohesive zone model and how they compare to the classical case without cohesive zone.

3.1 Buckling driven delamination of thin films

Buckles can be seen as an equilibrium state of a film under compression. Previous works in the literature have focused on the morphology resulting from such minimization. The most simple solution for the post-buckling equilibrium for a band of width $2b$ is the straight sided blister. In the following section we will take the straight sided blister as an example for comparison purpose between the different models. More complex delamination patterns are treated in the next chapter.

3.1.1 The straight sided blister : a post-buckling solution

The delamination of a thin film of width $2b$ can be treated as a thin plate clamped to the substrate at its edge, see Fig.3.1. This problem has been solved in the literature in [1] and stability of the post-buckling solution has been studied in [2]. We will here recall the assumptions made and the main results that may be derived. Let the thickness of the plate be h and its elastic properties given by E_f and ν_f for its elastic modulus and Poisson ratio respectively. The film is loaded with an initial isotropic compressive load, intensity N_0, before buckling along x and y directions. N^0 is the stress tensor in the initial state and $N^0_{xx} = -N_0$ the stress along x and $N^0_{yy} = -N_0$ along y. N_{xx} denotes the variation with respect to the fundamental plane state. Then the final post-buckling stress state is $N^f_{xx} = N^0_{xx} + N_{xx} = -N_0 + N_{xx}$. The displacement field is noted (u, v, w). In Cartesian coordinates, the Föppl Von Kármán (FvK) equations take the form :

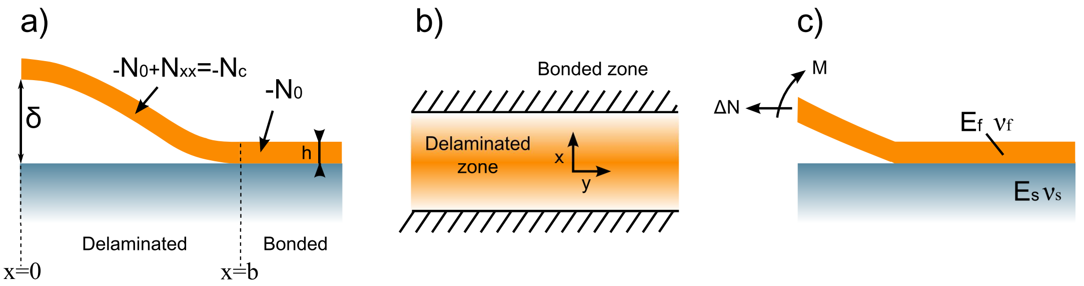

Figure 3.1: *a.* Half geometry for the straight sided blister. *b.* Geometry for the y-independent delamination extending between $-b \leq x \leq b$ and $-\inf < y < +\inf$. *c.* Crack tip loads under plane strain conditions.

$$\frac{\partial^4 w}{\partial x^4} + \frac{N_0 - N_{xx}}{D}\frac{\partial^2 w}{\partial x^2} = 0 \tag{3.1}$$

where $D = \bar{E}_f h^3/12$ is the bending stiffness of the film. We apply Hooke's law and take into account the fact that the shape of the solution is invariant along y, so that the strain is

$$\begin{cases} \dfrac{\partial u}{\partial x} + \dfrac{1}{2}\left(\dfrac{\partial w}{\partial x}\right)^2 = \dfrac{1}{Eh}(N_{xx} - \nu N_{yy}) \\ \\ N_{yy} = \nu N_{xx} = cte \end{cases} \tag{3.2}$$

The boundary conditions for resolution of Eq.3.1 are

$$\begin{cases} w\left(x=\pm b\right)=0 \\ \\ w'\left(x=\pm b\right)=0 \\ \\ w\left(x=0\right)=\delta \end{cases} \tag{3.3}$$

Then, the solution of Eq.3.1 is

$$\begin{cases} w\left(x\right)=\dfrac{1}{2}\delta\left[1+\cos\dfrac{\pi x}{b}\right] \\ \\ \dfrac{N_0-N_{xx}}{D}=\dfrac{\pi^2}{b^2} \end{cases} \tag{3.4}$$

Then comes immediately from Eq.3.4 that the residual stress is constant in the delaminated part of the straight sided blister $\sigma_c=\left(N_0-N_{xx}\right)/h$ is also equal to the critical buckling stress of a plate of width $2b$.

$$\sigma_c=\frac{\pi^2}{12}\frac{E}{1-\nu^2}\left(\frac{h}{b}\right)^2 \tag{3.5}$$

Normalizing $\sigma_0=N_0/h$ by σ_c from Eq.3.5, we get a convenient way to estimate the loading applied to the straight sided blister. σ_0/σ_c is called the loading ratio.

With Eq.3.2 using the condition $u\left(x=\pm b\right)=0$ and combining with Eq.3.4, we obtain the relation between the maximum out-of-plane displacement and the loading ratio σ_0/σ_c of the straight sided blister.

$$\frac{\delta}{h}=\sqrt{\frac{4}{3}\left(\frac{\sigma_0}{\sigma_c}-1\right)} \tag{3.6}$$

It is also convenient to define the minimum half width of a blister so that the plate may buckle up, i.e. for the loading ratio $\sigma_0/\sigma_c=1$

$$b_0=\frac{\pi}{\sqrt{12\left(1-\nu^2\right)}}h\sqrt{\frac{E}{\sigma_0}} \tag{3.7}$$

3.1.2 Equilibrium of the crack front

Once the post-buckling solution has been calculated it is interesting to consider what happens to the crack front at the edge of the blister. In order to ensure stability of the crack front at equilibrium, i.e no further propagation, the Griffith criterion implies that the energy release rate G is equal to the interfacial toughness G_c.

The energy release rate G can be calculated from the expressions of the moment M and the traction N_{xx} and re-expressed in terms σ_0 and σ_c. The calculation has been fully detailed in [1, 2] and we simply give here the final expression for G.

$$G = \frac{1}{2}\frac{1-\nu^2}{E} h \left(\sigma_0 - \sigma_c\right)\left(\sigma_0 + 3\sigma_c\right) \tag{3.8}$$

This expression exhibits a maximum for $\sigma_0/\sigma_c = 3$ when the loading ratio becomes large and G approaches G_0 which is the strain energy per unit area in the film which is available when released, subject to no shape variation along y.

$$G_0 = \frac{1}{2}\frac{1-\nu^2}{E} h \sigma_0^2 \tag{3.9}$$

Eq.3.5 reveals that a large loading ratio is equivalent to a large buckle width when thickness and in-plane compression are constant. Equivalently, G vanishes for values of the loading ratio under 1, where buckling is not possible.

Mixed-mode loading Another result may be derived from the straight sided solution : it is the stress field at the crack tip. The stress field is influenced by both the particular geometry of the blister and the material properties of the system considered. Those contributions create a mode mixity at the crack tip. In our problem, we need to consider an opening stress field normal to the plane of rupture, i.e. mode I, and a shear stress field along the rupture plan, i.e. mode II.

Let 1 be the axis normal to the plane of rupture, therefore normal to our interface where the rupture is confined, and 2 the axis normal to the crack tip in the plane of rupture. Using Eq .1.10, we can express the stress field as a function of the stress intensity factors in mode I, K_I and mode II, K_{II}.

$$\begin{cases} \sigma_{22} = \dfrac{K_I}{\sqrt{2\pi r}} \\[2ex] \sigma_{12} = \dfrac{K_{II}}{\sqrt{2\pi r}} \end{cases} \tag{3.10}$$

Relative proportion of mode II with respect to mode I, already defined in chapter 1 (Eq. 1.12), is given by ψ the angle of mode mixity.

$$\tan\psi = \frac{K_{II}}{K_I} \tag{3.11}$$

The expression for the stress intensity factor may be calculated for the edge crack of a thin film deposited on a substrate [1], in terms of moment and tension. The edge of a straight sided blister is a similar situation. The main contribution for K_I and K_{II} arises from the moment M applied by the film at the edge and the tension in the film $\Delta N = N_{xx}$ respectively, see Fig.3.1 for notations of the crack tip problem. However, another contribution arising from the elastic mismatch between the film and the substrate needs to be taken into account in the calculation of the stress intensity factors.

Effect of elastic mismatch. The contribution arising from the elastic mismatch between the substrate and the film may become an important aspect of the problem in particular cases. This effect is taken into account with the phase factor ω in the expression of K_I and K_{II} that depends on the Dundurs parameters α and β, that characterize the elastic mismatch.

$$\begin{cases} \alpha = \dfrac{\bar{E}_f - \bar{E}_s}{\bar{E}_f + \bar{E}_s} \\ \\ \beta = \dfrac{1}{2}\dfrac{\mu_f\left(1-2\nu_s\right) - \mu_s\left(1-2\nu_f\right)}{\mu_f\left(1-\nu_s\right) - \mu_s\left(1-\nu_f\right)} \end{cases} \tag{3.12}$$

where $\mu_i = E_i/\left(2\left(1+\nu_i\right)\right)$. Note that in the case that will be further treated where the thickness of the substrate is considered large in comparison to the film thickness and purely rigid, the values of α and β become

$$\begin{cases} \alpha = -1 \\ \\ \beta = \dfrac{1}{2}\dfrac{1-2\nu_f}{1-\nu_f} \end{cases} \tag{3.13}$$

In case of a molybdenum thin film where $\nu_f = 0.31$ we have $\beta \approx 0.275$. This corresponds to $\omega \approx 50°$. In regards, in case of no elastic mismatch between the substrate and the film we have $\alpha = 0$, $\beta = 0$ and $\omega \approx 52.1°$. The no-elastic mismatch case is the one generally treated in the literature. For precise computation of the phase factor the reader may refer to the work of Z. Suo [3]. We will here simply point out the fact that few differences between the case without elastic mismatch and a purely rigid substrate case will arise from the material properties through ω.

Taking into account the effect of M, N_{xx} and ω one may express K_I and K_{II} for the crack front at the edge of a straight sided blister in the general case,

$$\begin{cases} K_I = -\sqrt{\dfrac{1-\alpha}{1-\beta^2}}\left(\dfrac{N_{xx}}{\sqrt{2h}}\cos\omega - M\sqrt{\dfrac{6}{h^3}}\sin\omega\right) \\ \\ K_{II} = -\sqrt{\dfrac{1-\alpha}{1-\beta^2}}\left(\dfrac{N_{xx}}{\sqrt{2h}}\sin\omega - M\sqrt{\dfrac{6}{h^3}}\cos\omega\right) \end{cases} \tag{3.14}$$

Using Eq.3.14, Eq.3.11 and replacing the expressions of N_{xx} and M by their values, the mode mixity at the edge of the straight sided blister simply rewrites as :

$$\tan\psi = \frac{4\cos\omega + \sqrt{3}\left(\delta/h\right)\sin\omega}{-4\sin\omega + \sqrt{3}\left(\delta/h\right)\cos\omega} \tag{3.15}$$

As already mentionned in chapter 1 (Eq. 1.11), the energy release rate is the sum of the mode I contribution G_I and the mode II contribution G_{II} that are linked to the stress intensity factor,

$$G = G_I + G_{II} = \left(K_I^2 + K_{II}^2\right) \frac{1-\beta^2}{2\left(1/\bar{E}_f + 1/\bar{E}_s\right)} \tag{3.16}$$

At this point we can plot in Fig. 3.2 the evolution of the mode mixity at the edge of the blister as a function of the loading ratio using Eq. 3.15 and 3.6. We observe that the mode mixity is negative. Upon buckling, i.e. when $\sigma_c = \sigma_0$, the mode mixity is already below $-40°$. This means that for the straight sided blister, the mode II component is always present and the shear contribution is almost 50% in terms of traction at its minimum. The mode mixity further increases, as absolute value, towards more mode II until it reaches pure shear at $\sigma_0/\sigma_c \approx 6.7$ in case of an infinitively deep rigid substrate. Note also the weak dependence of the mode mixity on the material parameters as the boundary for the mode mixity remain similar.

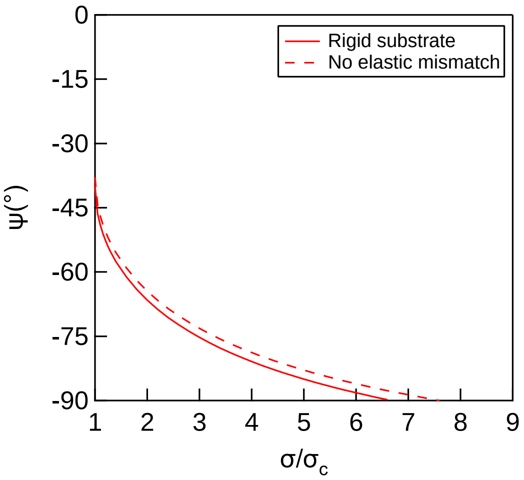

Figure 3.2: Mode mixity at the edge of the straight sided blister as a function of the loading ratio for a infinitively deep rigid substrate, with $\beta = 0.255$ and in case of no elastic mismatch.

So far we have treated the problem independently from the interfacial toughness and in terms of equilibrium. However in order to form a blister the delamination needs to propagate and this is especially true for the edge of straight sided blister.

3.1.3 Mode mixity dependence of the interfacial toughness

We now consider the stability of the buckle, and therefore stability of the crack front. Following the Griffith criterion, a crack front propagates if $G \geq G_c$ where G_c is the interfacial toughness. Let's suppose that $G/G_c > 1$, from Eq. 3.5 and Eq. 3.8, it is clear that b will increase until $G/G_c = 1$. The consequence of the increase of b

is the increase of the loading ratio and therefore increase of the mode mixity on the side of the blister. The reason for G/G_c to decrease may arise from Eq.3.8 above $\sigma_0/\sigma_c = 3$. This is a minor effect. However another reason might be the dependence of the interfacial toughness to the mode mixity.

We find in the literature several evidences for a mode dependence of the interfacial toughness at the interface between two solids [4, 5, 6, 7]. In particular, Liechti and Chai [8] have shown that for an interface between two bulks made of epoxy and glass, a mode dependence of the interfacial toughness exists and results in higher values of G_c when shear is applied. The lowest value of G_c is obtained for $\psi = 0°$ and the highest for $\psi = \pm 90°$. The distribution is not exactly symmetric for positive and negative values of ψ.

The origin of the mode mixity of the interfacial toughness is still unknown and may not be unique, as mentionned in chapter 1. Several causes are invoked in the literature such as roughness [9] and plasticity at the crack tip [10]. Roughness or asperities on the fracture surfaces will cause contact behind the crack tip when a mode II component exists in the loading. Tadepalli et al showed in [11] that the resulting roughness of a fracture interface in copper-copper bonds as well as the interfacial toughness increases when the mode mixity of the loading is increased.

Based on experimental observations, Evans and Hutchinson have proposed in [9] a model for the dependence of G_c that corrects the value of the mode I toughness G_{c_I} by a function $f(\psi)$ symmetric with respect to $\psi = 0°$ given below.

$$G_c(\psi) = G_{Ic} f(\psi) = G_{Ic}\left(1 + \tan^2(\eta\psi)\right) \tag{3.17}$$

where η is determined by $G_c(\pi/2) = G_{IIc}$. We plot on Fig. 3.3 the evolution of the function chosen for G_c as a function of ψ for several values of η. The case

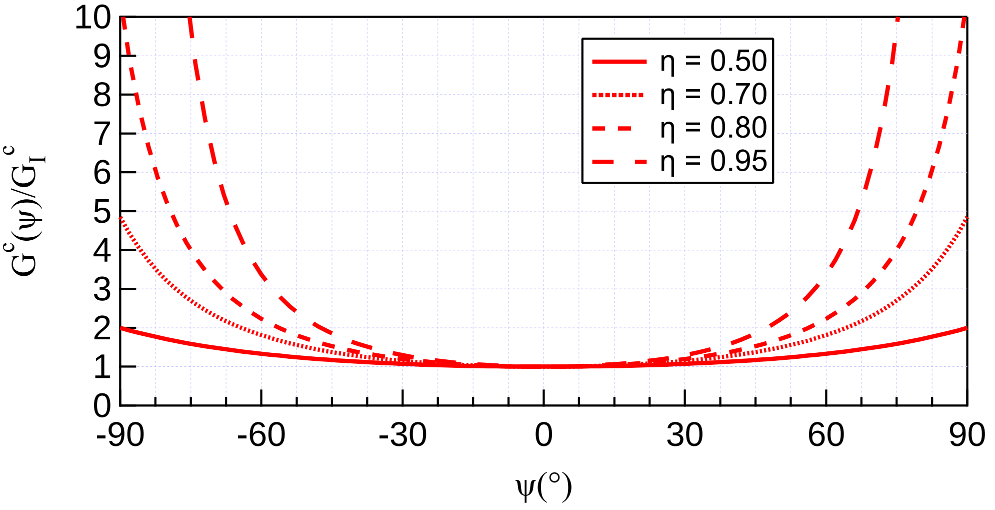

Figure 3.3: Interfacial toughness as a function of the mode mixity for several values of η

$\eta = 0$ corresponds to an interfacial toughness independent of the mode mixity and therefore $G_c(\psi) = G_{Ic}$.

The dependence of G_c on ψ has a consequence on the propagation of the blister. The more the blister propagates or widens, the higher the mode mixity on the side and the higher the interfacial toughness. The consequence is that G/G_c decreases readily when b increases at large b. In Fig. 3.4 we plot mode adjusted crack driving force as a function of the loading ratio for several values of η. The influence of the mode dependence is a strong decrease of the effective driving for rupture of the interface. Note that for $\eta = 0.5$, the driving force is half the one available without mode dependence and that $\eta = 0.95$ almost ensures that the driving force will drop to zero when pure mode II is reached at $\sigma_0/\sigma_c \approx 6.7$.

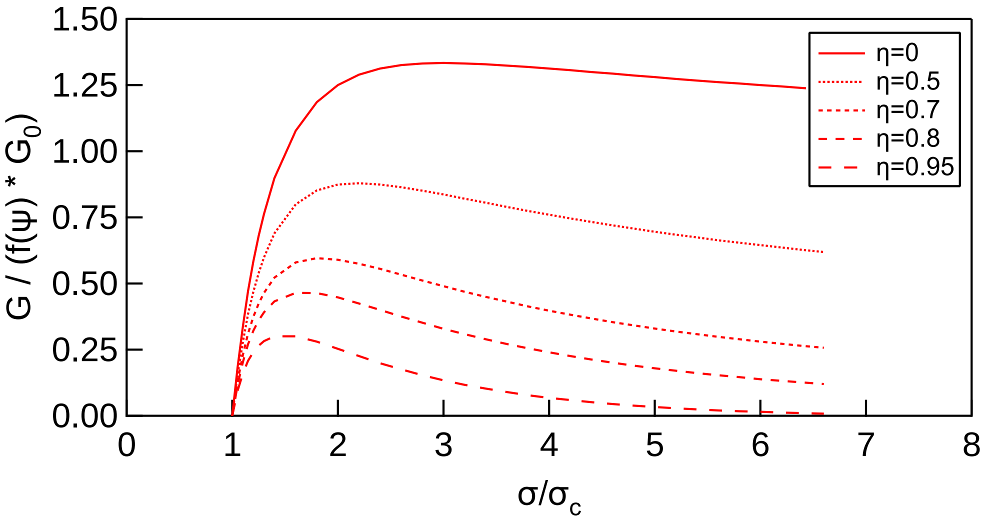

Figure 3.4: Mode adjusted crack driving force as a function of the loading ratio for several values of η.

3.1.4 Limitations and strategy adopted to study buckling driven delamination

We have presented previous works on the straight sided blister treated as an equilibrium state, where the global deformation is coupled to the local crack tip and then to the interfacial toughness. This model is suited for the straight sided blister and also for the circular blister [1] in particular because increase of b or equivalently the radius of the circular blister, R, leaves the shape of delamination unchanged. It gives excellent indication of the relation of b with the parameters of the interface. Experimentally it is found that, under equi-biaxial loading, such configurations are highly unstable [2, 12]. We present in Fig. 3.5 the destabilization of the delamination front of a circular blister and transition from a straight sided blister. Destabilization of the circular blister is obtained by applying different annealing temperatures to a

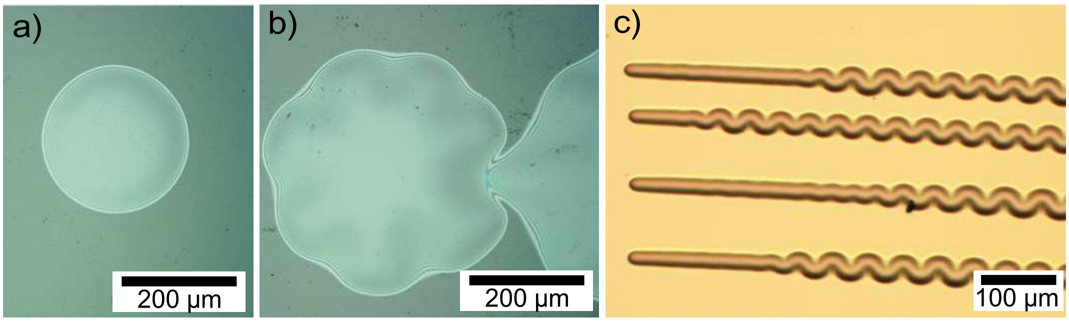

Figure 3.5: *a*. Delamination in circular blister of a Si_3N_4 film standing on glass after annealing. (A. Benedetto) *b*. Destabilization of a circular blister of Si_3N_4 standing on glass at higher annealing temperature. (A. Benedetto) *c*. Transition between straight sided blister and telephone cord like blister at the edge of a sample, molydenum thin film on silver-silicon interface.

Si_3N_4 thin film on glass, resulting in different thermal residual stress. The transition from the straight sided blister to the telephone cord may be observed at the edge of a sample of molybdenum thin film standing on a silver-silicon interface. The edge of the sample causes an anisotropy in the stress field large enough to stabilize a straight sided blister. Further away from the edge, equi-biaxial compression results into a telephone cord like blister. Similar results have been obtained considering destabilization of a plate of width $2b$ at large loading either experimentally by Moon et al. [13], analytically by B. Audoly [14] or numerically by Parry et al. [15] using finite elements modeling of the non-linear response of the plate.

The most common morphology under equi-biaxial loading remains the telephone cord like blister, see Fig. 3.5. This morphology is complex and it is not possible to determine easily the state of the crack front and the local mode mixity. Without taking into account the interfacial toughness and its mode dependence it has not been possible to study the formation of the delamination pattern from an initial defect and the influence of the interfacial toughness.

In order to answer these questions, we propose a model to study propagation of the buckling driven delamination. The three dimensional model couples non-linear plate buckling with a cohesive zone at the crack front. Such coupling has been recently used to model delamination of thin films on compliant substrate [16, 17], in the case of a straight sided blister in two dimensions [18] and even more recently in three dimensions [19] to model formation of blisters of metal film on compliant substrates in the transverse direction of uni-axial tensile traction.

The following section illustrates the use of cohesive zones by analytical resolution treating the simple case of a straight sided blister.

3.2 Analytical resolution for a straight sided blister

We propose to change the boundary conditions at the side of the straight sided blister previously solved and to replace the clamped conditions at $x = \pm b$ by a condition of cohesive zone of length Λ. New notations are given in Fig.3.6. Considering the problem is symmetric, we will therefore distinguish three parts in the problem. For $0 \leq x \leq b - \Lambda$ the film is fully detached from the substrate and free to buckle up, this part will be called free-buckled area, or delaminated area. For $b - \Lambda \leq x \leq b$ the interface is loaded with a cohesive stress T but has not been yet fully broken. This zone is the cohesive zone or process zone of the crack. For $b \leq x$ the interface is left unchanged and the plate unbuckled.

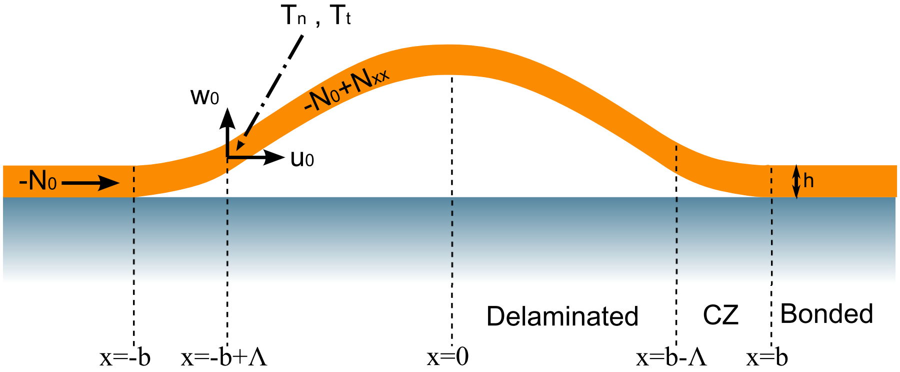

Figure 3.6: Straight sided blister with cohesive zone

3.2.1 Free-buckled area

We first solve the FvK equation, given in Eq. 3.1 on the delaminated area, $0 \leq x \leq (b - \Lambda)$. Therefore

$$\frac{\partial^4 w}{\partial x^4} + \frac{N_0 - N_{xx}}{D} \frac{\partial^2 w}{\partial x^2} = 0 \tag{3.18}$$

The solution is symmetric and has the following shape

$$w(x) = c_1 cos(\alpha x) + c_2 \tag{3.19}$$

The new boundary conditions are $w(b - \Lambda) = w_0$ and $w(0) = w_m$ we have :

$$\begin{cases} c_1 = \dfrac{w_m - w_0}{1 - \cos(\alpha(b - \Lambda))} \\ \\ c_2 = \dfrac{w_0 - w_m \cos(\alpha(b - \Lambda))}{1 - \cos(\alpha(b - \Lambda))} \end{cases} \tag{3.20}$$

Using boundary conditions on u and symmetry along y we obtain :

$$\begin{cases} \dfrac{\partial u}{\partial x} + \dfrac{1}{2}(\dfrac{\partial w}{\partial x})^2 = \dfrac{1}{Eh}(N_{xx} - \nu N_{yy}) \\ \\ N_{yy} = \nu N_{xx} \end{cases} \tag{3.21}$$

Replacing Eq. 3.19 in Eq. 3.21, we have

$$\frac{\partial u}{\partial x} + \frac{1}{2}(c_1\alpha)^2 \sin^2(\alpha x) = \frac{1-\nu^2}{Eh} N_{xx} \tag{3.22}$$

Integration of Eq. 3.22 between $-(b-\Lambda)$ and $b-\Lambda$ gives

$$w_m - w_0 = \frac{1-\cos(\alpha(b-\Lambda))}{\alpha}\sqrt{4\left[\frac{1-\nu^2}{Eh}N_{xx} + \frac{u_0}{b-\Lambda}\right]\cdot\left[1 - \frac{\sin(2\alpha(b-\Lambda))}{2\alpha(b-\Lambda)}\right]^{-1}} \tag{3.23}$$

3.2.2 Dugdale distribution for mode I and mode II

Instead of considering the clamped condition at the edge of the blister we replace the condition by an area where we impose a given traction distribution over a given length Λ : this is the cohesive (or process) zone of the crack tip, introduced in chapter 1. After Dugdale [20] (plastic yielding), cohesive zones were later used to describe damage processes [21] such as fracture processes that are interest for us, see [22, 23] and to model adhesive contact [24]. The general idea is that the rupture process is described by a local stress-displacement relationship shown in Fig. 3.7. The fracture energy, or interfacial toughness in our case, G_c is given by the area under the curve. Several stress distributions can be assumed to describe the local stress-displacement relationship. For example, solutions have been proposed by Williams et al. [25] for double cantilever beam (DCB) specimens. Whereas for the DCB the edge is solely loaded in mode I, in our case we have a mode mix at the edge of the blister. We will assume constant stress distribution (Dugdale) for both the mode I traction, T_n, and the mode II traction, T_t in the stress-displacement curve, see Fig.3.7. The energy in mode I, G_I simply writes as a function of the traction T_n and the crack opening displacement δ_n, and in mode II G_{II}, T_t and δ_t respectively,

$$\begin{aligned} G_I &= T_n\delta_n \\ \\ G_{II} &= T_t\delta_t \end{aligned} \tag{3.24}$$

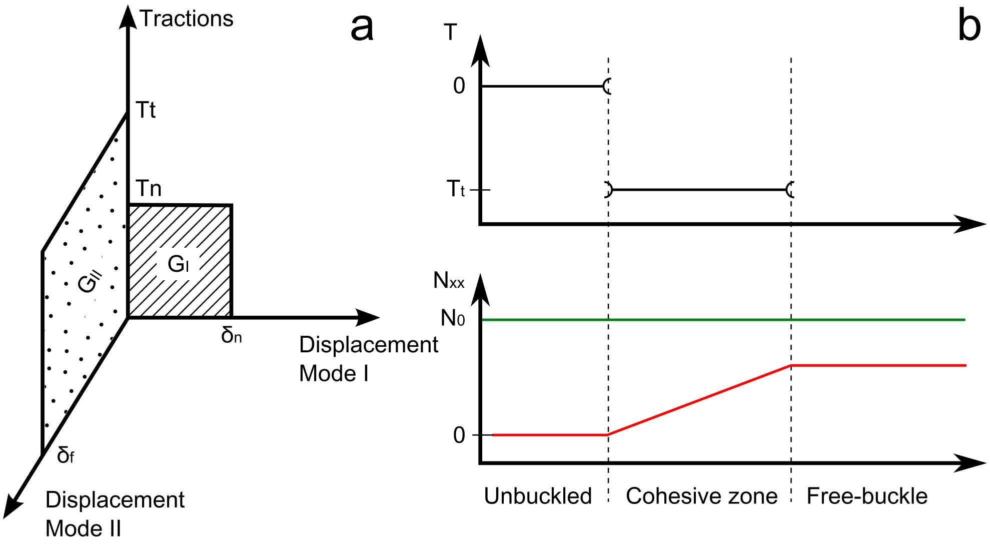
Tractions
a
Tt
Tn
GI
GII
δn
Displacement
Mode I
δf
Displacement
Mode II
T
b
0
Tt
Nxx
N0
0
Unbuckled
Cohesive zone
Free-buckle

Figure 3.7: **a**. Notations for Dugdale distribution in mode I and mode II resulting in (**b**) discontinuities of loading T and continuity of the plate stress.

Eq. 3.18 is simplified assuming small displacements in the process zone and the contribution due to mode I is added. Contribution from mode II is also added:

$$\begin{cases} \dfrac{\partial^4 w}{\partial x^4} = \dfrac{-T_n}{D} \\ \\ \dfrac{\partial N_{xx}}{\partial x} + T_t = 0 \end{cases} \tag{3.25}$$

Solution of the first relation of Eq. 3.25 is

$$w_{cz} = \frac{-T_n}{24D}x^4 + \frac{d_1}{6}x^3 + \frac{d_2}{2}x^2 + d_3 x + d_4 \tag{3.26}$$

Coefficients d_1, d_2, d_3 and d_4 can be determined from the continuity of displacements w_{cz} and its derivative in $x = -b$ and $x = -b + \Lambda$. Integration of the second relation of Eq. 3.25, gives

$$N_{xx}^{cz} = -T_t x + k_1 \tag{3.27}$$

k_1 being a constant. Hooke's law is still satisfied in the cohesive zone ($-b \leq x \leq -b + \Lambda$), with the assumption of small displacements and under plane strain :

$$\frac{\partial u}{\partial x} = \frac{1-\nu^2}{Eh} N_{xx}^{cz} \tag{3.28}$$

Integration gives k_1 :

$$k_1 = \frac{1}{\Lambda}\left[\frac{Eh}{1-\nu^2}u_0 + \frac{T_t\Lambda}{2}(\Lambda - 2b)\right] \tag{3.29}$$

where u_0 is the displacement along x at $x = -b + \Lambda$. There is a discontinuity for the loading T_t in $x = -b$, but the tension itself, N_{xx} is continuous at $x = -b$ and $x = -b + \Lambda$, see Fig.3.7. With conditions of continuity, we link the size of the cohesive zone with the residual stress in the blister.

$$N_{xx} = T_t\Lambda \tag{3.30}$$

$$u_0 = -\frac{T_t^0\Lambda^2}{2}\frac{1-\nu^2}{Eh} \tag{3.31}$$

3.3 Numerical resolution

In principle, this 2D model can be solved numerically but could not be extended to 3D. In order to solve 3D models, we have used finite elements coupled with cohesive elements to deal with the non linear plate deformation. In the following section we describe the implementation of the cohesive zone model using cohesive elements and the non-linear plate buckling using shell elements. The FEM calculations were carried out using the software ABAQUS [26].

3.3.1 Non-linear plate implementation

The plate can be modeled by any type of continuum solid elements. As in our case the thickness is small with respect to in-plane dimensions, we use shell elements. Discretization is done solely for the in-plane dimension, and gradient effects are neglected along the thickness direction. An elastic behavior is assumed with a Young modulus E and Poisson ratio ν.

The key point for implementation of buckling is to take into account the non-linear response of the plate, governed by Eq.3.1, by allowing large displacements.

Boundary conditions. Periodic conditions have been applied to the shell elements and cohesive elements for edges parallel to the y axis, the conditions are $v(x, y) = 0$ and no rotation along the x and z axis, ($\phi_x = 0$ and $\phi_z = 0$). Nodes part of the edges parallel to x axis for the plate and cohesive elements as well as the bottom nodes of the cohesive elements in contact with the rigid surface have fully built-in conditions.

Loading conditions. Loading is applied to the shell elements of the plate by a non-zero expansion coefficient, from which an eigenstrain $\epsilon_0 > 0$ is applied uniformly to the plate ($\epsilon_{xx} = \epsilon_{yy} = \epsilon_0$, $\epsilon_{xy} = 0$). An equibiaxial compressive stress state is generated in the film: $\sigma_{xx} = \sigma_{yy} = -E/(1-\nu)\epsilon_0 = -\sigma_0$, $\sigma_{xy} = 0$.

3.3.2 Cohesive zone implementation

Discontinuities of the tractions at both edges of the cohesive zone as with Dugdale, is difficult to handle numerically, see Fig. 3.7, so we use a continuous cohesive law.

Bilinear traction-separation law. We choose for the cohesive elements a bilinear-traction separation law. The general behavior of the traction components are described in Fig. 3.8. It represents the evolution of the tractions applied to a given cohesive elements. In a bilinear traction-separation law the behavior of the traction T_i during damage initiation and damage evolution is kept linear with respect to the separation δ_i, $i = n, t$ for mode I and II respectively. The total work of rupture is represented by the integral of T_i from 0 to δ_i^f which represents the displacement at full rupture. Note that δ_i^0 should be kept as small as possible, especially in comparison to δ_i^f. In this case the total work of rupture can be expressed as $G_{ci} = T_i^0 \delta_i^f / 2$. This bilinear behavior is defined for both mode I and mode II interfacial toughness through the normal traction T_n and the shear traction T_t.

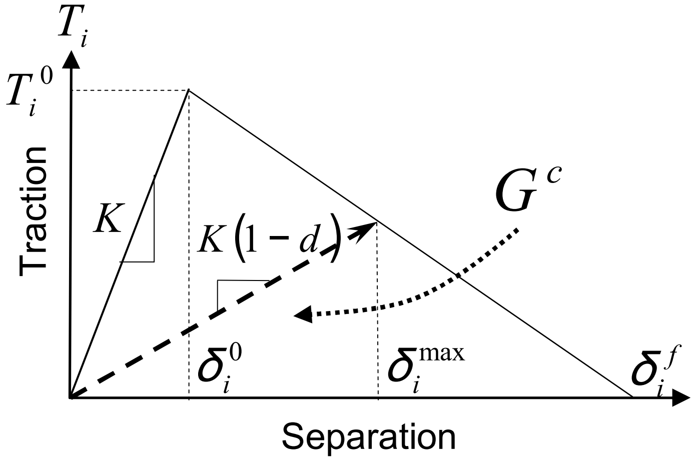

Figure 3.8: Traction vs separation law used for the toughness at the film/substrate interface. Mode I, II and mixed mode correspond respectively to $i = n, t$ and eff.

Damage initiation. When traction is applied to the cohesive element, the displacement remains proportional to the traction applied until a criterion is reached. We note $K_i = T_i^0/\delta_i^0$ the initial loading stiffness. It is defined for mode I and mode II. Values K_n and K_t must be large enough so that δ_n^0 and δ_t^0 are small enough. The damage initiation criterion we choose is a criterion based on a maximum normal, T_n^0 and shear T_t^0 tractions.

$$\left(\frac{T_n}{T_n^0}\right)^2 + \left(\frac{T_t}{T_t^0}\right)^2 = 1 \tag{3.32}$$

Determination of the mode mixity. Once the initiation criterion is reached, the mode mixity needs to be computed as the damage evolution will depend on this value. The definition of the mode mixity given in Eq.3.11 uses the stress intensity factor in mode I (K_I), and mode II (K_{II}), with respect to the crack tip. Such value is not directly available for cohesive elements. Therefore two possibilities can be used to evaluate the mode mixity. The first is to use the normal and shear components of the traction applied to the elements. Assuming the field around the crack tip is similar for the mode I and mode II then the ratio of stress intensity factors is identical to the ratio of the stress fields. The mode mixity definition used in the numerical simulation is thus :

$$\tan\psi = \frac{T_t}{T_n} \tag{3.33}$$

and corresponds to the relative proportion of mode II traction at the interface. An important condition is that the values of K_n,K_t, T_n^0 and T_t^0 must be carefully chosen so that when the criterion is reached, the distribution of tractions in mode I and mode II is physically acceptable. For example, if δ_t^0 is too large compared with δ_n^0, the criterion will be reached with a smaller T_t. The immediate consequence is that the mode mixity is smaller than expected and the damage evolution will not be properly conducted. One rule of thumb to avoid this problem is to take $\delta_t^0 \approx 2\delta_n^0$.

Another definition based on energies can be used for the mode mixity. The energy release rate G at the crack tip can be written as a function of K_I and K_{II}, from Eq. 3.16 and in case of an infinitively deep and hard substrate, $\alpha = -1$,

$$G = 2\bar{E}_f\,(1-\beta)\left(K_I^2 + K_{II}^2\right) \tag{3.34}$$

we then rewrite the energy release rate as a sum of contributions due to mode I and mode II. $G = G_I + G_{II}$ with $G_i = 2\bar{E}_f\,(1-\beta)\,K_i^2$, $i = I, II$. The mode mixity is therefore linked to ratio of the energy contribution from mode I and mode II by

$$\tan^2\psi = \frac{K_{II}^2}{K_I^2} = \frac{G_{II}}{G_I} \tag{3.35}$$

Numerically, a purely normal strain with respect to the crack plane will result in $G_I \neq 0$ and $G_{II} = 0$ independently of the stress applied in the cohesive element. The mode mixity computed from the traction will be higher in this case than the one computed from the energies. Convergence between the two methods is presented in appendix B.

Damage evolution. In order to implement irreversible decohesion, we allow for the cohesive traction T_i^0 to irreversibly decrease along the traction-separation curve as the maximum interfacial displacement δ_i^{max} increases from δ_i^0 to δ_i^f. This process reflects interface damage once the initiation criterion has been reached. After opening up to $\delta_i^{max} > \delta_i^0$, if the cohesive element subsequently closes, it unloads from δ_i^{max} to 0 with decreasing interface traction $T_i = K_i\,(1-d)\,\delta_i$, Fig. 3.8 dashed line. The damage variable d is chosen so that it increases from 0 to 1 with $\delta_i^{max} > \delta_i^0$ and fulfills the condition $T_i^0\delta_i^{max} = K_i\,(1-d)\,\delta_i^{max}$. This softening of the loading-unloading segment results in irreversibility through incomplete restitution of interfacial energy upon the unloading of the cohesive element. If δ_i^{max} reaches δ_i^f, then $d = 1$, $T_i^0\left(\delta_i^f\right) = 0$ and rupture is complete. The model applies for pure mode I and mode II.

Mode mixity dependence chosen. Once the criterion of initiation is reached, the mode mixity is evaluated. We consider that depending of the mixity of the loading, the energy release rate will be evaluated from Eq. 3.17 and the shape of G_c as a function of ψ has been previously plotted in Fig. 3.3. The energy release rate can be expressed as $G^c(\psi) = 1/2\ {T_n}^{0'}{\delta_n}^f + 1/2\ {T_t}^{0'}{\delta_t}^f$ as a function of the mechanical variables. For the damage variable d we define the effective cohesive stress ${T_{eff}}^{0'} = \sqrt{({T_n}^{0'})^2 + ({T_t}^{0'})^2}$, the effective interfacial deformation $\delta_{eff} = \sqrt{(\delta_n)^2 + (\delta_t)^2}$ and the effective deformation at full rupture ${\delta_{eff}}^f = 2G^c(\psi)/{T_{eff}}^{0'}$. The two expressions for $G^c(\psi)$ are compatible for ${\delta_n}^f/{\delta_t}^f = {T_n}^{0'}/{T_t}^{0'}$. The damage variable d is then defined as in the previous section, substituting the effective variable δ_{eff} for δ_n.

3.3.3 Unilateral contact

In order to take into account the presence of an infinitively deep and rigid substrate, the unilateral contact condition $w(x, y) \geq 0$ is introduced. Numerically, an interaction between a rigid planar reference surface and the bottom surface of the cohesive elements is created. The interaction is defined as frictionless. When both surfaces come into contact, any contact pressure can be transmitted between them, ensuring no interpenetration. If the contact pressure reduces to zero the surface are considered separated.

3.3.4 Resolution method

Two main methods may be used to numerically solve the problem, the so called implicit and explicit methods. We will briefly describe both methods and state what precautions need to be taken so that the solution may converge.

Implicit method. The implicit method uses a static stress analysis in which all inertia effects are neglected as well as time-dependent material effects (creep, swelling...). For a given stress state, an equilibrium solution is looked for until it matches some convergence criterion. This method is in general rather accurate and used when the response of the system to a loading sequence is needed. In the case of the straight sided blister problem, the crack front propagates on the sides when the stress increases until it reaches the right width $2b$. The variation of b can be rather large for two different levels of stress and thus the number of cohesive elements to break. Material models exhibiting a softening behavior, as the interface model used for the cohesive elements in this study, often result in serious convergence issues in FEM simulations. In an implicit formulation, the radius of convergence of the Newton-Raphson scheme reduces to zero at the point of instability. We avoid these issues by introducing viscous regularization of the damage variable with a characteristic time μ [26]. Viscous regularization causes the tangent stiffness matrix of the softening material to be positive for sufficiently small time increments. The amount of energy dissipated should remain small in comparison to the total elastic energy of the system ($< 1\%$).

Explicit method. The explicit method uses a dynamic stress analysis and does take into account the inertia effects. For non-linear problems in three dimensions involving contact and large deformation this method can be more efficient than static equilibrium. In addition this method is much faster but the convergence is less accurate. Here the damage of the cohesive elements must be controlled by the plate displacement. This can be ensured by choosing a mass density for the cohesive elements 85 times smaller than the mass density of the plate. In this configuration the velocity of the plate will not be limited by the velocity of the cohesive elements. Another issue comes from using dynamics to solve a quasi-static problem that would require millions of time increments to process in the natural period. In order to speed up the process in the simulation, the loading rate is increased, resulting in inertia effects, such as local unrealistic stretching or large vibration in the plate due to boundary conditions. Such effects can be limited by implementing a viscous pressure to the plate, which is very efficient to damp dynamic effects quickly.

A good check on the validity of the simulation is to obtain consistent results with these two methods.

3.4 Numerical results for a straight sided blister

In the following section we present numerical results obtained for the model coupling non-linear plate buckling and cohesive zone, in the particular case of a straight sided delamination. The geometry is briefly described and we present results on the influence of the loading conditions of the interface on the extent of delamination. Results are compared to the ideal case of an infinite cohesive stress $T_{max} = \infty$ that was presented in the first section and result in a zero process zone length, $\Lambda = 0$.

Finally we present the influence of the cohesive stress on the extent of delamination.

3.4.1 Geometry

The geometry we adopt is a rectangular plate of shell elements of length a and width $a/100$ and is presented in Fig 3.9. Each shell element is a square of edge size $a/100$ and thickness h and initial displacement $w(x, y) = 0$ along z axis. A defect zone is introduced to enable initial buckling. Its width is $2b_0$, from Eq. 3.7. The plate elements of this zone have an initial out of plane displacement $w(x, y)$ corresponding to a straight sided blister of width $2b_0$ and maximum normalized out-of-plane displacement $0.01h$.

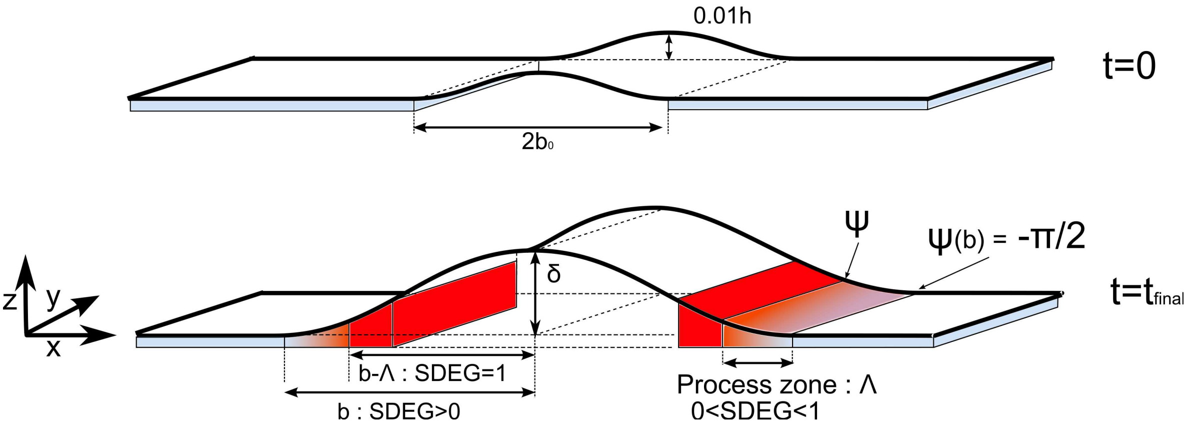

Figure 3.9: Geometry used to study the straight sided blister. Top numerical image of the resulting out of plane displacement, $w(x, y)$. Bottom, schematic of the straight sided blister for notations.

Under the plate, a layer of cohesive elements of zero initial thickness is placed, except in the zone of initial defect. The traction-separation law is as described in section 3.3.2. Cohesive elements are defined by their maximum normal and shear cohesive traction T^n_{max} and T^t_{max}, the mode I interfacial toughness G_{Ic} and η for the mode II strength.

3.4.2 Effect of the loading

For this given geometry, we load the plate with an eigenstrain leading to a residual compressive stress before buckling σ_0 ranging from 1.5 to 3 GPa. Thickness of the film varies from 50 to 250 nm. Cohesive stresses are fixed to $T^n_{max} = 170$ MPa and $T^t_{max} = 1.78$ GPa. Interfacial toughness is kept constant with $G_{Ic} = 0.4$ J.m^{-2} and $\eta = 0.8$. The system is studied at equilibrium when the delamination stops extending. In this condition we have $G = G_c$ and we can measure the half-width b, the maximum out-of-plane deflection δ of the buckle and the process zone size Λ.

Scheme of resolution. The resolution was carried with a definition of mode mixity based on traction with an explicit scheme. Comparison between the different schemes and definition of mode mixity are presented in appendix B. Both schemes of resolution converged to the same solution.

Euler solution. In Fig. 3.10 we plot δ/h measured as a function of σ_0/σ_c. Here b takes into account for the process zone size. We also plot the expected relation between δ/h and the loading ratio $\sigma_0/\sigma_c = (b/b_0)^2$ from Eq. 3.6 corresponding to the ideal case without a cohesive zone (no-CZ). This will serve as a reference for the straight sided blister.

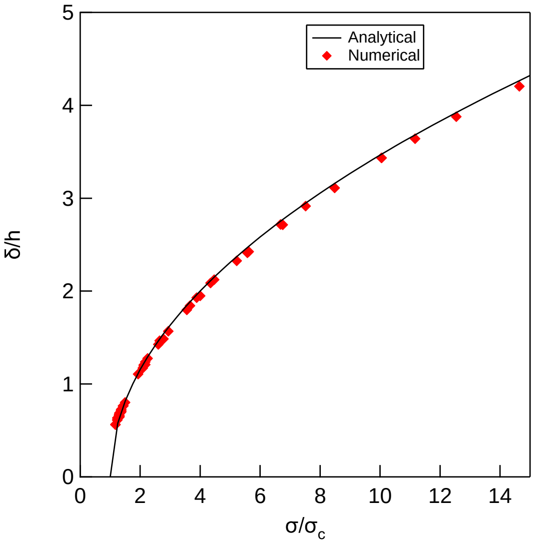

Figure 3.10: Out of plane displacement as a function of the loading ratio for numerical solution and analytical solution.

The agreement is a clear sign that the post-buckling regime of the plate adopts the Euler solution of the straight sided blister. Above the critical value of $\sigma_0 = \sigma_c$, attained at $b = b_0$, the plate experiences non-linear response for the out-of-plane displacement rather sharply. The minimal value for δ/h is equal to 0.56 which corresponds to $b/b_0 = \sqrt{\sigma_0/\sigma_c} = 1.08$. In the simulation, no blister may grow with a smaller b. As the minimum size for the initial defect to cause buckling is b_0 and that the process zone is about 10% of b, no stable blister may grow with a b smaller than $b = 1.1b_0$ for the interfacial toughness and cohesive zone parameters chosen. This effect can be reduced by decreasing the process zone size.

Stability at large loading ratios An important point must be considered from Eq. 3.24. When the mode mixity reaches pure mode II, the normalized out of plane displacement reaches the value of $\delta/h = 2.8$ in case of $\omega = 50°$ for the film here considered on a rigid substrate. However we do observe in our model higher values for δ/h for which blisters are stable. In order to understand in what conditions δ/h may exceed 2.8 when a finite cohesive zone is used, we plot (Fig.3.11) δ/h and σ/σ_c as a function of total elastic energy stored per unit area G_0 normalized by the interfacial toughness in mode I G_{Ic}.

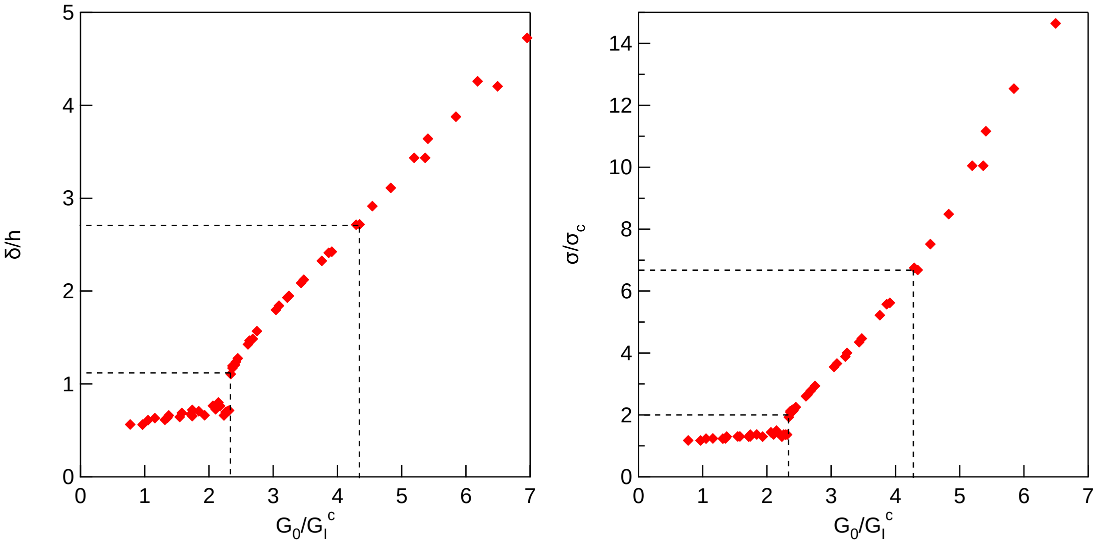

Figure 3.11: Measured out of plane displacement, left, and measured loading ratio, right, as a function of the normalized elastic energy to mode I interfacial toughness.

We first comment the evolution of δ/h. We observe that δ/h is a one to one function of G_0/G_{Ic} and three regimes can be identified. A first discontinuity of δ/h can be identified when $G_0/G_{Ic} = 2.34$. Below this value of G_0/G_{Ic}, δ/h remains small, between 0.5 and 0.8. Above $G_0/G_{Ic} = 2.34$, δ/h increases sharply and the expected maximum value for is reached for $G_0/G_{Ic} = 4.3$. Higher values of δ/h are reached at large G_0/G_{Ic}.

Commenting the evolution of σ_0/σ_c as a function of G_0/G_{Ic}, we also observe that the loading ratio follows a one to one relation with G_0/G_{Ic}. The loading ratio stays close to unity as long as $G_0/G_{Ic} < 2.34$. Above this value, the loading ratio evolves from 2 to 6.8 which is reached at $G_0/G_{Ic} = 4.3$ when $\delta/h = 2.8$. For higher values of energy, the loading ratio keeps on increasing up to 15.

This behavior of post-buckling solution below $G_0/G_{Ic} = 2.34$ can be interpreted as an effect of existence of the process zone and corresponds to loading conditions leading to $b < b_0 + \Lambda$. In these configurations the size of the process zone is constrained. For $2.34 < G_0/G_{Ic} < 4.8$, the solution follows the behavior of the solution with an infinite cohesive stress. For $G_0/G_{Ic} > 4.8$, stable blisters are still observed in a zone where the film should delaminate dynamically as $G \geq G_c(\psi = -\pi/2)$ in the infinite cohesive stress case. Stable blisters implies however a mode mixity smaller than $\pi/2$. In order to understand better, we now study the mode mixity in the simulations.

Mode mixity at the sides of the blister The mode mixity at the edge of the blister can be obtained by several means, either by computing ψ from the energy spent during damage $G = G_c(\psi)$ or from the tractions exerted at the interface $\tan\psi = T_t/T_n$. Calculations and distributions of mode mixity are presented in appendix B. The value of ψ plotted in Fig. 3.12 as a function of G_0/G_{Ic} is the mode mixity at the edge of the blister at $b - \Lambda$. Note that $\psi(b)$ is always equal to $-\pi/2$ in the post-buckling regime due to the plate compliance at the edge of the process zone, see Fig. 3.9 and appendix B. The value of the mode mixity obtained in the numerical simulation is compared to the value of ψ obtained from Eq. 3.15 using δ/h measured. Therefore we can expect the dependence of the mode mixity as a function of G_0/G_{Ic} in case of infinite cohesive traction.

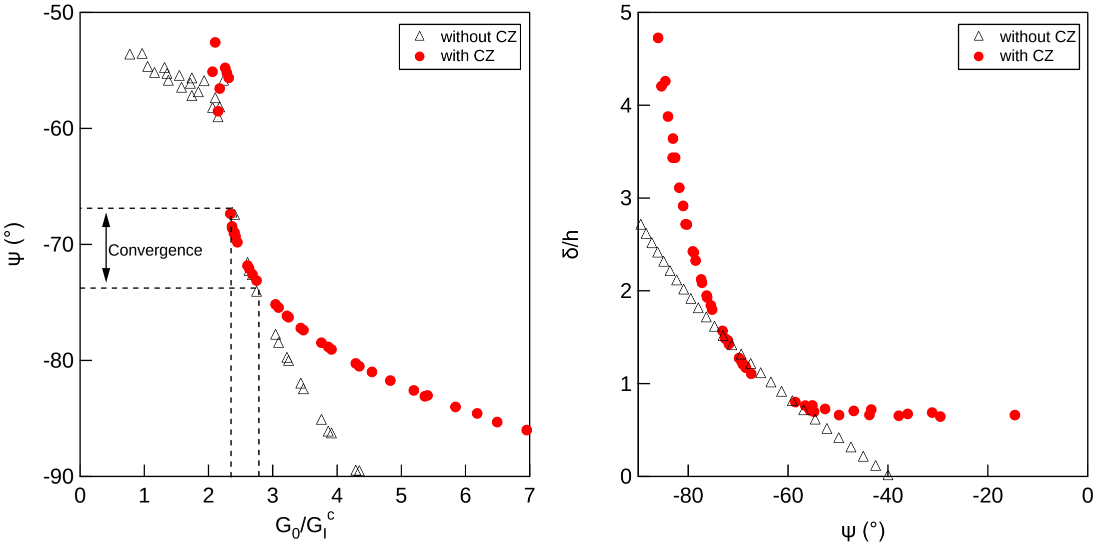

Figure 3.12: Mode mixity calculated from the normalized out-of-plane displacement for analytical solution and numerically computed from the tractions on the cohesive elements as a function of the normalized elastic energy to mode I interfacial toughness, left, and normalized out-of-plane displacement as a function of the mode mixity for analytical and numerical solutions.

We first comment the evolution of the mode mixity for the two models as a function of G_0/G_{Ic} on Fig.3.12. There is a small variation of the mode mixity below $G_0/G_{Ic} = 2.34$ as the blister cannot extend. We observe a good agreement from $-67°$ to $-75°$ for the case with and without existence of a process zone. However, the mode mixity is lower in the model with a cohesive zone than without for values above $G_0/G_{Ic} = 4.8$. As pure mode II is expected as early as $G_0/G_{Ic} = 4.8$ if the cohesive stress was infinite, $\psi = -86°$ is only reached for $G_0/G_{Ic} = 7$. Further calculation were not conducted but the trend predicts a pure mode II loading of the interface around $G_0/G_{Ic} = 11$.

Commenting now on Fig.3.12 the behavior of δ/h as a function of the mode mixity, the decreased values of the mode mixity under $\psi = -75°$ corresponds to a sharp increase of δ/h, way above the critical value of $\delta/h = 2.8$. Note that $\tan\psi$ is still a function of δ/h but different from the relation 3.15.

The reason for lower ψ can be numerous. Conditions of moment at the edge of the buckle are different due to the existence of the process zone and are likely to cause a lower ψ. In addition, another reason is the evaluation of the tractions at the interface. Better convergence may be achieved for finer mesh, at cost of higher computation time.

We have seen that taking a non-infinite cohesive stress leads to existence of the process zone at the edge of the buckle in the model chosen. This process zone leads to two main changes in the straight sided blister solution. First, at low loading, the minimum width for the post buckling regime is now $b_0 + \Lambda$, and smaller blisters cannot be obtained. Secondly, at large loading, it is possible to observe stable blisters with loading ratios larger than $\sigma_0/\sigma_c = 6.8$ due to lower mode mixity at $b - \Lambda$ at the edge of the blister.

3.4.3 Effect of process zone

We will now study the effect of the size of the process in terms of morphology for the straight sided blister. Numerically, the size of the process zone may be varied easily by changing the values of the maximum tractions in the bilinear traction-separation law. We apply a factor to the maximum traction in normal and shear and see the evolution of the size of several key parameters of the straight sided blister.

We first plot in Fig. 3.13 the process zone size and the half width of the free buckle part of the resultant blister. For comparison purpose, the expected value in case of no-CZ is also shown. The first comment is that for large values of the maximum shear traction, the process zone size decreases towards zero, while b approaches the expected b for the no-CZ case. Note that numerically, evaluation of the traction is limited by the mesh size and further convergence towards the no-CZ case would require finer meshing. As a result for the largest maximum shear traction the plate does not experience buckling (not shown). We observe that the process zone size increases when the maximum shear traction is decreased. Opposite behavior is observed for the width of the free buckle part, with an amplitude of variation much smaller.

We now comment the evolution of δ/h also plotted in Fig. 3.13. The normalized out-of-plane displacement decreases with decreasing size of the process zone and approaches the no-CZ case for a rather large range of maximum shear traction. This remarkable fact is due to the total width of the blister, therefore including the

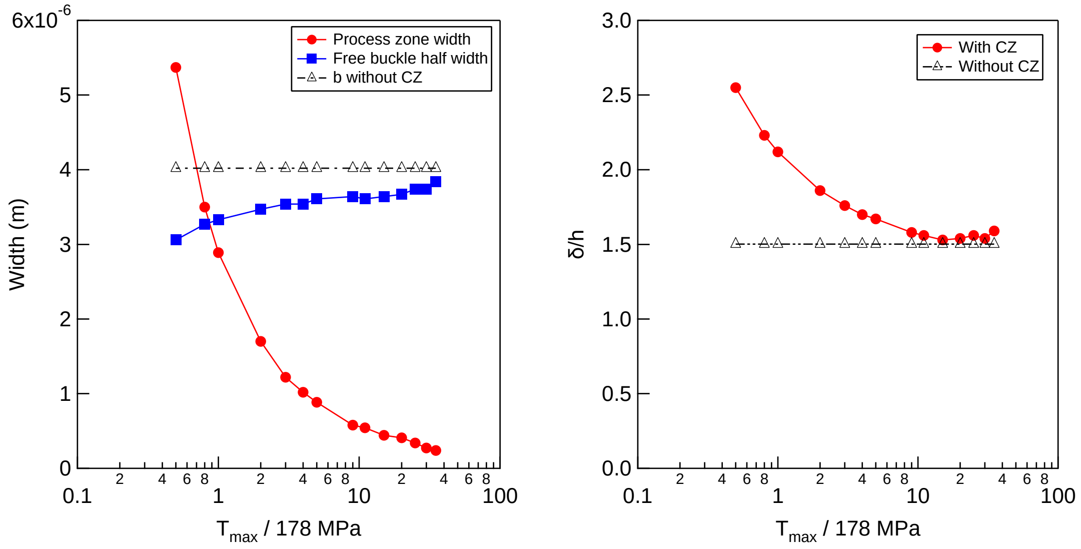

Figure 3.13: Process zone size and half width of the free buckle part for a straight sided blister with cohesive zone as a function of maximum shear traction and half width of expected straight sided blister in case of no cohesive zone (left). Normalized out-of-plane displacement as a function of the maximum shear traction and expected value for no cohesive zone (right).

process zone, remaining close to the expected b for the no-CZ case. This convergence range corresponds to blisters where Λ is not higher than 15% of b. For large value of the process zone size, δ/h might be 60 % higher than expected.

It is interesting to compare the family of blisters obtained for the same loading conditions and different process zone sizes to the Euler solution. One way is to plot δ/h as a function of b/b_0 and to compare the solution to Eq. 3.6. These quantities are plotted in Fig. 3.14. On the top left part of the graph we plot b including the process zone width over which the energy is relaxed. In this case, the height of the blister is smaller than expected by the Euler solution and tends to be further off as the process zone sizes increases and approaches the no-CZ case at small values of Λ. This is expected as the stress in the film above the process zone is less relaxed than in the free-buckled part. The buckle is effectively restrained by the cohesive stress. From a practical point of view, it is difficult to identify precisely b. Indeed, displacements remain small over the cohesive zone and profile of the blister would give $b-\Lambda$ rather than b. We therefore plot in Fig. 3.14 δ/h as a function of $(b-\Lambda)/b_0$. In this case, the solution result in a δ/h way above the one expected from the Euler solution. This is due to the fact that the cohesive zone offers more compliant boundary conditions than the built in assumption of the no-CZ buckle.

In terms of loading ratio, plotted in Fig. 3.15, if σ_c represents the stress left in the free buckle part, σ/σ_c increases with the size of the process zone, and approaches

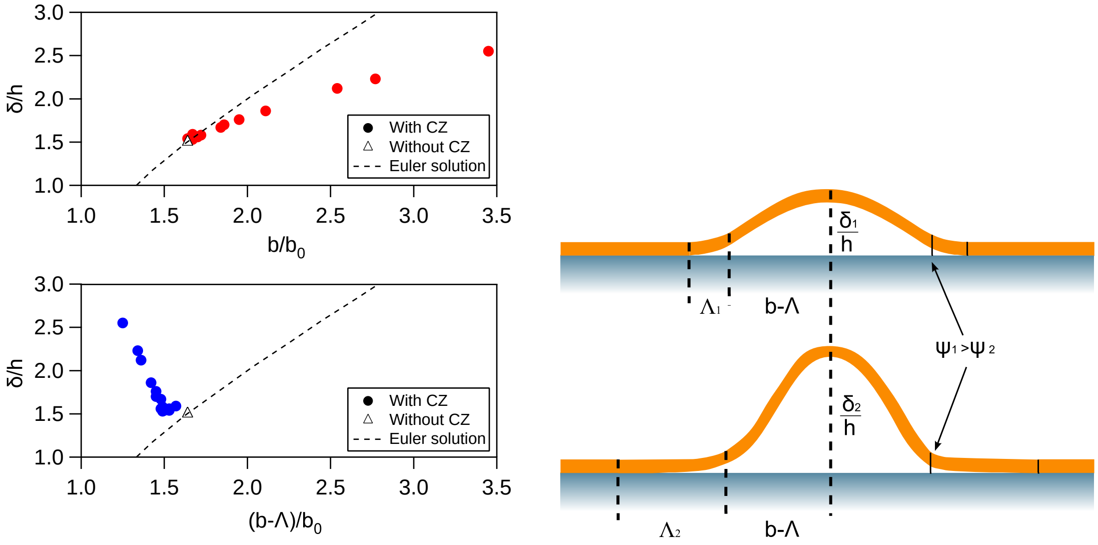

Figure 3.14: Out of plane displacement as a function of the loading ratio for numerical solution and analytical solution (left). Schematic of the effect of the process zone on a straight sided blister (right).

the expected value of σ/σ_c for small process zone size. This reflects the fact that initial stress in the free part is more and more relaxed. As the total b increases as well, the equivalent σ_c for a straight sided blister without a cohesive zone drops as well. The actual energy release rate G, plotted in Fig. 3.15 drops with increasing

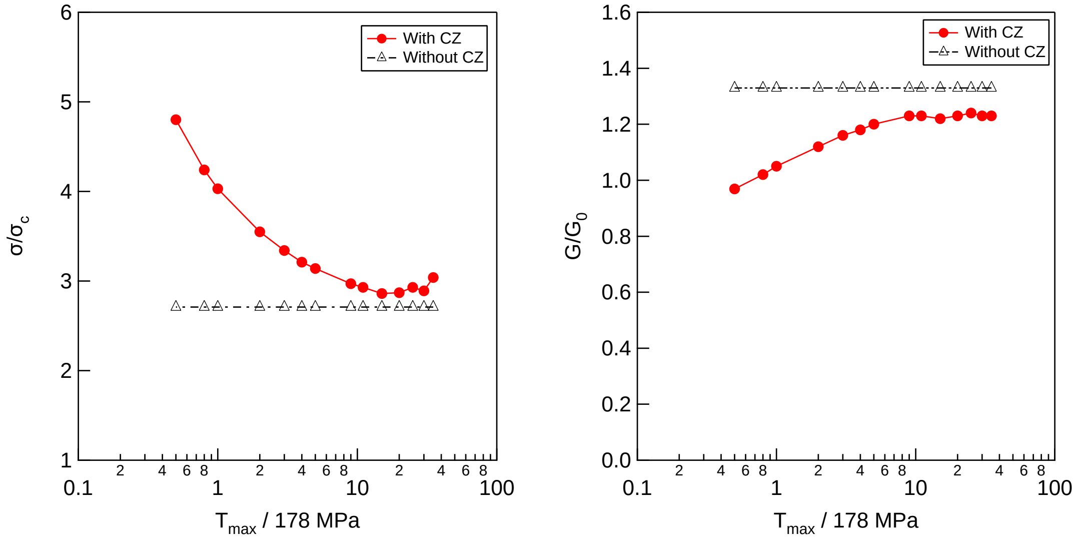

Figure 3.15: Loading ratio for a straight sided blister with cohesive zone as a function of maximum shear traction and expected loading ratio of a straight sided blister in case of no cohesive zone (left). Normalized enery release rate as a function of the maximum shear traction and expected value for no cohesive zone (right).

size of the process zone. The mode mixity at the edge of the blister is smaller for the cases with a large process zone, even if the initial loading of the interface G_0/G_{Ic} is constant. This is equivalent to a decrease of the mode mixity at $x = b - \Lambda$, and a constant shear loading at $x = b$.

The consequence of a large process zone is summarized Fig. 3.14 on the right. For this kind of blister, the delaminated part remains an Euler shape with an apparent aspect ratio $\delta / (b - \Lambda)$ much higher than in a regular blister. At the sides of the blister, the mode mixity is lower and the residual stress in the blister is smaller than for a blister without a cohesive zone of half width $b - \Lambda$.

We add that though the effect of the process zone size was studied by changing the values of maximum tractions, the size of the process zone is also linked to the value of the interfacial toughness at constant traction. Therefore if the tractions are not adapted in the model, one should expect such effects at very large interfacial toughness values.

3.5 Conclusion

In this chapter we presented the model coupling a non-linear plate with a cohesive zone used to solve the buckling driven delamination problem. This model was treated analytically for Dugdale stress distributions for mode I and II and numerically using bilinear stress distributions. The results show a good convergence of the model towards the solution without a cohesive zone using proper parameters. In particular the values of the T_{max} should be kept as high as possible. The model predicts larger out-of-plane displacements of the blister and lower energy release rate at the sides in case of process zone at the interface above 15% of b.

With this we investigate the influence of the interfacial toughness on the morphology of buckling driven delamination. In the next chapter we study the morphology of the delamination pattern, as a function of the interfacial parameters, and in particular try to link specific dimensions of the pattern to the interfacial toughness.

Bibliography

[1] J. W. Hutchinson and Z. Suo. *Adv. Appl. Mech.*, 29:63, 1992.

[2] H. M. Jensen. Energy release rates and stability of straight-sided, thin-film delaminations. *Acta metall. mater.*, 41:601–607, 1993.

[3] Z. Suo and J. W. Hutchinson. *Int. Journal of Fracture*, 43:1–18, 1990.

[4] J.-S. Wang and Z. Suo. Experimental determination of interfacial toughness curves using brazil nut sandwiches. *Acta metall. mater.*, 38(7):1479–1290, 1990.

[5] Y. Wei and J. W. Hutchinson. *Philosophical Magazine*, 88:3841–3859, 2008.

[6] R. Kitey, P. H. Geubelle, and N. R. Sottos. *J. Mech. Phys. Solids*, 57:51–66, 2009.

[7] J. Tong, K. Y. Wong, and C. Lupton. Determination of interfacial fracture toughness of bone-cement interface using sandwich brazilian disks. *Eng. Frac. Mech.*, 74:1904–1916, 2007.

[8] K. M. Liechti and Y. S. Chai. *Journal of Applied Mechanics*, 59:295–304, 1992.

[9] A. G. Evans and J. W. Hutchinson. *Acta metall.*, 37(3):909–916, 1989.

[10] V. Tvergaard and J. W. Hutchinson. *J. Mech. Phys. Solids*, 41(6):1119–1135, 1993.

[11] R. Tadepalli, K. T. Turner, and C. V. Thompson. *J. Mech. Phys. Solids*, 56:707–718, 2008.

[12] J. W. Hutchinson. *Acta metall. mater.*, 40(2):295–308, 1992.

[13] M.-W. Moon, K.-R. Lee, K. H. Oh, and J. W. Hutchinson. *Acta Mater.*, 52:3151, 2004.

[14] B. Audoly. *Phys. Rev. Lett.*, 83:4127, 1999.

[15] G. Parry, A. Cimetiere, C. Coupeau, J. Colin, and J. Grilhe. Stability diagram of unilateral buckling patterns of strip-delaminated films. *Phys Rev E Stat Nonlin Soft Matter Phys*, 74(6 Pt 2):066601, 2006.

[16] H. Mei, C. M. Landis, and R. Huang. *Mech. Mater.*, 43:627–642, 2011.

[17] X. L. Fan, R. Xu, and T. J. Wang. *App. Surf. Science*, 258:9816–9823, 2012.

[18] O. van der Sluis, A. A. Abdallah, P. C. P. Bouten, P. H. M. Timmermans, J. M. J. den Toonder, and G. de With. *Eng. Fracture Mech.*, 78:877–889, 2011.

[19] F. Toth, F. G. Rammerstorfer, M. J. Cordill, and F. D. Fischer. *Acta Mater.*, xxx:xxx–xxx, 2013.

[20] D.S. Dugdale. Yielding of steel sheets containing slits. *J. Mech. Phys. Solids*, 8:100–104, 1960.

[21] M. A. Crisfield and J. Willis. *Comp Method in App. Mech. Eng.*, 66:267–289, 1988.

[22] X. P. Xu and A. Needleman. *Model. Simul. Mater. Sci. Eng.*, 1:111, 1993.

[23] V. Tvergaard and J. W. Hutchinson. *J. Mech. Phys. Solids*, 40:1377–1397, 1992.

[24] E. Barthel. *J. of Colloid and Interface Sci.*, 200:7–18, 1998.

[25] J. G. Williams and H. Hadavinia. *J. Mech. Phys. Solids*, 50:809–925, 2002.

[26] Dassault Systèmes Simulia Corp., Providence, RI, USA. *ABAQUS Manuals Collection*, 2010.

Chapter 4

Buckles morphology: experiments meet simulations

This chapter is dedicated to the understanding of the morphology of the delamination for films under in-plane equi-biaxial compression.

In particular the origin of the oscillating morphology of the telephone cord blister remains open. Some experiments [1] report that the telephone cord morphology might result from the destabilization of a straight sided blister grown previously. Such phenomenon is known as "‘secondary buckling"’. Here we use the model (chapter 3) to understand morphologies obtained with low adhesion and stressed layers (chapter 2). In particular, we will pay attention to the domain over which the stress is relaxed, which is of great importance in order to compare experimental data with analytical models.

4.1 Experiments and propagation mechanism

As shown in chapter 3, compressive stress is the driving force for formation of buckles. Stress is released during buckling of the film concomitantly with propagation of the crack front. Several ways can be used to force a film to form buckles and they often mean different ways to introduce compressive stress. We have stated in chapter 2 the main causes of compressive stress and most of them have been used to study buckling driven delamination.

The first way to produce blisters is to directly put the film under a compressive strain. This is especially doable for hard films on soft substrates under traction. In this case a uni-axial traction along x will result in a compressive strain of the substrate along y due to the Poisson effect [2]. Depending on the elastic mismatch between the film and the substrate and the value of the interfacial toughness it will either result in wrinkling [3, 4, 5] or buckling driven delamination [2]. This effect is more difficult to achieve on hard substrates and has the disadvantage that it is anisotropic.

A second source of compression is thermal stress. It was used in to study propagation of a straight blister along a strip [6]. The difference in thermal expansion coefficients between the film and the substrate gives rise to a compressive stress when the stack is annealed. Advantage of thermal stress is a good isotropy of the in-plane stress, provided that the material is isotropic. However if the difference in thermal expansion coefficients between film and substrate is not large, it requires a high annealing temperature. Numerous metal/oxide interfaces are sensitive to oxygen diffusion at the interface. In addition, films growing in VW mode such as silver dewet at rather low temperatures [7]. Such changes may cause variation of the interfacial toughness during an annealing step.

The third way to introduce compressive stresses (as described in chapter 2) relies on the conditions of deposition to achieve an isotropic in-plane residual intrinsic stress. Such a compressive layer, or superlayer, may be deposited at room temperature on top of a multilayer stack where a weak interface resides and cause rupture by buckling driven delamination. In the next section, we describe in detail the experimental conditions used to study delamination of thin films and probe interfacial toughness by the superlayer method.

4.1.1 Design of the experimental system

In order to study buckling driven delamination, we use the system described in Fig. 4.1, in which a superlayer provides elastic energy to the weak interface.

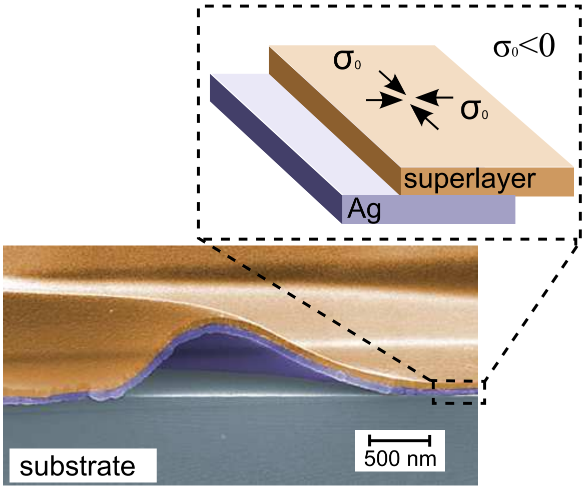

Figure 4.1: Scanning electron micrograph in cross-section of a buckled thin film. The stack consists of 80 nm of molybdenum and an especially thick 80 nm of silver, for figurative purpose, on a silicon wafer.

Interface. In our experiments, we use a silicon wafer of 2 inches in diameter as a substrate. Native oxide [8] on the polished surface is not removed prior to deposition and is simply cleaned of dust and will therefore be referred to as $\mathrm{SiO_x}$. In a second step, a continuous layer of 15 nm of silver is deposited by magnetron sputtering. The interface formed by silver and the silicon oxide is expected to be the weakest of the stack where the interface crack will propagate during delamination. In order to ensure constant interfacial toughness in mode I, a pure molybdenum layer of 50 nm is always sputtered right after silver to prevent Ag oxidation from the plasma when $\mathrm{MoO_x}$ is sputtered.

Stressed superlayer. Next, a stressed layer of molybdenum doped with oxygen is sputtered. Following the results obtained for the straight sided blister in chapter 3, loading of the interface is controlled by the total elastic energy normalized to the mode I interfacial toughness $G_0/G_{Ic} \propto (h\sigma^2)/G_{Ic}$[1] and by film thickness. This is why it is necessary to control both σ and h over as large a range as possible. For the molybdenum superlayer, the thickness is controlled by deposition time and residual stress can be tuned by changing the deposition conditions presented in chapter 2[2].

In Mo films, the residual stress ranges from 500 MPa to 4 GPa in compression and thickness varies from 50 nm to 1 μm. Such conditions lead to elastic energies ranging from 0.05 $\mathrm{J.m^{-2}}$ to almost 10 $\mathrm{J.m^{-2}}$. In some cases, loading is enough to break the interface and cause buckling driven delamination of the $\mathrm{SiO_x}$//Ag interface.

4.1.2 Experimental investigation of the morphology of the blister

When the $\mathrm{SiO_x}$//Ag interface is loaded with different G_0, buckling driven delamination results in a rather large variety of patterns that may be classified and are presented in Fig. 4.2.

The first morphology encountered at low loading is of course the no-delamination case. If the energy is increased, telephone cord like blisters appear. They are very regular and can be characterized by their period λ and their full width $2b$, by analogy with a straight sided blister. Note that all TC blisters are far from being identical and they display a wide range of aspect ratios $0.8 < \lambda/2b < 1.6$ for different deposition conditions. In some cases the blister becomes angular with a herringbone structure (Fig. 4.2).

---

[1] Stress measurement performed on silver and molybdenum thin films shows that $\sigma_{Mo} \approx 100\sigma_{Ag}$. In addition thickness of the silver layer is small in comparison of the superlayer, $h_{Mo} > h_{Ag}$ unless told. Therefore we will neglect the influence of the silver layer in the contribution of loading.

[2] In further consideration we assume that the stress distribution through the thickness of Mo does not impact the general shape of the blisters. We will assume that the average stress of the stack can be extended to the film through the thickness and therefore :

$$\sigma_0 =< \sigma > \tag{4.1}$$

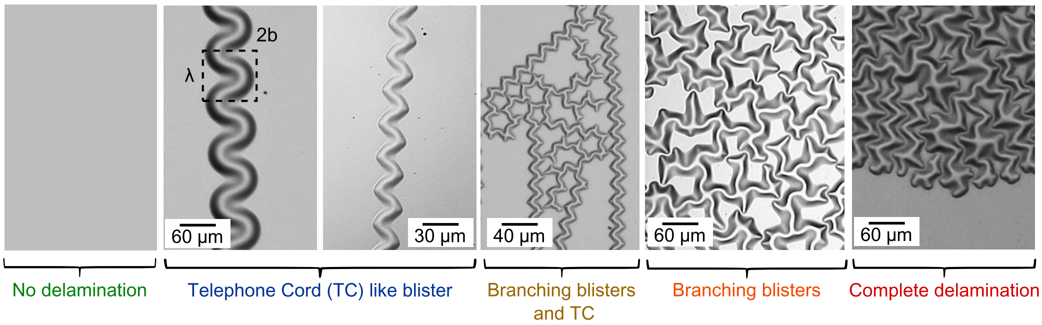

Figure 4.2: Microscope photographs of the morphologies commonly observed for the delamination of silver-silica interface loaded by a equibiaxial compressive molybdenum layer. Patterns are ranked by complexity from no-delamination, left, to complete delamination, right.

If the elastic energy of the superlayer is further increased, the front of the blister can eventually destabilize into a branching structure which remains rather periodic. This destabilization of the front seems like a continuous change of the morphology and can be concomitant with the growth of a TC blister.

Increasing the elastic energy given to the system results in heavy branching where the notion of periodicity tends to disappear until complete delamination is reached. Note that when complete delamination is achieved, a characteristic length scale is observed due to the relaxation of a film under equi-biaxial loading, see last morphology in Fig.4.2.

From these observations, two questions can be addressed. What causes the periodicity of the TC blister ? What causes branching of the blister ?

4.1.3 Comparison with simulations

Branching and periodicity of the blister cannot be explained without understanding growth of the crack front. Propagation of the buckling driven delamination can be followed experimentally using optical microscopy. Propagation of a TC blister is shown in Fig. 4.3 (bottom). It corresponds to the rupture of a $SiO_x//Ag$ interface for 10 nm layer of Ag loaded by 120 nm of MoO_x, compressive stress $\sigma_0 = 1.72\,\text{GPa}$. The film spontaneously delaminated when brought to atmospheric pressure, forming a 29 μm wide TC progressing over one wavelength in about 28 s. The buckle propagation was consistent with usual observations [9], with one notable addition however: it was observed that the tip of the semi-circular buckle sags when the TC completes one half-rotation and the front caves in (Fig. 4.3). This sagged area is reminiscent of the configurational instabilities predicted earlier [10].

In order to further understand the process, we use the model proposed in chapter 3 to solve the buckling driven delamination. Numerical resolution is the same as the one described for the straight sided blister problem except that the simulation box

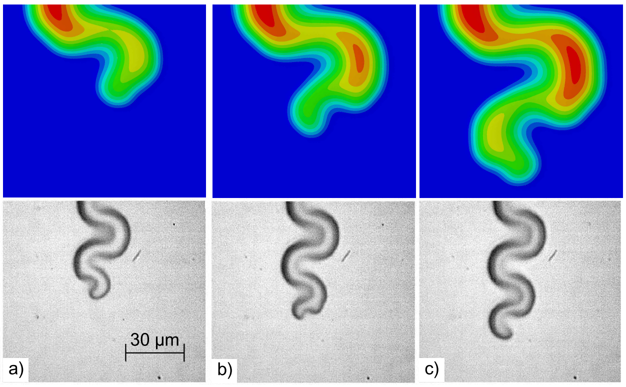

Figure 4.3: Telephone cord propagation : comparison between numerical results (top) and optical measurements (bottom). Configurational instability induces a sag at the front, resulting in pinning of the outer edge of the buckle in almost pure shear. The blister grows further around this pinning point thus changing direction of rotation.

is much larger allowing for the propagation from an initial defect into a landscape of constant loading G_0 and interfacial toughness G_c. The final result of the numerical simulation is a post-buckling equilibrium with a telephone cord like pattern. This blister is shown in Fig. 4.4 where the adhesion-free area, i.e. without cohesive elements, of the initial defect is marked by dashed lines. In the adhesion-free initiation area, a standard TC buckle initiates readily [11, 12]. The buckle subsequently propagates to the area where the film adheres to the substrate. The morphology of the TC there differs markedly from the morphology in the adhesion-free area as it is dictated not only by the film thickness and the elastic properties of the film, but also by the fracture energy $G_c(\psi)$. The simulation emulates the experiment very well (Fig. 4.3). In Fig. 4.3-a the buckle grows as a counter-clockwise segment

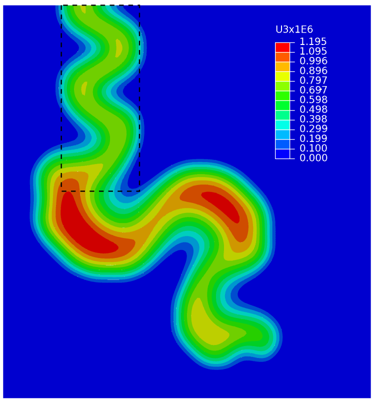

Figure 4.4: Overview of the deformed shape of the delaminated film in the numerical simulation. We can distinguish the adhesion free initiation zone (dashed line). Note the strong contrast between the buckle morphology in the adhesionless area and the morphology of the buckle propagating in the adhesive area.

of pinned circular blister [13] with increasing radius. Subsequently (Fig. 4.3-b) the initial convex front becomes unstable and a sag appears on the outer edge of the buckle, slightly behind the front, and gives rise to a bifurcation of the propagating front into two branches. While the right-hand branch gradually comes to a halt, the left-hand branch moves forward (Fig. 4.3-c), turning around a specific point located near the sagged area and growing clockwise as another segment of pinned circular blister with growing radius.

4.1.4 Branching blisters

In Fig. 4.5 an experimental blister is presented in which the crack front separates into two branches. Here we rupture a $SiO_x//Ag$ interface with 15 nm of Ag loaded by 132 nm of MoO_x ($\sigma_0 = 1.84$ GPa). The film spontaneously delaminated when brought to atmospheric pressure forming a periodic structure with $\lambda = 21.4\ \mu$m. The sagged area previously observed for growth of a TC was also present. However, the front of the TC blister was more angular resulting in a herringbone structure.

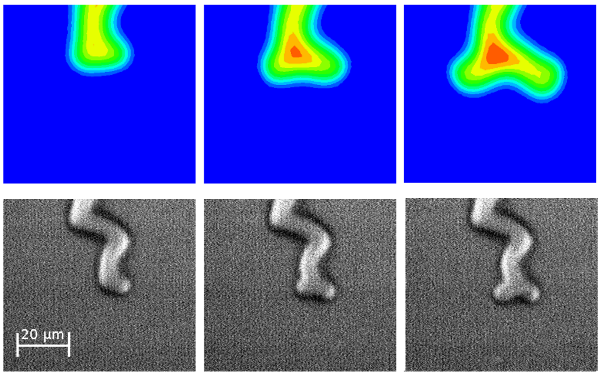

Figure 4.5: Formation of branching blister : comparison between numerical results (top) and optical measurements (bottom). Configurational instability induces a sag at the front, resulting in pinning of the outer edge of the buckle in almost pure shear. The crack front divides in two part around the pinning point.

Again, numerical simulation of the branching blister can be obtained. From the TC configuration we need to either decrease G_{Ic}, h or increase σ_0. Such observations are in agreement with experimental observations for $SiO_x//Ag$ interface for which branching blisters are observed for large G_0 or when the residual compressive stress is large $\sigma_0 > 2.5$ GPa for very thin films $h < 100$ nm.

Unlike TC case, here no front comes to a halt and both branches move forward (Fig. 4.5), being separated by a point near the sagged area. Radii of both fronts are very similar and do not enlarge as both branches propagate with an angle of approximately 120°. The out-of-plane displacement at the junction of the three branches, including the delaminated part which subsequently separated, is larger than in other parts of the delaminated pattern.

4.1.5 Pinning of the crack front : sagging and mode mixity

We have seen that for both TC and branching blisters, an instability develops along the crack front causing the film to destabilize and sag. A detailed series of snapshots of the TC buckle propagation around the turning point is shown in Fig. 4.6. where the mode mixity angle ψ is reported around the delamination front at different stages. When the initial portion of pinned circular blister collapses, forming the sag due to configurational instability [10], it can be observed that shear increases markedly at the interface since ψ rises from its mean value 72° to almost 90° (*i.e.* near mode II), and such observation can be made as well for the branching blister. It clearly demonstrates that the coupling between instability and mode mixity dependent adhesion results in the formation of a *pinning point*, as it is effectively impossible to break the interface in mode II. The solution of expanding around the pinning point becomes energetically more favorable for the buckle, and the delamination front then divides into two branches, expanding on each side of the pinning point. Growth of both or halt of one of the crack fronts leading to branching or TC buckle depends on the position of the pinning point. For the TC buckle, on the right-hand side of the pinning point, the previous blister keeps growing, increasing its radius into full half-circle but stops gradually. It shifts the pinning point slightly in the process, shifting also present for the branching blisters. On the left-hand side, the other front grows as a new segment of pinned circular blister. This smaller blister grows faster than the previous one and it is this counter-rotating pinned circular blister which emerges as a new TC segment. From this point, the story repeats itself. If the loading is large enough, both ends can grow. This is the branching case.

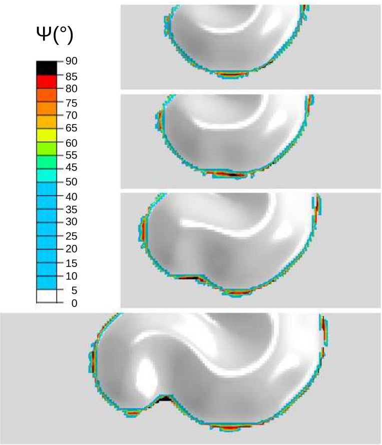

Figure 4.6: Phase angle along the delamination front for four different stages of propagation. A pinning instability can be observed, appearing when the front enlarges and the drift of the pinning point during propagation.

Summerizing the detailed experimental observation of the crack front during propagation of both TC and branching buckles and supported by numerical simulation, it can be stated that the origin of the periodicity of the blister arises from the instability of the crack front. This instability leads to sagging of the plate causing a decrease of the mode I component at the crack front increasing the local mode mixity to almost pure shear. Because of the mixed-mode dependence of the interfacial toughness, the energy release rate cannot reach the value of interfacial toughness in pure shear and the crack front is pinned. As this process repeats itself regularly, the result is a periodic pattern where λ is defined as the equilibrium distance between two pinning points.

4.2 Simulations: Phase diagram of buckling driven delamination patterns

We have experimentally identified four different morphologies for the buckling driven delamination, see Fig. 4.2, including the possibility to have branching buckle concomitantly with TC buckle. It is known that interfacial defects are important in many buckling problems [14, 15, 16] and especially in buckling driven delamination [17]. They are in general the initiation point for propagation of the four types of buckling driven delamination pattern over a large surface, as long as the condition $G \geq G_c$ is verified. We are here interested in answering two questions : What parameters govern the propagation of the buckling driven delamination from an initial defect ? What drives the transition from one morphology to the other ?

In order to unveil the governing parameters for the transition between morphologies, we use numerical simulation that allows to change interfacial toughness and film properties easily.

4.2.1 Phase diagram

We use the numerical resolution of the model for buckling driven delamination based on cohesive zone modeling to simulate a large number of buckles. Parameters varied are summarized in Tab. 4.1 and are representative of the experiments conducted in the previous section. Poisson ratio $\nu = 0.31$ and mode II dependence of the interfacial toughness $\eta = 0.95$ were fixed. The cohesive stresses in mode I and mode II were also kept constant with $T^n_{max} = 17\,\text{MPa}$ and $T^t_{max} = 200\,\text{MPa}$.[3] As a result, the variation of the crack opening displacement is rather large. We observed that the ratio between the process zone and the size of the blister Λ/b remained under 15%, which is the limit determined in chapter 3 for good convergence of the model.

---

[3] Note that the values of the cohesive stress are smaller than the one chosen in chapter 3 for the straight sided blister. This choice was imposed by the larger in-plane element size used in this study.

Parameter	σ_0 (GPa)	h (nm)	E (GPa)	G_{Ic} (J.m^{-2})
Range	0.6 - 4	50 - 10000	50 - 400	0.1 - 30

Table 4.1: Parameters used in the numerical determination of a phase diagram of buckling driven delamination.

Buckling is initiated in the defect of half width slightly greater than b_0 and propagates to the adhesive zone depending of the loading conditions. A plot of the delamination morphologies is presented in Fig. 4.7 where the no-delamination case represents an initial defect that did not result in a propagating buckling driven delamination. Each morphology corresponds to the experimental cases observed previously (see Fig. 4.2)

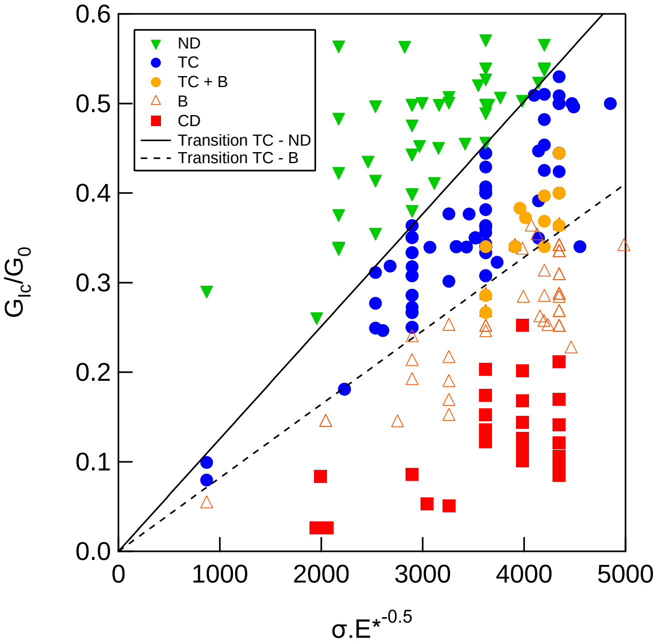

Figure 4.7: Phase diagram of the delamination morphology with $\eta = 0.95$ and $\nu = 0.31$. The morphology of delamination is indicated and the calculated limit for propagation of the an initial defect and branching of a delamination front are ploted. ND : No delamination, TC : Telephone cord, B : Branching, CD : Complete delamination.

We observe that for the set of parameters chosen, $\left(G_{Ic}/G_0; \sigma_0/\sqrt{E}\right)$, it is possible to separate several regions of existence for each morphologies. As expected, the crack front does not propagate from the initial defect at large G_{Ic}/G_0 as the energy in the system is not large enough to induce rupture of the interface. At lower interfacial toughness, on the onset of delamination, the first morphology encountered is invariably the TC like blister followed by branching blister and complete delamination when interfacial toughness drops toward zero.

It is noticeable that whereas for a straight sided buckle, for which each buckle is fully characterized with a given loading ratio σ_0/σ_c, equivalent to a given G_0/G_{Ic}, another parameter is required to characterize fully the delamination pattern when secondary buckling occurs. Indeed if G_0/G_{Ic} is kept constant it is possible to induce a change in the morphology by increasing h/G_0.

4.2.2 Condition for propagation of the buckling driven delamination.

The previous paragraph has shown a clear separation between the domains within which the film does not delaminate outside the initial defect and the domain of TC buckling. We would like to express the boundary for propagation of the buckling driven delamination from an initial defect as a critical propagation stress that we name σ_c^* at each G_{Ic}/G_0. The boundary is shown on Fig. 4.7. It differs from the classical critical buckling stress σ_c of a plate of width $2b$. Indeed as the classical critical buckling stress depends on the plate width, here σ_c^* does not directly depend on an initial length but on adhesion, loading and film properties.

It should be here stated that the initial defect size bears an important role. In order to determine σ_c^*, we assume that the initial defect is small in comparison with the resulting buckle size after propagation. If the initial defect is larger than the resulting blister, the mode mixity the crack front experiences will exceed the value above which G_c is larger than G_0 and the crack front will not propagate. Small size of the initial defect is ensured by taking the half width of the defect equal to b_0, which is the minimal size of a buckle for the given loading (see chapter 3).

From Fig. 4.7, we find for the propagation to occur from a defect of width $2b_0$,

$$\sigma_0 \geq c_1 \sqrt{\frac{E}{1-\nu}} \sqrt[3]{\frac{G_{Ic}}{h}} \tag{4.2}$$

with $c_1 \approx 19.97\,\mathrm{Pa}^{1/6}$ for $\eta = 0.95$ and $\nu = 0.31$. We define σ_c^* as

$$\sigma_c^* = c_1 \sqrt{\frac{E}{1-\nu}} \sqrt[3]{\frac{G_{Ic}}{h}} \tag{4.3}$$

This enables re-definition of the loading ratio based on a critical stress for propagation of the buckling driven delamination from an initial defect of width larger than $2b_0$ but smaller than the final $2b$, σ_0/σ_c^*.

Interestingly, we did not observe any propagation of straight sided blister in the numerical simulations for equi-biaxial loaded films with the mode II dependence chosen ($\eta = 0.95$). This result is in accordance with Jensen [18] who predicted almost immediate instability of a straight front for such loading. This instability can be checked by comparing σ_0/σ_c^* with the loading ratio σ_0/σ_c of the equivalent straight sided blister.

Calculation of σ_c. In order to evaluate σ_c, numerical simulations of straight sided blisters similar to the one presented in chapter 3 were conducted with the same parameters used to generate the phase diagram, i.e. $\eta = 0.95$, $\nu = 0.31$, $T_n^{max} = 17$MPa and $T_t^{max} = 200$ MPa in addition, Young modulus was fixed to $E = 329$ GPa. Data were extracted in order to find the one to one relation between σ_0/σ_c and G_0/G_{Ic}, which we have seen is independent[4] of b.

We plot in Fig. 4.8 the loading ratio for the particular case $\sigma_0 = \sigma_c^*$ as a function of G_{Ic}/G_0. This curve indicates the loading ratio of a straight sided blister on the

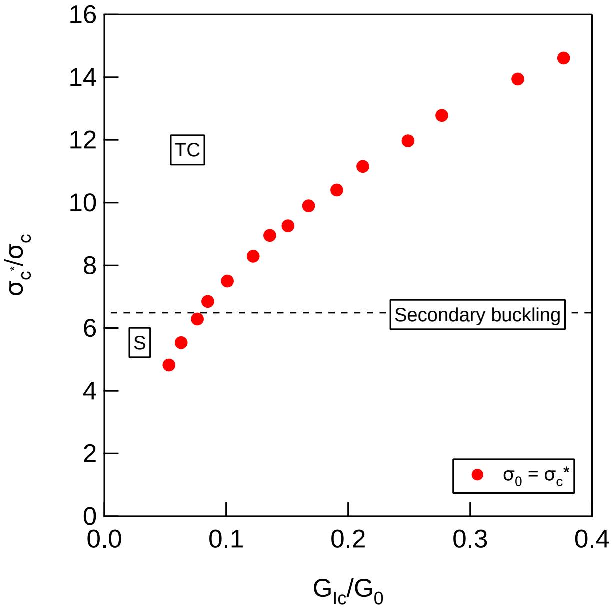

Figure 4.8: Ratio between the critical propagation stress and the critical buckling stress, σ_c^*/σ_c as a function of G_{Ic}/G_0.

onset of propagation for several energy level. We observe that when the interfacial toughness is increased in comparison with the total elastic energy stored in the film, the loading ratio of a straight sided buckle grown from the defect is increased. This is somewhat unexpected as σ_0/σ_c decreases with G_{Ic}/G_0 for the straight sided blister, see for example Fig. 3.11. This decrease of σ_0/σ_c is compensated by the fact that the level of stress required to propagate increases.

Parry et al [11] and Moon et al [19] have computed the loading ratio at which the sides of a straight sided blister are unstable under equi-biaxial loading. They report that above $\sigma_0/\sigma_c = 6.5$ the straight sided buckle is not stable and tends to destabilize into a TC like blister. We note that, at the onset of propagation, this value σ_0/σ_c is reached for $G_{Ic}/G_0 = 0.08$. It therefore means that no stable straight sided blister may grow from an initial defect for values of G_{Ic} greater than $0.08G_0$. Below this value, growth of a straight sided blister may be possible. Experimentally, interfacial G_{Ic} of silver thin films on silica has been measured previously by cleavage test in [20] to be around $0.4\,\mathrm{J/m^{-2}}$. It therefore means that to grow a straight sided blister with a molybdenum thin film it requires $\sigma_0 < 500\,\mathrm{MPa}$ and $h > 8\,\mu\mathrm{m}$. Such films are rather thick and require several hours of sputtering and were not tested. Neither was it possible to obtain straight sided blister for the mode II dependence chosen numerically.

---

[4] Note that for these parameters the size of the process zone is 30% of b for the straight sided blister and drops to 10% of the half width within which the TC blister is confined.

4.2.3 Range of stability of the TC morphology

Two boundaries may be considered for the stability of the TC buckles : 1) Either the first appearance of a branch in the morphology or 2) complete disappearance of the TC morphology. As branching relies on instability of the front, it is not surprising that the limit between branching morphologies and TC like blister is blurred. One possible boundary is plotted in Fig. 4.7. This boundary may move a little depending on the mesh size adopted in the simulation. Here the element sizes were scaled with h and $\bar{E}/\sigma_0$ so that the number of elements along b for an equivalent straight sided blister would remain constant. It is quite remarkable that the boundary remains linear with the parameters chosen and corresponds also to a critical stress.

We observe that for $\sigma_0/\sigma_c^* = 1.11$ we have appearance of the first branch in the morphology. TC blister are still observed up to $\sigma_0/\sigma_c^* = 1.16$, above which only branching blisters are observed. We point out that a small variation of the stress for a given thickness and interfacial toughness may lead to a strong variation of the morphology observed. Such variations are common in Mo thin films as seen in chapter 2. If we assume that the stress is kept constant and variation of G_0 arises solely from the thickness, TC buckle may be observed over a range of thickness. If h_0 is the thickness of the film at the onset of propagation, TC buckle will be observed up to $1.5h_0$.

Experimentally, TC buckles are observed over a wider range of thickness and stress level which may seem contradictory with the previous numerical result. This is a more subtle effect related to thin film deposition and stress build up (chapter 2). To better explain this effect, in Fig 4.9 we plot the evolution G_{Ic}/G_0 as a function of $\sigma_0/\sqrt{E}$ of two experimental molybdenum thin films presented in chapter 2. To compare with the model, we assume the superlayer is deposited on top of an interface with an interfacial toughness in mode I of $G_{Ic} = 0.4\ \mathrm{J.m^{-2}}$ and that no relaxation occurs in the thin film after deposition.

For $\mathrm{MoO_x}$ thin film, the range over which TC buckles are predicted stable extends from 195 nm to 283 nm, which is consistent with a rapid destabilization of the TC buckle. In the pure Mo case, TC buckles are expected from 230 nm up to 670 nm. This larger range of stability is due to a strong decrease of the average residual stress through the thickness and a small increase in G_0, which is common in Mo thin films past the first nanometers. As a result the curve representing the

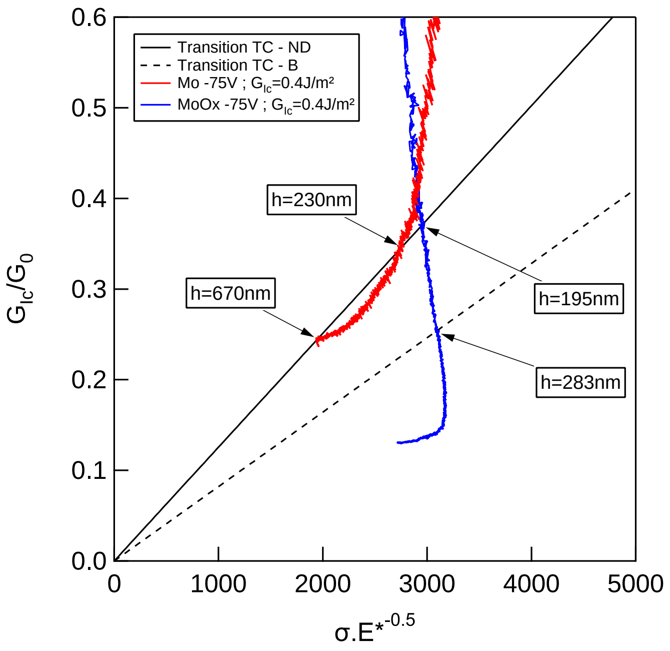

Figure 4.9: Possible energy range available with two different superlayer, Mo and MoO$_x$ at −75 V assuming an interface with $G_{Ic} = 0.4$ J.m^{-2}.

possible delamination morphologies exits the region where buckle may propagate above 670 nm even though G_0 increases.

4.2.4 Stress released in the blister during buckling

From the numerical results, the elastic strain energy in the plate is averaged over the delaminated area, excluding the initial defect zone. From this, we can estimate the amount of stress released in the blister. Results are presented in Fig. 4.10 and are expressed as a percentage of σ_0. It is observed that the amount of stress relaxed in the buckled state depends on both G_{Ic}/G_0 and $\sigma_0/\sqrt{E}$. In the case where the defect does not propagate, the energy released is equal to zero. The telephone cord like blister is the morphology where stress is the less relaxed. Branches morphologies relax more energy.

Over the range of tested parameters, the percentage of stress relaxed on average is limited to 78% to 82% for the TC morphology. This corresponds to an energy left in the buckled state of about 36%. Values obtained by Moon and co-authors [19], while studying destabilization of a thin plate of width $2b$ at large σ_0/σ_c, are significantly lower as they predict elastic strain energy as low as 20% left in the buckle. The difference can be attributed either to the fact that the film does not delaminated fully next to the sagged area or to a lower relaxation in the process zone, see Fig. 4.11.

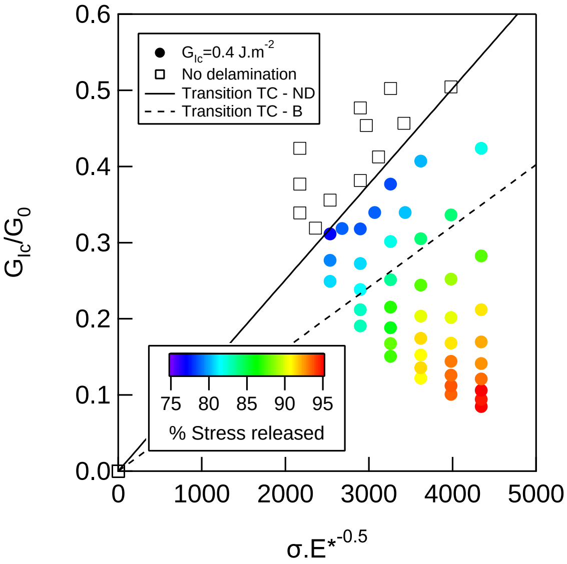

Figure 4.10: Amount of stress relaxed in the buckled state for $G_{Ic} = 0.4\,\mathrm{J.m}^{-2}$, $\eta = 0.95$ and $\nu = 0.31$. Transitions between morphologies are reported from Fig. 4.7.

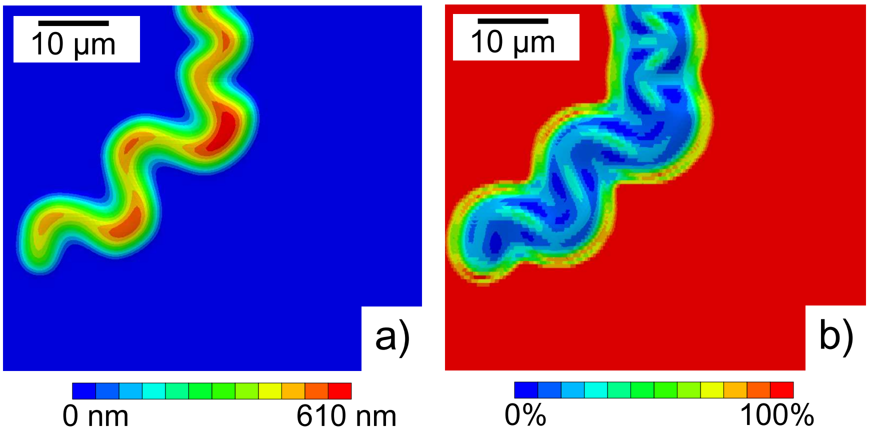

Figure 4.11: Numerical result of delamination of a thin film. $h = 150\,nm$, $\sigma_0 = 2.5$ GPa, $G_{Ic} = 0.4\mathrm{J.m}^{-2}$ a) Out-of-plane displacement b) Percentage of energy left in the film.

4.3 Large cohesive zone sizes: The role of Ag

In the previous section we have discussed experimental cases in comparison with numerical simulations where periodic branching leads to complex delamination patterns. In addition, we considered the process zone Λ reasonably small in comparison of the width of delamination b. We will now present a case where the delamination pattern is influenced by a large process zone at the interface.

4.3.1 Periodic branching: evidence for hexagonal pattern

Among the branching morphologies we discussed previously, there exists a particular case where separation of the front gives rise to two new fronts oriented at an angle of 120° from each other. Alternate branching at the angle of 120° is only observed for small thicknesses $h < 150\,\text{nm}$ and for at least $\sigma_0 = 2\,\text{GPa}$. In Fig 4.12 we present three cases of buckles branching in this fashion. Detailed sputtering conditions are given in Tab A.6. For those particular buckles, propagation of the branches remained limited on the sides and resulted in a confinement of the buckle within a certain width, similar to a TC buckle. The blisters presented a branch every three sags alternatively to the left and to the right of the propagation direction, which led to a new apparent period $\lambda_b = 3\lambda/2$.

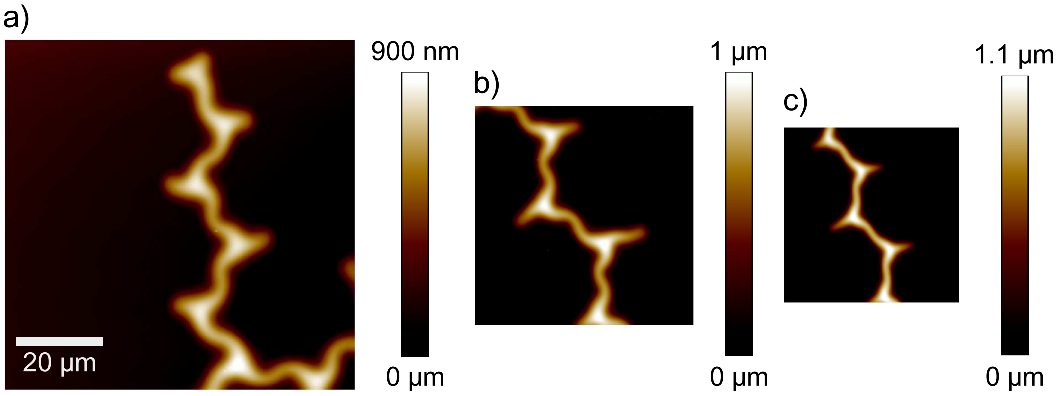

Figure 4.12: Atomic force microscopy of sample a) C_1, b) C_2, c) C_3

When the branches extend on the sides of the normal direction, a vast area of the film is delaminated. The pattern resulting from the delamination of the film is presented in Fig. 4.13 for various thickness of the silver film. When the thickness of silver is small, the delamination pattern seems erratic even though branching occurred regularly at the period λ_b. When the thickness of silver is increased, the network of blisters self-organizes into an array. It adopts a hexagonal pattern to

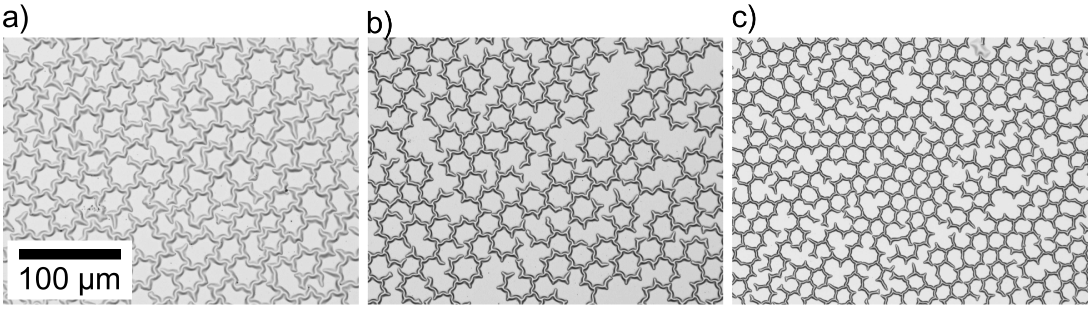

Figure 4.13: Evolution of the delamination morphology for different loading conditions and thickness of silver. a) C_1, b) C_2, c) C_3

cover the whole area of the sample. In Fig. 4.13.c, the pattern arises from the creation of branches every 11.5 μm leading to two fronts, each at 120° from the initial blister. We observe almost no variation of the period over the whole wafer, ($< 5\%$). Such regular branching leads to an hexagonal pattern with a side size of 11.5 μm. However, blisters forming the hexagons are not completely connected. For a given hexagon, there is always at least a zone where two branches meet without connecting. The distance between two fronts varies and is measured between 300 nm for the closest to 2 μm for the furthest which is at least twice of the thickness of delaminated stack considered.

4.3.2 Telephone cords : large aspect ratio

The particularities of stacks with thicker silver layers do not only reside in the organization of the branching network. With thick silver layers, it is possible to delaminate the film in the telephone cord regime previously described where branching does not occur. In this case, the change of morphology due to silver thickness is not visible in the formation of a network but on the out-of-plane displacement of the blister. In Fig. 4.14 we plot δ/h as a function of the elastic energy G_0 stored in the superlayer for several samples with a $\mathrm{SiO_x}$//Ag interface and silver thickness 8.4 nm, 40 nm and 60 nm. δ is measured between the two sagging points of a half period. Even though interfacial toughness is unknown, it can be assumed to be subject to small variation as the interface is not directly modified, therefore G_0 is a good indication of the loading level of the blister. We first observe that experimental values of δ/h are confined within 4.5 and 6.5 when the thickness of silver is equal or lower than 15 nm. Such values are in accordance with values obtained in numerical simulations which are also presented in Fig. 4.7. In the numerical simulations with a cohesive zone, ensuring $\Lambda < 10\%$ of b, no blisters had a normalized out-of-plane displacement greater than 7 and lower than 4. Data found in the literature [21] also point towards values of δ/h for TC like blisters in this range. Incidentally, values of δ/h are in any case far greater than 2.8 which is the maximum value reached by a straight sided blister when pure mode II is reached on the sides ($\psi = -90°$) for a rigid substrate.

For stacks with a thickness of 40 nm or 60 nm however, larger normalized out-of-plane are measured from $\delta/h = 8$ up to $\delta/h = 12$. Such values cannot be ascribed to larger residual stress in the thin film. Indeed, the residual stress in the film before buckling is measured experimentally and range from 2 to 3 GPa, which does not differ from other samples. In addition numerical simulations were conducted at higher level of residual stresses, up to 4 GPa and never exceeded $\delta/h = 7$. Material properties of the superlayer and stress loading are not responsible for the phenomenon observed.

In order to characterize these films further, we can estimate the average strain released during buckling. Let A_0 be the initial surface area of the film experiencing buckling and let A be the final specific surface area of the film in the post-buckling

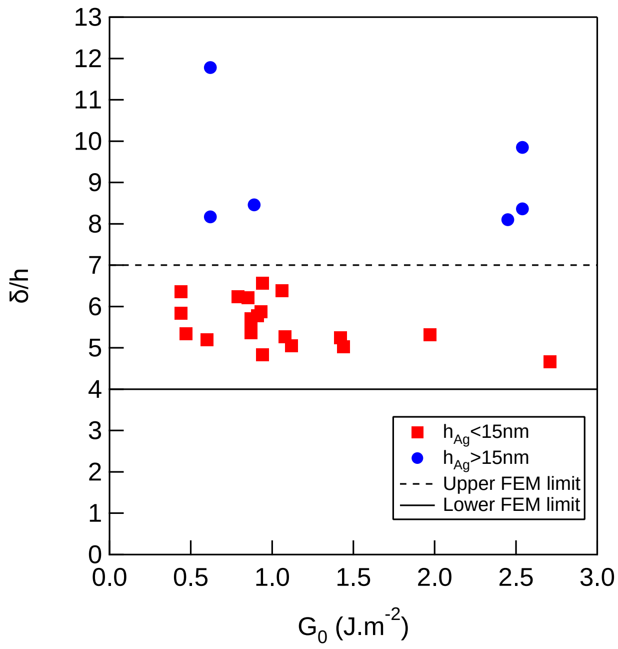

Figure 4.14: Experimental values of δ/h as a function of the elastic energy for $\mathrm{SiO_x}$//Ag/Mo samples. Upper and lower limits for δ/h in numerical simulation for $\eta = 0.95$.

regime. Note that A_0 is simply the projected area of the blister. In this case the average strain released during buckling is simply :

$$\epsilon = \frac{A - A_0}{2A_0} \tag{4.4}$$

Both A and A_0 can be measured using atomic force microscopy. Considering the propagation of the TC like blister observed experimentally and numerically, we have evidence that the interface has not been broken in the area close to the pinning point, see Fig 4.11. Therefore we consider A_0 as the area defined by a non-zero out-of-plane displacement with respect to the surface of the thin film over one period. This rather rough evaluation of strain can be compared to the in-situ measurement. Results are presented in Tab. 4.2. It is observed that for the sample with the lowest thickness of silver, the stress measured from the area is about 79% of the stress measured in-situ. This corresponds to an energy left in the buckled state of about 36%. This experimental observation is consistent with our numerical simulation presented in the previous section. For films with higher thickness of silver the strain in the buckled area far exceeds the in-situ strain. This cannot be explained without considering that the stress is actually relaxed in-plane around the buckled film. Assuming a relaxation of 80% on average for the stress during buckling, the in-plane zone to be considered around the buckled part extends to $\Lambda = 6.5\ \mu$m on each sides. Without arguing on the state of the interface under the in-plane relaxed

Sample	C_1	C_2	C_3
Ag thickness	8.4 nm	40 nm	60 nm
Mo thickness	108 nm	132 nm	95 nm
In-situ stress	1.88 GPa	1.84 GPa	2.85 GPa
Area stress	1.48 GPa	3.09 GPa	6.34 GPa
$2b$	9.58 μm	6.60 μm	4.75 μm
Λ	-	6.80 μm	6.60 μm

Table 4.2: Measurements of the samples used to study the influence of Ag thickness on the morphology of delamination.

area and on the origin of such relaxation, such characteristic length is very similar to a process zone. In our experiments Λ would be 206% of b with a silver thickness of 40 nm and 279% of b for 60 nm. Such values are very large for films of hundred nanometers.

4.3.3 Role of the process zone size in the delamination morphology

While studying the delamination morphology in the previous section, we did not observe any organization in the branching regime. One of the parameter we did not modify was the cohesive stress in mode II T^t_{max}. We have presented in chapter 3 the influence of a large process zone on a straight sided blister, caused mostly by the mode II cohesive stress. Such influence can also be conducted in three dimensions.

In Fig. 4.15 we present the delamination morphology when the cohesive stress in mode II is strongly decreased ($T^t_{max} = 12$ MPa). As the dependence for the mixed-mode is fixed with $\eta = 0.95$ and $G_{Ic} = 0.4$J.m^{-2}, it corresponds to a crack opening displacement for the mode II of 10.8 μm. It is observed in Fig. 4.15-a) that

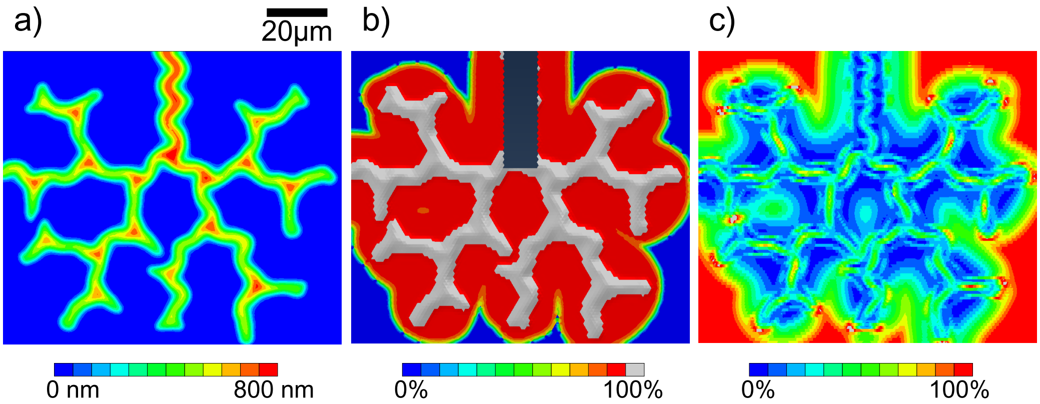

Figure 4.15: Numerical simulation of buckling driven delamination with $\sigma_0 = 1.8$ GPa, $h = 95$ nm $G_{Ic} = 0.4$ J.m^{-2} and $T^t_{max} = 12$ MPa. a) Out-of-plane displacement b) Damage variable of the cohesive elements. c) Strain energy left in the film as a percent of G_0.

the morphology adopted by the delamination is the shape of a hexagonal network, very similar to the one reported in Fig 4.13. The width of the buckle between two branches is equal to $2b = 6\,\mu$m. The normalized out-of-plane displacement is equal to $\delta/h = 6$ which is large for this level of in-plane stress before buckling. Note that the delamination occurs at $\left(\sigma_0/\sqrt{E} = 2610; G_{Ic}/G_0 = 0.62\right)$ which is outside the limits determined in Fig 4.7 for propagation of an initial defect. As the phase diagram was computed for a larger value of cohesive stress, limits might change depending of this parameter.

In Fig. 4.15-b) we report the damage variable of the cohesive elements, it is representative of the extension of the process zone Λ. We observe that Λ is not homogeneous along the crack front. Variation of Λ is expected as the mode mixity along the front is not constant. In particular, $\Lambda = 3\,\mu$m for the curved front of the branches still propagating and $\Lambda = 11\,\mu$m next to the pinning points, which is consistent with the value of the crack opening displacement in mode II chosen. On average, we have $\Lambda/b \approx 2.4$ which is very similar to expected values in the experimental cases.

In Fig. 4.15 we observe the amount of strain energy left in the blister as a percentage of G_0. In the buckled area, the energy left is, on average, 40% of G_0 as found previously for cases with a smaller process zone, see Fig 4.10. Surprizingly, the maximum relaxation does not occur in the buckled part but in the film above the process zone. Above the process zone, the energy left is only 7% of G_0 over the first $2\,\mu$m. The amount of energy relaxed decreases further apart of the buckle.

This numerical simulation of an organized hexagonal pattern shows that, firstly a large process zone is necessary for organization of the branching network. Secondly the stress in the film is relaxed above the process zone.

4.3.4 Material origin of a large process zone at the interface SiO$_x$/Ag

We have shown experimentally and numerically that a large relaxation zone around the blister is necessary in order to understand the formation of an organized structure such as the hexagonal pattern. The size of this zone should be of the order of $\Lambda/b \approx 2$, which in experimental cases corresponds to $6\,\mu$m. As only the thickness of silver is modified significantly, we expect it to play an important role in the high-aspect ratio structure.

We first present in Fig. 4.16-a) a SEM cross-section of sample C_3. On the figure we can notice an excess of silver dewetting around the buckle. This large dewetting is observed up to $4.4\,\mu$m. This phenomenon underlines the high mobility of silver at room temperature and the possibility for the molybdenum superlayer to deform silver. In Fig. 4.16-b) a SEM cross-section of the same sample at higher magnification is presented. We observe a large pack of silver at the edge of the buckled part of the film. On the left side of the silver pack, we observe a zone depleted of silver. This

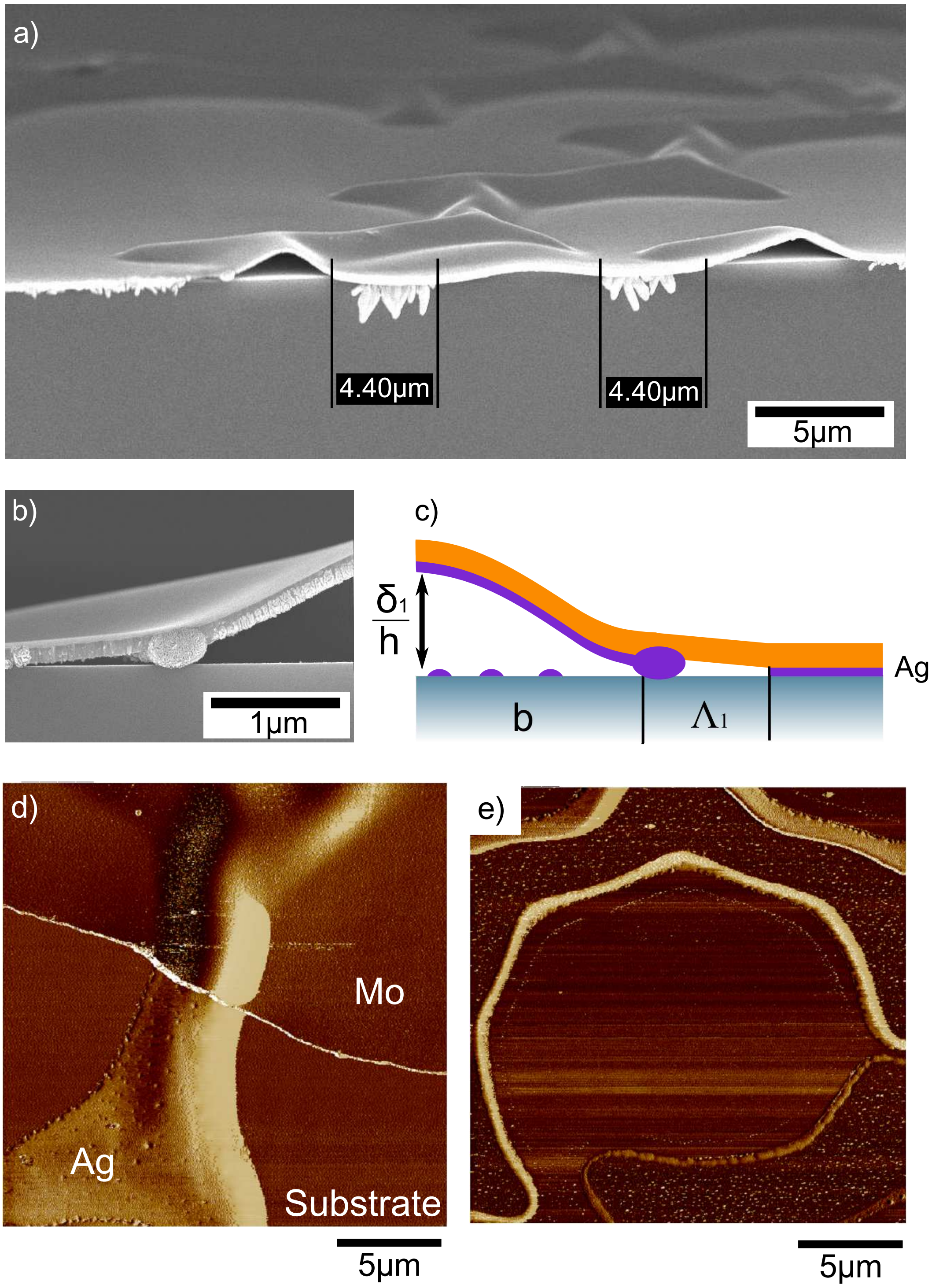

Figure 4.16: a) and b) SEM cross-section of sample C_3. c) Schematic of the silver interface for large thickness of silver. d) AFM phase measurement of sample C_3 after peeling. e) AFM phase measurement of sample C_3 after removal of silver blister.

zone is 1 μ large. On the right side, under the buckle, silver can be observed. It appears that silver moved from the the depleted area to the large pack of silver. Note that in the depleted area, the film delaminated and possesses a non-zero out-of-plane displacement. Observation is summarized in Fig 4.16-c).

In order to check the presence of such depleted area around the blister, we peeled the molybdenum layer using a regular tape. We then observed the sample under atomic force microscopy. We observe that in some parts of the sample, the interface broke between Ag and Mo above the buckles and between Ag and SiO_x outside. As a result, the sample is left with hexagonal blisters of silver, see Fig. 4.16-d) for an AFM phase image. In other parts of the sample, the remaining buckles broke, see Fig. 4.16-d). Under the broken buckles, some silver islands are observed. At the edge of the blister, large packs of silver are present as seen previously on the SEM cross-sections. Right outside of the packs a zone without islands is deliminated by the edge of the buckle parts and islands. This zone is of equal width all around the hexagon and is equal to $1\,\mu$m and corresponds to the zone observed in cross-section. In the center of the hexagon, islands are also present, though their size and number are smaller than the one found under the buckled part.

4.3.5 Discussion

Results presented in this section show organization of a branching buckles network when the thickness of silver is increased. Concomitantly with the organization of the network, the compressive stress in the film is relaxed around the buckled area of the film. The area extends to several microns around the buckle. Numerically, such relaxation occurs when a large process zone exists at the interface.

Presence of large plastic zone up to $\Lambda \approx 4\ \mu$m around TC buckle was reported by Cordill and coauthors [22]. The process zone appeared when the grain size of copper at the interface increased and the yield stress decreases down to 390 MPa. In our case, the process zone takes place in the silver layer at a thickness above 25 nm and is likely to be due to plasticity in silver. The yield stress of a silver thin film was estimated by nano-indentation in [23] and [24] in the hundred of MPa and as low as 100 MPa. The value of the yield stress given in the literature is one order of magnitude larger than the value of the cohesive stress required in the numerical simulation for apparition of a large process zone, but is likely to depend on the deposition conditions of the silver thin film. In addition the yield stress is likely to drop as the thickness of the film increases. The shear applied at the edge of the blister in mode II by the superlayer however far exceeds the yield stress of the silver thin film, thus causing plasticity.

Presence of a large plastic zone at the interface around the buckle introduces a new length Λ in the problem. We believe this zone is responsible for organization of the network. It enables two crack fronts to interact with each other even though the substrate is purely rigid.

4.4 Conclusion

In this chapter we have studied the morphology of the delamination pattern experimentally and numerically. The role of the front instability and creation of a pinning point loaded in pure mode II is critical for arrest of the crack front and formation of a periodic pattern. The phase diagram of the possible morphologies reveals that under equi-biaxial loading, two criteria are required to predict stability or branching of the side : a criterion in energy G_{Ic}/G_0 and a criterion in stress $\sigma_0/\sqrt{\bar{E}}$. Interfaces based on silver enabled experimental observation of a large plastic zones around the buckle. The role of the plastic or process zone in the formation of an organized hexagonal pattern has been confirmed by numerical simulation.

Bibliography

[1] P. Waters and A. A. Volinsky. Stress and moisture effects on thin film buckling delamination. *Exp. Mech.*, 47:163–170, 2004.

[2] A. A. Taylor, M. J. Cordill, L. Bowles, J. Schalko, and G. Dehm. An elevated temperature study of a ti adhesion layer on polyimide. *Thin Solid Films*, 531:354–361, 2013.

[3] B. Audoly and A. Boudaoud. Buckling of a stiff film bound to a compliant substrate - part i : Formulation, linear stability of cylindrical patterns, secondary bifurcations. *J. of the Mech. and Phys. of Sol.*, 56:2401–2421, 2008.

[4] B. Audoly and A. Boudaoud. Buckling of a stiff film bound to a compliant substrate - part ii : A global scenario for the formation of herringbone pattern. *J. of the Mech. and Phys. of Sol.*, 56:2422–2443, 2008.

[5] B. Audoly and A. Boudaoud. Buckling of a stiff film bound to a compliant substrate - part iii : Herringbone solutions at large buckling parameter. *J. of the Mech. and Phys. of Sol.*, 56:2444–2458, 2008.

[6] S. Goyal, K. Srinivasan, G. Subbarayan, and T. Siegmund. A non-contact, thermally-driven buckling delamination test to measure interfacial fracture toughness of thin film systems. *Thin Solid Films*, 518:2056–2064, 2010.

[7] N. J. Simrick, J. A. Kilner, and A. Atkinson. Thermal stability of silver thin films on zirconia substrates. *Thin Solid Films*, 520:2855–2867, 2012.

[8] M. Morita, T. Ohmi, E. Hasegawa, M. Kawakami, and M. Ohwada. Growth of native oxide on a silicon surface. *J. Appl. Phys.*, 68:1272–1281, 1990.

[9] A. A. Abdallah, P. C. P. Bouten, J. M. J. den Toonder, and G. de With. *Thin Solid Films*, 516:1063–1073, 2008.

[10] J. W. Hutchinson. *Acta metall. mater.*, 40(2):295–308, 1992.

[11] G. Parry, A. Cimetiere, C. Coupeau, J. Colin, and J. Grilhe. Stability diagram of unilateral buckling patterns of strip-delaminated films. *Phys Rev E Stat Nonlin Soft Matter Phys*, 74(6 Pt 2):066601, 2006.

[12] J. Colin, F. Cleymand, C. Coupeau, and J. Grilhé. *Phi. Mag. A*, 80:2559, 2000.

[13] M.-W. Moon, H. M. Jensen, J. W. Hutchinson, K. H. Oh, and A. G. Evans. *J. Mech. Phys. Sol.*, 50:2355, 2002.

[14] M. Y. He, A. G. Evans, and J. W. Hutchinson. *Mater. Sci. Eng.*, A245:168, 1998.

[15] M. R. Memm and A. G. Evans. *Acta. Mater.*, 48:1815, 2000.

[16] A. G. Evans, J. W. Hutchinson, and M. Y. He. *Acta. Mater.*, 47:1513, 1999.

[17] M.-W. Moon, J.-W. Chung, K.-R. Lee, K. H. Oh, and R. Wang. An experimental study of the influence of imperfections on the buckling of compressed thin films. *Acta. Mater.*, 50:1219–1227, 2002.

[18] H. M. Jensen. Energy release rates and stability of straight-sided, thin-film delaminations. *Acta metall. mater.*, 41:601–607, 1993.

[19] M.-W. Moon, K.-R. Lee, K. H. Oh, and J. W. Hutchinson. *Acta Mater.*, 52:3151, 2004.

[20] E. Barthel, O. Kerjan, P. Nael, and N. Nadaud. Asymmetric silver to oxide adhesion in multilayers deposited on glass by sputtering. *Thin Solid Films*, 473:272–277, 2005.

[21] M. J. Cordill, D. F. Bahr, N. R. Moody, and W. W. Gerberich. *Mat. Sci. and Eng. A*, 443:150–155, 2007.

[22] M. J. Cordill, T. Muppidi, N. R. Moody, and D. F. Bahr. Effects of microstructure on the mechanical properties of copper films for high aspect ratio structures. *Micro. Tech.*, 10:451–455, 2004.

[23] Y. Cao, S. Allameh, D. Nankivil andS. Sethiarag, T. Otiti, and W. Soboyejo. Nanoindentation measurements of the mechanical properties of polycrystalline au and ag thin films on silicon substrates : Effects of grain size and film thickness. *Mat. Sci. and Eng. A*, 427:232–240, 2006.

[24] H. Conrad and K. Jung. Effect of grain size from millimeters to nanometers on the flow stress and deformation kinetics of ag. *Mat. Sci. and Eng. A*, 391:272–284, 2005.

Conclusion

The purpose of this thesis was to study buckling driven delamination of thin films in order to evaluate how suitable it is for the evaluation of interfacial toughness. Experimentally, the superlayer method has been chosen, with molybdenum for the loading and silver for the interface. This choice imposed experimental study of the loading conditions. The necessary comprehension of the delamination morphologies along with the unknown behavior of the interface led to development of a general model for buckling driven delamination.

Residual stress in molybdenum thin films. In-situ study of residual stress in molybdenum thin films of thickness 30 nm to 700 nm has provided insight in the influence of pressure, bias potential and oxygen doping on residual stress. In particular ion peening of oxygen ions and its role on the modification of the film microstructure and residual stress has been identified. This improved understanding of the build up of residual stress may have some applications. One of them is to purposefully stress a thin film prior to post-processing so that the final residual stress is equal to zero. In this case, the layer will provide no driving force for delamination.

Model for buckling driven delamination. We have proposed a model coupling thin plate buckling and cohesive zone to solve buckling driven delamination problems. This model has proven successful when confronted to experimental results. We confirmed the critical role of the mixed-mode dependence of the interfacial toughness in the formation of the telephone cord like blister. A variety of morphologies has been evidenced experimentally, and reproduced numerically. Thanks to this model, we have identified two parameters governing the propagation of the delamination crack front. These two parameters prescribe boundaries within a phase diagram for the delamination morphologies. From a numerical point of view, several improvements can be brought to the model :

- in-plane stress is rarely isotropic due to the material itself or imposed by the geometry of the sample. Detailed study of the influence of stress anisotropy on the delamination morphology could explain why straight sided blister are still widely observed even at high loading ratios.

- thin films are nowadays more and more often deposited on soft substrates. Such films are also subject to delamination This is also the case when the substrate is stretched and compression arises in the film due to Poisson effect. In this problem, the elastic mismatch between the film and the substrate cannot be neglected and the substrate cannot be replaced by a rigid plane. Our model can be adapted and an elastic substrate can be added.

- we have modeled the ideal case of delamination with a single layer and homogeneous residual stress. In practice, delamination occurs within a multilayer stack. Elastic properties as well as distribution of stress is therefore not homogeneous through the thickness, as we observed experimentally for MoO_x thin films. A stress and modulus distribution can be added in the superlayer of the model to take into account the complexities and study their influence on delamination morphology.

From an experimental point of view, the perspective of this work is the estimation of interfacial toughness. Parameters identified for the phase diagram of the delamination morphology should be used in combination with the buckle size, namely λ and b, in order to calculate adhesion.

Self-organized blister network. We have observed experimentally deviations from the morphologies expected in the simple case with a small cohesive zone size and shown numerically how a large process zone induces organization of the buckles in a hexagonal network. In our samples, plasticity in the silver layer was providing this large relaxation zone. We believe this phenomenon can be controlled and used to pattern large surfaces without external means : as long as growth conditions of the crack front are unchanged, the network will remain identical. One possible application is microfluidics. Percolation of the network can be controlled using a material different than molybdenum. Silver can also be replaced by a material with a lower yield stress so that interaction between crack front occurs at larger distance, the size of the hexagons should therefore increase.

Appendix A

List of samples

Tables summarizing the different samples presented in the chapter on in-situ stress measurements for Mo and MoO_x thin films.

Sample	Material	Pressure	O_2 flux	Potential	Thickness	$<\sigma>$
S1	Mo	$1.4\,\mu$bar	0 sccm	F	259 nm	-1.30 GPa
S2	Mo	$5.0\,\mu$bar	0 sccm	F	247 nm	-752 MPa
S3	Mo	$7.0\,\mu$bar	0 sccm	F	257 nm	311 MPa
S4	Mo	$10.0\,\mu$bar	0 sccm	F	287 nm	2.00 GPa

Table A.1: Conditions of deposition for study of residual stresses in Mo thin films as a function of pressure. Fig 2.8

Sample	Material	Pressure	O_2 flux	Potential	Thickness	$<\sigma>$
S5	Mo	$1.4\,\mu$bar	0 sccm	F	23 nm	-1.11 GPa
S6	Mo	$1.4\,\mu$bar	0 sccm	F	45 nm	-1.07 GPa
S7	Mo	$1.4\,\mu$bar	0 sccm	F	68 nm	-1.85 GPa
S8	Mo	$1.4\,\mu$bar	0 sccm	F	95 nm	-2.04 GPa
S9	Mo	$1.4\,\mu$bar	0 sccm	F	113 nm	-1.95 GPa

Table A.2: Conditions of deposition to study reproducibility of residual stresses in Mo thin films. Fig 2.10

Table for stacks $SiO_x//Ag/MoO_x$ resulting in blisters. For each sample the thickness of silver is indicated. The thickness, residual stress and atmosphere at which blistering occur are noted as well as the period λ of the patterns formed.

Sample	Material	Pressure	O_2 flux	Potential	Thickness	$< \sigma >$
S10	Mo	1.4 μbar	0 sccm	0 V	620 nm	−522 MPa
S11	Mo	1.4 μbar	0 sccm	F	626 nm	−932 MPa
S12	Mo	1.4 μbar	0 sccm	−50 V	674 nm	−1.22 GPa
S13	Mo	1.4 μbar	0 sccm	−75 V	671 nm	−1.34 GPa

Table A.3: Conditions of deposition to study the influence of potential on residual stress in Mo thin films. Fig 2.13

Sample	Material	Pressure	O_2 flux	Potential	Thickness	$< \sigma >$
S14	Mo	2.1 μbar	0 sccm	F	274 nm	−1.23 GPa
S15	MoO_x	2.1 μbar	1 sccm	F	306 nm	−1.78 GPa
S16	MoO_x	2.1 μbar	2 sccm	F	328 nm	−2.08 GPa
S17	MoO_x	2.1 μbar	3 sccm	F	376 nm	−1.65 GPa
S18	MoO_x	2.1 μbar	4 sccm	F	382 nm	−1.13 GPa
S19	Mo	2.1 μbar	0 sccm	0 V	349 nm	−713 MPa
S20	MoO_x	2.1 μbar	2 sccm	0 V	323 nm	−1.28 GPa
S21	MoO_x	2.1 μbar	4 sccm	0 V	344 nm	−1.83 GPa
S22	MoO_x	2.1 μbar	6 sccm	0 V	339 nm	−1.22 GPa

Table A.4: Conditions of deposition to study the influence of oxygen doping on residual stress in Mo thin films. Fig 2.14

Sample	Material	Pressure	O_2 flux	Potential	Thickness	$< \sigma >$
S23	MoO_x	1.4 μbar	2 sccm	F	633 nm	−1.46 GPa
S24	MoO_x	1.4 μbar	2 sccm	−75 V	616 nm	−2.18 GPa

Table A.5: Conditions of deposition to achieve high stressed thin films.

Sample	Material	Potential	Thickness	Residual stress	Atmosphere	Period
C1	Ag	(−)	8.4 nm	(−)		
	MoO_x	F	108 nm	−1.88 GPa	Air	19.3 μm
C2	Ag	(−)	40 nm	(−)		
	MoO_x	−75 V	132 nm	−1.84 GPa	Vacuum	18.7 μm
	MoO_x	−75 V	140 nm	(−)	Air	21.0 μm
C3	Ag	(−)	60 nm	(−)		
	MoO_x	F	95 nm	−2.85 GPa	Vacuum	12.5 μm

Table A.6: Thin film multilayers used to study the influence of silver thickness on delamination morphology.

Appendix B

Effect of mode mixity definition

The analytical solution for the straight sided blister considering an infinite cohesive stress, will serve as a reference for the solution obtained numerically. In Tab.B.1 we show the results for four different simulations with different parameters for the cohesive zone.

Table B.1: Comparison between the different resolution method and definition of the mode mixity.

		Numerical solution with CZ			Analytical without CZ	
Method	ψ definition	$2b_{total}$ (μm)	$2b_{100\%}$ (μm)	δ/h	δ/h	ψ
Implicit	Traction	8.39	7.27	1.575	1.607	-74.29
Explicit	Traction	8.39	7.27	1.568	1.607	-74.15
Implicit	Energy	17.5	16.9	3.981	4.043	80.12
Explicit	Energy	17.5	16.9	3.981	4.043	80.12

Euler solution. Either implicit or explicit scheme converge to the same solution which is very close to straight sided blister on a rigid substrate without a cohesive zone. We verify that the normalized out-of-plane displacement is linked to the width of the blister by :

$$\frac{\delta}{h} = \sqrt{\frac{4}{3}\left(\frac{\sigma}{\sigma_c} - 1\right)} \tag{B.1}$$

where σ_c is the critical buckling stress for a plate of width $2b$. This is the characteristic of the Euler solution. In addition, for a straight sided blister standing on an infinitively deep substrate, the mode mixity on the side of the blister is linked to the normalized out-of-plane displacement and to the elastic mismatch through ω by :

$$\tan\psi = \frac{4\cos\omega + \sqrt{3}\,(\delta/h)\sin\omega}{-4\sin\omega + \sqrt{3}\,(\delta/h)\cos\omega} \tag{B.2}$$

This mode mixity must compare with the one satisfying Griffith criterion of rupture that gives in our case $G = \Gamma(\psi)$. For a straight sided blister, the energy release rate can be calculated from :

$$G = \frac{1-\nu_f^2}{2E_f} h \left(\sigma - \sigma_c\right)\left(\sigma + 3\sigma_c\right) \tag{B.3}$$

The mode mixity calculated from the final b_{total} is equal, in this example, to $\psi = -73.12\,°$.

Definition of the mode mixity. As presented in Tab.B.1, the final width of the blister is different depending of the definition chosen for the mode mixity. This can be seen on Fig.B.1 where we plot the out of plane displacement of the blister in the equilibrium state. Only the part where cohesive elements are present is displayed. The process zone is indicated with dashed lines in both cases. The final b is too large in case of definition based on energy. It means that the relation of the loading ratio to the mode mixity is different for definitions based on tractions and energies. We plot the normal and shear tractions at the interface in the equilibrium state in Fig.B.2. We observe that the distribution of traction on the cohesive elements is larger in case of mode II compared with mode I. It means that the extent of the process zone is limited by the distribution of normal traction at the interface. As a consequence, at the limit of the process zone the mode I component drops to zero while the mode II component is non-zero. This implies a pure mode II solicitation on one side of the process zone. This behavior is checked for both definition of the mode mixity. In addition, as the parameters of the cohesive zone modeling are identical in both cases, the normal and shear distribution are only influenced by the plate displacement. For a larger blister we observe a larger shear component and a smaller normal component.

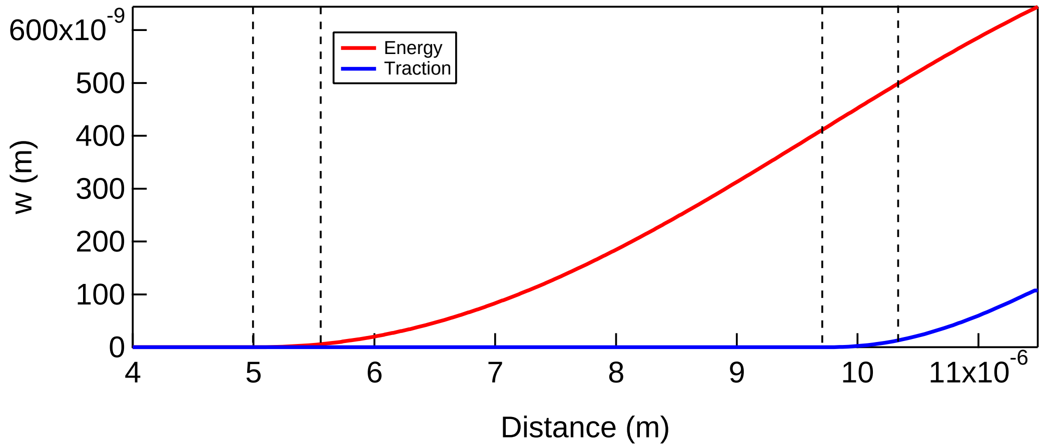

Figure B.1: Out-of-plane displacement of two straight sided blister for $G_{Ic} = 0.4$ J.m^{-2}, $\eta = 0.8$ and two definition of the mode mixity based on tractions and energies.

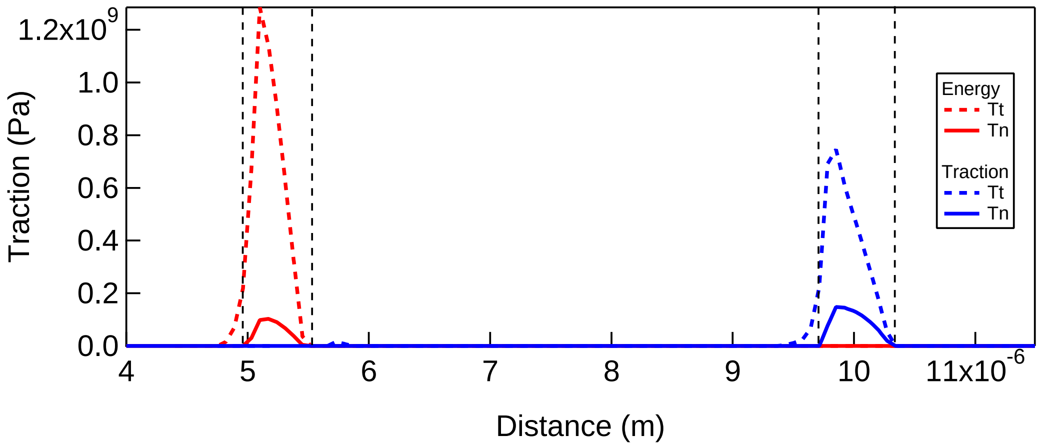

Figure B.2: Normal T_n and shear T_t tractions at the interface of two straight sided blister for $G_{Ic} = 0.4\,\mathrm{J.m^{-2}}$, $\eta = 0.8$ and two definition of the mode mixity based on tractions and energies.

We plot in Fig.B.3 the evolution of the mode mixity at the crack front as a function of the position of the crack front. From the equilibrium state, the mode mixity in the process zone can be estimated from the ratio of the tractions applied on the cohesive elements. Outside the process zone we use the value of energy spent during damage to evaluate the mode mixity at which the crack propagated. For

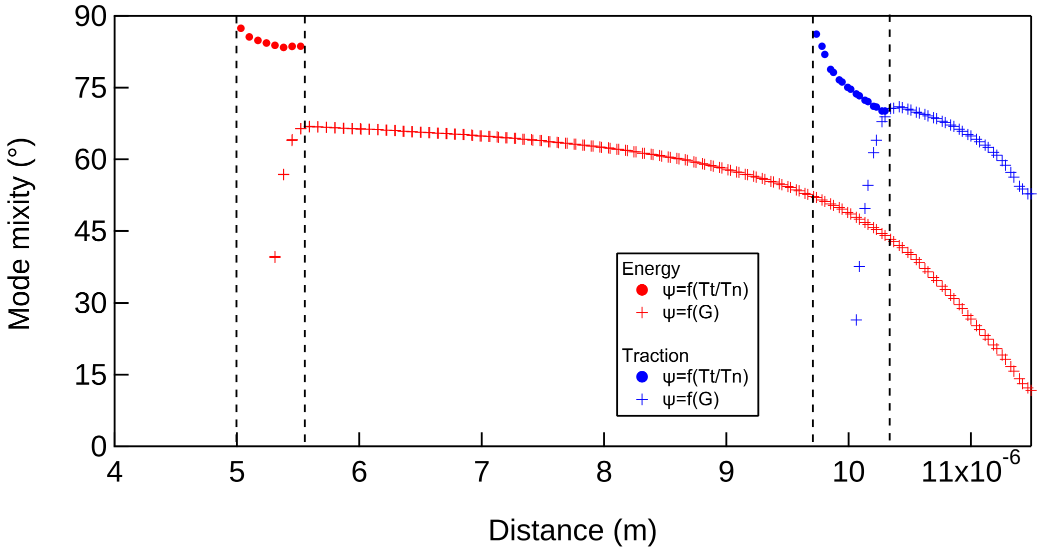

Figure B.3: Mode mixity at the interface calculated from tractions in the process zone and from the energy release rate for previous time step for two straight sided blister for $G_{Ic} = 0.4\,\mathrm{J.m^{-2}}$, $\eta = 0.8$ and two definition of the mode mixity based on tractions and energies.

both definition of the mode mixity we verify the continuity of the mode mixity in the process zone from ψ to $\psi = \pi/2$. In addition the mode mixity calculated from the energy of rupture is identical in both cases even though the equilibrium widths of the blisters are different. At a given b, the mode mixity at which the crack front propagates, and therefore the energy spent to propagate, is lower in the case of energy based definition.

The assumption used for calculation of the mode mixity from energies, given in Eq.3.35, is not correct in this particular case. This is due to the fact that G_I and G_{II} are solely computed from the strain applied on the elements and not from the work of the tractions.

Appendix C

Stress tuning in in sputter-deposited MoO$_x$ films

J.-Y. Faou, E. Barthel, S. Y. Grachev
Stress tuning in in sputter-deposited MoO$_x$ films
***Thin Solid Films*, *527*,** *(2013) 222-226*

Appendix D

How Does Adhesion Induce the Formation of Telephone Cord Buckles?

J.-Y. Faou, G. Parry, S. Y. Grachev & E. Barthel
How Does Adhesion Induce the Formation of Telephone Cord Buckles?
Phys. Rev. Lett., 108, *116102, 2011*

Jean-Yvon FAOU

Mécanique des couches minces fonctionnelles : instabilité et adhésion.

Résumé:

La thèse concerne l'instabilité des couches minces et en particulier à la délamination des couches sur substrat rigide. La première partie du travail s'intéresse aux contraintes résiduelles dans les couches minces de molybdène déposées par pulvérisation cathodique. Elle a permis d'étudier et développer des couches fortement compressives pour la délamination. Dans la seconde partie du travail ces couches fortement contraintes sont utilisées pour provoquer la délamination par cloquage d'un empilement contenant une interface faible. La propagation ainsi que la morphologie des délaminations ont été étudiés. Les paramètres qui affectent la morphologie des délamination sont identifiés et permettent la construction d'un diagramme de phase. Dans la dernière partie du travail un modèle numérique couplant flambage d'une plaque mince et zone cohésive est développé afin de modéliser le phénomène de délamination par cloquage. Les résultats obtenus par la méthode des éléments finis sont en accord avec les expériences.

Abstract:

We have studied thin film instabilities and in particular buckling driver delamination of thin films on rigid substrates. In the first part we studied residual stress in molybdenum thin films deposited by magnetron sputtering. With these results we can deposit a film with high compressive stresses for delamination. In the second part, compressive stressed layers are used to induce buckling driven delamination of a stack with a weak interface. Propagation as well as morphology of delamination are studied. Parameters playing a role in the buckling morphology are identified and enable drawing of a phase diagram. The last part of the work is dedicated to the development of a numerical model coupling buckling of thin plate and cohesive zone in order to model buckling driven delamination. This model has been solved by finite elements method. Results are sound with experiments.